2022

Synthesis And Characterization Of Functional Materials Using Silica Colloidial Crystals, Their Inverse Replicas, And Layered Double Hydroxides

Pratibha Mahale
University of Pennsylvania

Synthesis And Characterization Of Functional Materials Using Silica Colloidial Crystals, Their Inverse Replicas, And Layered Double Hydroxides

Abstract

The design of materials with tunable properties is at the forefront of material-based applications. The key to materials design is understanding their fundamental characteristics and establishing a structure-property correlation. This dissertation explores fundamental aspects of synthesis and characterization of functional materials designed using colloidal crystals, inverse replicas, and layered materials for electronics and energy devices applications. We have combined particle assembly and High Pressure confined Chemical Vapor Deposition (HPcCVD) to create ordered and electrically continuous 3D nanostructures of metals and semiconductors, defined as metalattices. These nanostructures have crystalline arrays of uniform particles in which the period of the crystal is close to the characteristic physical length scale of the material, for example, exciton Bohr radius in semiconductors, making them tunable for electronic, plasmonic, thermoelectric and spintronics applications. Silica nanoparticles in the range of 20-120 nm, assembled as micron thick films using vertical deposition technique, were used as templates for metalattice design. The interstices in the colloidal crystal films were infiltrated with polycrystalline semiconductors (Ge/Si/ZnSe) and metals (Ni/Pt/Ag/Pd/Au) using HPcCVD to obtain corresponding metalattices.We have developed a core-shell chemical passivation strategy for Ge metalattice prepared by infiltration of ~70 nm silica colloidal crystal using HPCVD. The oxide-free Ge core shows quantum confinement which depends on the void size in the silica template. The size of Ge sites dictated by the voids in the template and core-shell interdiffusion of Si and Ge can, in principle, be tuned to modify the electronic properties of the Ge metalattice. We have also investigated the structures of colloidal crystalline films and germanium metalattice in detail by scanning electron microscopy (SEM) and small angle x-ray scattering (SAXS). Particles smaller than ~32 nm diameter assemble into body centered cubic, whereas particles larger than 32 nm assemble into random hexagonal close pack structures with 2D hexatic phase. Polycrystalline films of these materials retain their structure, and long-range order upon infiltration at high temperature and pressure, and the structure is preserved in Ge metalattice. This detailed understanding of particle arrangements in the template can help in establishing structure-property relationships in the metalattices. We also explore material design made from layered materials for application in energy systems. We discuss method for controlled assembly of oppositely charged nanosheets using tri-block co-polymer F127 to tune their interactions and study the synthesis and anion exchange of Mg-Al, Zn-Al and Co-Al layered double hydroxides. We characterize their structural, thermochemical, and ionic conduction properties to understand their fundamental behavior for applications as anionic conductors in electrochemical systems operating between 100-250 °C.

Degree Type

Dissertation

Degree Name

Doctor of Philosophy (PhD)

Graduate Group

Chemistry

First Advisor

Thomas Mallouk

Keywords

anion exchange, assembly, colloids, layered double hydroxides, nanostructures, surface

SYNTHESIS AND CHARACTERIZATION OF FUNCTIONAL MATERIALS USING SILICA COLLOIDAL CRYSTALS, THEIR INVERSE REPLICAS AND LAYERED DOUBLE HYDROXIDES

Pratibha Mahale

A DISSERTATION

in

Chemistry

Presented to the Faculties of the University of Pennsylvania

in

Partial Fulfillment of the Requirements for the

Degree of Doctor of Philosophy

2022

Supervisor of Dissertation

Dr. Thomas E. Mallouk

Vagelos Professor in Energy Research

Graduate Group Chairperson

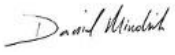

Dr. David W. Christianson

Roy and Diana Vagelos Professor in Chemistry and Chemical Biology

Dissertation Committee

Dr. Cherie Kagan, Stephen J. Angello Professor

Dr. Arjun Yodh, James M. Skinner Professor of Science

Dr. Tobias Baumgart, Professor of Chemistry

ACKNOWLEDGMENT

Graduate school has been an incredible learning and defining experience for me, and this journey would not have been possible without the valuable support of my advisor, mentors, collaborators, friends, and family. I am grateful that I embarked on this journey with Tom Mallouk as my supervisor. Over the years, working with Tom, I have learned to understand science and research in all its forms, and he has taught me to appreciate their synergy and find a balance. Tom has always provided steadfast support for my growth as a scientist and professional. I am thankful for the freedom he has given me to choose and chase different project ideas and carve my professional path by doing an internship during graduate school. It has been a blessing to experience his belief in our skills and the motivational 'you will figure it out' during the lows of research. I have learned a great deal about science outreach and communication from him outside of research and will forever cherish all our outreach events/projects.

I want to express my gratitude towards my committee members from UPenn - Dr. Cherie Kagan, Dr. Arjun Yodh and Dr. Tobias Bamgart, and Penn State - Dr. John Badding, Dr. Venkatraman Gopalan, and Dr. Lauren Zarzar. Discussions with them have always been thought-provoking and insightful. I appreciate their support through the COVID-19 pandemic and during our lab move to Penn. I would also like to especially mention our IRG project PI and my previous committee member Dr. John Badding; even though he is not with us today, his presence shall always remain in our work and his mentoring. Thank you for welcoming me with such warmth into the project and always encouraging the women scientists in the group.

None of my projects would have been feasible without my collaborators' contribution, mentoring, and support. As a part of MRSEC, I had the opportunity to work with researchers from different fields. I explored research questions with them and discovered the joy of collaborative problem-solving, gained mentors for Ph.D. and career, and most importantly, lifelong friends. Thank you, Dr. Jennifer Russel, for teaching me colloidal synthesis, Dr. Hiu Yan Cheng, Nabila Nabi Nova, Andrew Glaid, Dr. John Badding for HPCVD support, Dr. Parivash Moradifar and Dr. Nasim Alem for help with TEM and EELS, Dr. Alex Grede and Dr. Noel Chris Giebink for help in optical

characterization, Dr. Disha Talreja. Dr. Venkatraman Gopalan, Dr. Weinan Chen, and Dr. Ismail Dabo for including me in thermal studies, Dr. Yixuan Chen and Dr. Ying Liu for including me in electrical studies, and Dr. Yunzhi Liu, Dr. Susan Kempinger, and Dr. John Miao for making me a part of the magnetic studies. I would also like to thank Dr. Byeongdu Lee for his mentorship and discussions. During the second half of my Ph.D., I explored layered materials and functional materials for electrochemistry and had the opportunity to collaborate within the Mallouk group. Jarrett Dillenburger, Dr. Luis R. De Jesus , Dr. Zhifei Yan, and Linxi Xu, thank you for making experiments and discussions so much fun and informative.

The last five years of my Ph.D. would not have been so amazing without the support of the entire Mallouk group. I want to thank both past and present members of the Mallouk group who I had an opportunity to interact with – Alyssa, Zhifei, Langqiu, Jarrett, Ritesh, Luis, Linxi, Liquang, Chris Li, Pengtao, An, Chris Gray, Jeff, Jeremy, Colton, Zichen, Amy, Mary, Grace, Mohammed, Walter, Akshay, Kurt, Shunta and Yaya. I have found mentors, friends, collaborators, and confidants in this group. Thank you for creating a warm, positive and inclusive environment. The coffee chats, lunch breaks, and hot pots with you all will always be the highlight of this journey. I also want to thank my undergraduate mentees – Grace and Mohammed. Thank you for bringing your energy into the projects and helping me learn a bit of mentoring.

Outside of lab work, I had the opportunity to pursue my passion for science outreach and communication through MRSEC, GWIS, and Eberly college of science. Special thanks to Kristin Dryer, Tiffany Mathews, Alyssa, and Kyra for the memorable outreach opportunities. I have been fortunate to pursue an internship during my graduate school at P&G, and I would like to thank my manager Dr. Matt Wagner and my technical coaches, Dr. Yuri Roiter and Dr. Yonas Gizaw, for their mentorship and guidance. Thank you for introducing me to the world of industry R&D with so much care. Also, thanks to my fellow interns – Layla, Doug, Abbie, and Nityanshu for their support and my dear friends Rajat and Mohit for all the laughs and good food in Mason.

Graduate school was fun and at times, bearable due to consistent support and warmth received from my friends. A huge thank you to my friends from undergrad – Naveen, Tan, and Sowmya, who

were just a call/text away even though there were several miles and ocean between us. Thank you for growing with me and always hyping me regardless of the situation. Pho and Saehyun, I feel blessed to have you as my Ph.D. batchmates and my very best buddies. I cannot imagine surviving grad school without you two smart and beautiful ladies and our 'pretty nerdy' group. Thank you, Sai, Disha, Prawal, Puja, Vishikh, Alistar, Ambika, and Prhashanna, for the stress-bursting hangouts and delicious pot-lucks. Special thanks to Ahana, Raj, and Moupiya for your hospitality and for helping me settle down in the US. A very heartfelt thank you to my best friend and partner, Dr. Vijay Kumar, for being my rock during this graduate school journey. Thank you for consistently encouraging me, listening to me vent, making ten thousand and one plans for projects, celebrating my small wins, sharing my failures, and most importantly, for being you and for being a part of my journey. We did it!

Last but not least, I will try to put in words my gratitude towards my parents and sisters. Aai and baba, thank you for believing in me, dreaming with me, taking those small incremental steps with me to make these dreams a reality, teaching us the importance of persistence and hard work, and telling us that sky is the limit! Jyoti Tai and Monu Tai, thank you for venturing first and creating a path for me. I stand tall on the mountain of your grit, struggles, and achievements. Your support, encouragement, and pampering meant the world to me, even across the ocean.

Thank you all for making this journey special.

ABSTRACT

SYNTHESIS AND CHARACTERIZATION OF FUNCTIONAL MATERIALS USING SILICA COLLOIDAL CRYSTALS, THEIR INVERSE REPLICAS, AND LAYERED DOUBLE HYDROXIDES

Pratibha Mahale

Dr. Thomas E. Mallouk

The design of materials with tunable properties is at the forefront of material-based applications. The key to materials design is understanding their fundamental characteristics and establishing a structure-property correlation. This dissertation explores fundamental aspects of synthesis and characterization of functional materials designed using colloidal crystals, inverse replicas, and layered materials for electronics and energy devices applications. We have combined particle assembly and High Pressure confined Chemical Vapor Deposition (HPcCVD) to create ordered and electrically continuous 3D nanostructures of metals and semiconductors, defined as metalattices. These nanostructures have crystalline arrays of uniform particles in which the period of the crystal is close to the characteristic physical length scale of the material, for example, exciton Bohr radius in semiconductors, making them tunable for electronic, plasmonic, thermoelectric and spintronics applications. Silica nanoparticles in the range of 20-120 nm, assembled as micron thick films using vertical deposition technique, were used as templates for metalattice design. The interstices in the colloidal crystal films were infiltrated with polycrystalline semiconductors (Ge/Si/ZnSe) and metals (Ni/Pt/Ag/Pd/Au) using HPcCVD to obtain corresponding metalattices.

We have developed a core-shell chemical passivation strategy for Ge metalattice prepared by infiltration of ~70 nm silica colloidal crystal using HPCVD. The oxide-free Ge core shows quantum confinement which depends on the void size in the silica template. The size of Ge sites dictated by the voids in the template and core-shell interdiffusion of Si and Ge can, in principle, be tuned to modify the electronic properties of the Ge metalattice. We have also investigated the structures of colloidal crystalline films and germanium metalattice in detail by scanning electron microscopy (SEM) and small angle x-ray scattering (SAXS). Particles smaller than ~32 nm diameter assemble into body centered cubic, whereas particles larger than 32 nm assemble into random hexagonal

close pack structures with 2D hexatic phase. Polycrystalline films of these materials retain their structure, and long-range order upon infiltration at high temperature and pressure, and the structure is preserved in Ge metalattice. This detailed understanding of particle arrangements in the template can help in establishing structure-property relationships in the metalattices.

We also explore material design made from layered materials for application in energy systems. We discuss method for controlled assembly of oppositely charged nanosheets using tri-block co-polymer F127 to tune their interactions and study the synthesis and anion exchange of Mg-Al, Zn-Al and Co-Al layered double hydroxides. We characterize their structural, thermochemical, and ionic conduction properties to understand their fundamental behavior for applications as anionic conductors in electrochemical systems operating between 100-250 °C.

TABLE OF CONTENTS

LIST OF TABLES

LIST OF ILLUSTRATIONS

CHAPTER 1 – Introduction

1.1 3D Nanostructured material design in the sub-100 nm regime using silica colloidal crystal and high-pressure chemical vapor deposition

1.1.1 Materials by design – metamaterials

The ubiquitous presence of materials in our lives has prompted researchers to expand the discovery of natural materials and also establish structure-property-performance relationships in these materials. However, to support rapid changes in human lifestyle, fuel technological progress, and make sustainable development a reality, significant efforts are being made in designing materials beyond the existing natural materials. Artificially designed 3-dimensional materials, commonly defined as metamaterials, with periodicity smaller than the length scale of the wavelength/physical phenomenon of interest, have become increasingly popular to obtain properties/performance beyond existing natural materials[1–3]. The wavelength of interest can correspond to electromagnetic waves, and the physical phenomenon can correspond to the electronic, vibrational, optical, or magnetic length scales. Metamaterial properties with a selective response at these varying length scales have been tailored by controlling the length of lattice parameters, 3D arrangement/structure, and orientation of building blocks[2,3]. Significant progress has been made in designing and synthesizing metamaterials at the optical length scale. These photonic metamaterials have lattice parameters in the order of several hundreds of nanometers to hundreds of microns, allowing them to manipulate the transport of electromagnetic waves in the near UV to near IR region[4–6]. The success and continued development of photonic metamaterials has not only led to improved optical

devices but has also prompted the research of metamaterials on other length scales to manipulate the behavior of electrons, plasmons and phonons in the material.

1.1.2 Significance of 3D nanostructures

Metamaterials at the nanoscale, particularly in sub-100 nm regime (nanostructures), have recently gained attention for tuning the electronic, magnetic, and vibrational responses of materials. Metamaterials at this length scale should have structural order parameters comparable to the characteristic length scale of the intrinsic physical phenomenon in the material, for example the exciton Bohr radius in quantum confinement, the electron/phonon mean free path, and the magnetic domain wall thickness, to mention a few, allowing coupling/interaction between the structural periodicity and the corresponding physical phenomenon[7–10]. This interaction in a wide range of materials (semiconductors, metals, insulators) could give rise to new physics with applications in solar devices, electronic devices, thermoelectrics, near IR photonics, and light-emitting devices. In particular, interconnected semiconductor nanostructures in the sub-100 nm regime can create a tunable bandgap through quantum confinement, high interface area, and tunable carrier (electron, phonon) transport through the pervasively connected structure. Also, semiconductor systems offer independent controls on electrical and heat transport due to the respective carriers being electrons and phonons, which along with confinement effects, can make semiconductor nanostructures suitable for both electronic and thermoelectric applications.

1.1.3 Synthetic approaches to 3D semiconductor nanostructures

Several approaches have been attempted to create electronically continuous, atomically crystalline, periodic 3D semiconductor nanostructures in the sub-100 nm regime. Still, these continue to face challenges in incorporating interconnectivity, quantum confinement

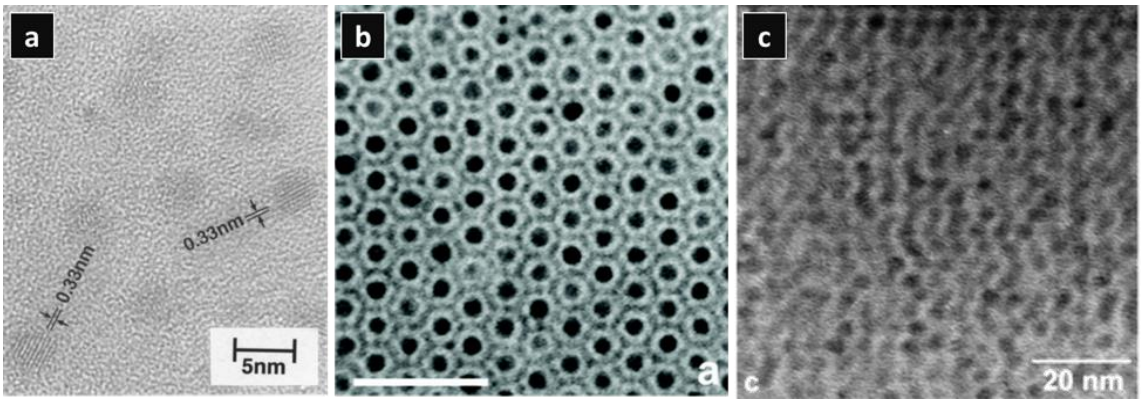

Figure 1.1. Different types of 3D semiconductor nanostructures obtained by (a) particles in a matrix, reprinted from (11), copyright 1998 American Physical Society (b) colloidal assembly of nanoparticles, reprinted from (12), copyright 2007 American Chemical Society (c) 3D array of semiconductor nanoparticles using hard templates, reprinted from (19), copyright 2002 American Chemical Society

effects, and periodicity in one structure. One of the approaches was to disperse semiconductor particles in a matrix, for example, Ge particles in a silica matrix[11] (Figure 1.1). While these structures showed promise in understanding quantum confinement effects, they failed to provide interconnectivity between particles and also had a random distribution of particles. Another approach that addresses the issue of periodic arrangement is the assembly of colloidal semiconductor nanoparticles into 3D structures[12,13] (Figure 1.1). These nanoparticle superlattices have long-range order, quantum confinement effects and also have shown evidence of extended electronic states[14,15]. However, the presence of ligands on the nanoparticles even after ligand exchange/stripping limits the connectivity between the particles. Soft templating methods

have created mesoporous structures with variable pore sizes of 1-50 nm that provide interconnectivity[16,17]. But these mesoporous semiconductors are not atomically crystalline. Hard templating methods were also explored, and periodic mesoporous materials such as silica (MCM-41) and zeolites were used as hard templates to obtain a 3D array of semiconductor nanoparticles[18–20]. Using periodic templates incorporated size effects and periodicity/order but not interconnectivity since the semiconductor particles grow and localize in the pore.

1.1.4 Silica nanoparticle template and HPCVD assisted synthesis of 3D nanostructures in sub-100 nm regime

Although significant developments have been made by the approaches mentioned above in the quest for electronically continuous, interconnected and atomically crystalline semiconductor nanostructures, there is still a need for a method that overcomes the challenges of incorporating all the desirable characteristics into one system. Recently, a novel approach has been developed to synthesize polycrystalline interconnected semiconductor nanostructures in the sub-100 nm regime by combining silica nanoparticle films and high-pressure chemical vapor deposition (HPCVD)[21–24]. This approach uses silica nanoparticle assembly as templates to access the interconnected network of voids/pores arising from the 3D arrangement of the particles. HPCVD or high pressure confined chemical fluid deposition (HPcCFD) is then used to infiltrate the voids present in the templates using semiconductors and metals, resulting in 3D structures, as shown in Figure 1.2. The resulting nanostructures are called metalattices and are notionally sub-divided into meta-atoms (voids in the template) and meta-bonds as the interconnections between the meta-atoms. Metalattice lattice parameters, porosity and structure can, in principle, be controlled by the size and arrangement of the silica nanoparticles in the

template. For example, Figure 1.2 shows a germanium metalattice obtained by infiltrating a 30 nm silica template. The following two subsections will discuss the synthesis of silica nanoparticles, their assembly, and the infiltration of the assembled templates using HPcCVD.

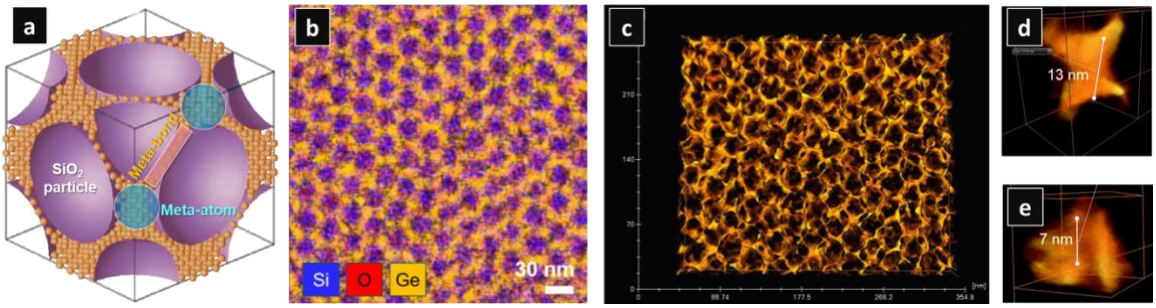

Figure 1.2. a) 3D schematic representation of silica nanoparticle template infiltrated with Germanium (b) SEM-EDS image of 30 nm silica nanoparticle template infiltrated with Germanium (c) TEM tomography of a germanium metalattice after removal of the template (d) and (e) Different voids/meta-atoms in the germanium metalattice as observed by TEM tomography (Reprinted with permission from Dr. Hiu Yan Cheng)

1.1.5 Synthesis and assembly of silica nanoparticle templates

Silica nanoparticles make an excellent candidate for particle-based templates due to their high monodispersity, low cost and simple synthesis, surface functionalization, colloidal stability and easy template removal post infiltration. The synthesis of spherical silica particles has been known and developed since Stober *et al.* proposed ammonia catalyzed hydrolysis of silicon alkoxides in a water-alcohol medium in 1968[25]. The sol-gel method proposed consists of two main steps (equation 1 and 2) – hydrolysis of the silica precursor and its subsequent condensation to form a crosslinked network which eventually becomes a particle.

$$Si(OR)_4 + H_2O \rightarrow Si(OR)_3OH + ROH - (1)$$

$$2Si(OR)_3OH \rightarrow Si(OR)_3O - OSi(OR)_3 + H_2O - (2)$$

The size and dispersity of the obtained particles are a function of the reaction conditions – temperature, pH, reaction concentrations/relative ratios of reactants[26–29]. Based on reaction kinetics studies, the seeded regrowth approach has been developed further to control the size and dispersity of the particles. The regrowth method separates the nucleation and growth events by performing seed synthesis first and then growing these seeds into desired size particles under controlled reaction conditions[26,30]. The Stober method and its modifications have been since optimized to synthesize silica nanoparticles of sizes in the range of hundreds of nanometers to a few microns, with dispersity decreasing with increasing particle size (going as low as 3%).

Although it is tunable and applicable to synthesizing a wide range of silica particles, this method cannot be extended to monodisperse particles with less than 4% standard deviation in the sub-100 nm regime. A reverse microemulsion approach (water-in-oil) which had shown promise for synthesis of particles for several materials (metals, chalcogenides, oxides), was attempted in the silica system to synthesize sub-100 nm particles[31,32]. The microemulsion approach also involves hydrolysis of silica precursors (for example, tetraethylorthosilicate) in water catalyzed by ammonia. However, hydrolysis and condensation occur in water droplets confined in the aggregates of surfactant molecules in the oil phase (cyclohexane). The molar ratio of water and surfactant, and the ammonium hydroxide concentration, play a crucial role in controlling particle size and dispersity. Particles with diameters between 30-70 nm were synthesized using this approach. However, the removal of non-polar organic solvents and a high loading of surfactants limited the use of this method.

A significant development in the synthesis of sub-100 nm silica nanoparticles was made by using amino acids (lysine and arginine) as catalysts for the hydrolysis of silica precursors[33,34]. There are two significant effects of amino acids that help in size control in

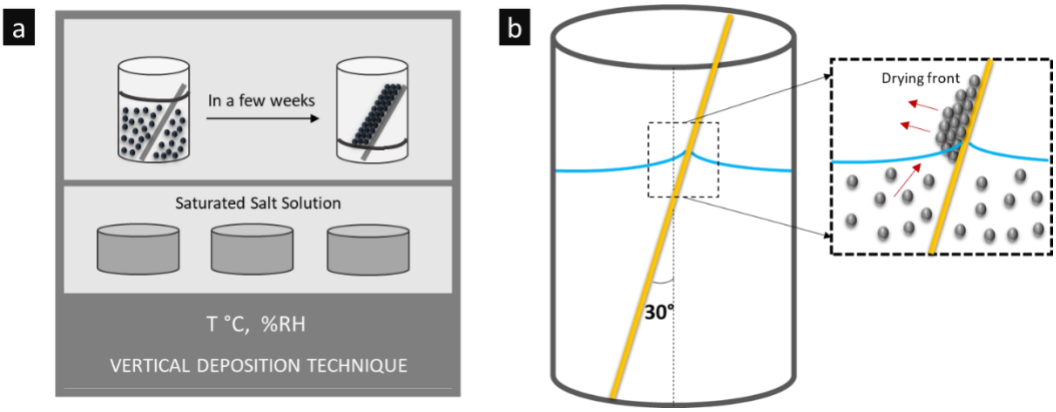

Figure 1.3. Schematic representation of (a) the set-up for silica colloidal crystal deposition on Si wafer using vertical deposition technique (b) particles assembling at the interface. Reprinted from *ACS Appl. Mater. Interfaces* 2022, copyright 2022 American Chemical Society.

the sub-100 nm regime. First, the amino acids provide buffer conditions (pH 9-10), which decrease the hydrolysis rate and decrease silicate species' solubility. Thus, the silicate species slowly hydrolyzed in the solution are more likely to react with existing particles via condensation than to nucleate new particles. This diffusion-controlled growth as opposed to reaction-controlled growth in the Stober process gives more control of the particle size. Second, the protonated amine groups of the amino acids electrostatically interact with the deprotonated surface silanol groups on the silica particle surface. This interaction and the constant pH value due to the buffering action of amino acids maintains the high negative zeta potential of the silica particles, causing them to form a stable dispersion. Further, the hydrogen bonding between the amino acids present on the silica particle surface helps create periodically ordered structures during self-assembly.

The amino acid-catalyzed synthesis of silica particles was further developed by Hartlen *et al.*[35] and Watanabe *et al*.[36] to prepare silica particles in the range of 14-550 nm and assemble them into colloidal crystals. Both the researchers implemented arginine catalyzed hydrolysis of silicon alkoxides in aqueous media and also used a seeded

regrowth approach to gain control of the particle size. Watanabe *et al.* developed a single-phase emulsion approach by combining the Stober method of using an ethanol-water mixture but replaced ammonia with arginine as the catalyst to synthesize particles with diameters between 14 nm and 550 nm. In contrast, Hartlen *et al.* used a bi-phasic reaction to further tune the particle size and dispersity. A cyclohexane layer was formed on top of the aqueous reaction mixture and silicon alkoxide was added to this cyclohexane layer. This physically decreased the rate of adding the silica precursor into the aqueous mixture, thereby reducing the rate of hydrolysis and providing more control over nucleation and growth of the particles. We have implemented the methods developed by Hartlen and Watanabe in this thesis work with slight modifications to obtain silica particles of sizes 20 nm, 25 nm, 35 nm, 50 nm, 70 nm, and 120 nm.

This dissertation used the vertical deposition technique to assemble the as-synthesized silica nanoparticles into 3D colloidal crystals on different substrates: silicon, quartz, sapphire, and silica capillaries. The vertical deposition technique involves the self-

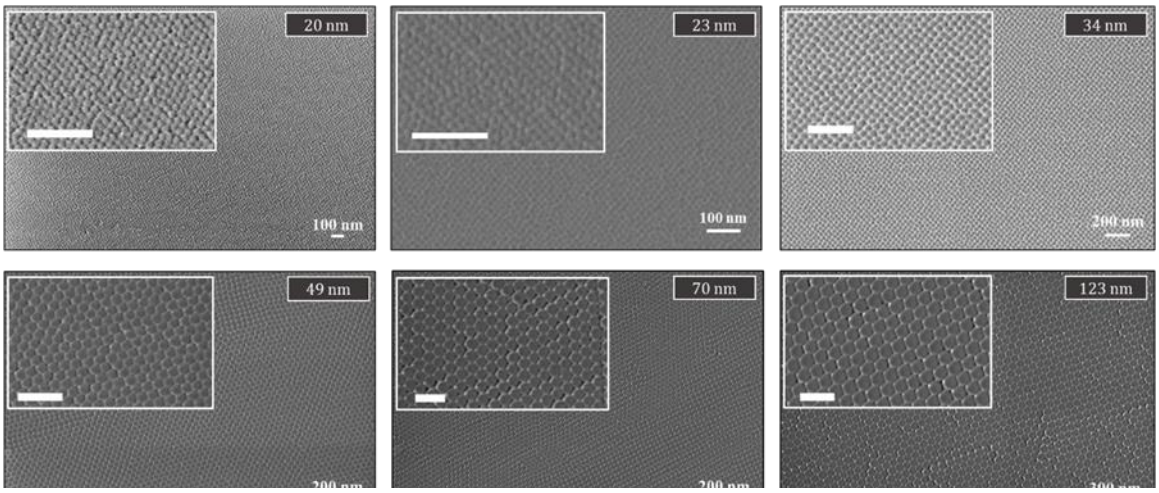

Figure 1.4. Top view of silica nanoparticle assembled as multilayer films on Si wafer by vertical deposition technique. Inset shows magnified images with the same scale bar as the parent image. Reprinted from *ACS Appl. Mater. Interfaces* 2022, copyright 2022 American Chemical Society.

assembly of particles on a substrate at the air-water interface as the solvent evaporates. Capillary forces acting at the meniscus along with the convex flow influence particle deposition[37,38].

This method has been widely used to create large-scale crystalline films of spherical and non-spherical particles in size range of a few nanometers to a few microns. The quality of the film is controlled by tuning the rate of meniscus movement with respect to particle sedimentation. This is achieved by controlling the deposition conditions such as temperature, humidity, air pressure, solvent, and the position of the substrate with respect to the solvent. In comparison with other deposition techniques, vertical deposition is a low-cost and scalable method to generate large-scale colloidal crystals on various substrates[39–41]. However, the films obtained from vertical deposition have non-uniform thickness across different deposition levels, as shown in Figure 1.3. This variation becomes concerning when optimizing methods to infiltrate the pores in the silica templates.

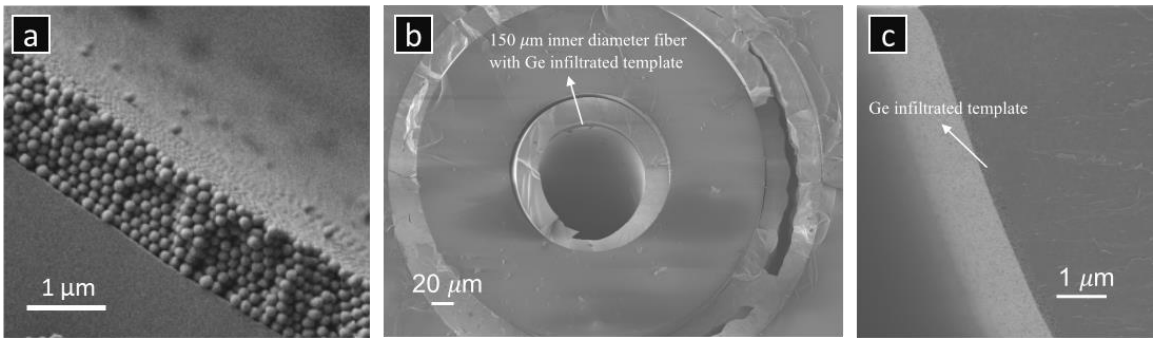

Figure 1.5. (a) Silica nanoparticle assembled in a 150 µm silica capillary. (b) Silica template infiltrated with Germanium using HPCVD and (c) magnified image of b.

Our set-up for silica nanoparticle assembly consisted of a temperature-controlled oven (40 °C-60 °C). The relative humidity (70-80%) was controlled using the saturated salt solution, and the substrate was placed at an angle of 30 degrees[23,42]. First, all the substrates were

cleaned using Piranha solution before deposition. Then, the deposition was carried out for ~two weeks until the entire solution evaporated, and the obtained films were sintered at 600 °C to remove any organic residues. Figure 1.4 and 1.5 shows SEM images of different sizes assembled on silicon wafers and 100 nm particles in silica capillaries. These silica nanoparticle templates were then infiltrated with metals and semiconductors using HPCVD to obtain metalattices. The advantage of silica colloidal crystals inside capillaries over a planar substrate is the directional flow of gas molecules, allowing for easier removal of byproducts and confinement effects on silica assembly. This dissertation will focus on a detailed description of deposition conditions on planar substrates and the structure of particle arrangement on silicon for different particle sizes (Chapter 3).

1.1.6 High-pressure infiltration of silica nanoparticle templates

The silica nanoparticle templates in the range of particle diameters (14-120 nm) and particle 3D arrangements studied here contain voids between 3 and 60 nm. These nanoscale voids are interconnected and also form a 3D network. In such high aspect ratio geometries with confined pores, infiltrating electronic grade semiconductors is a challenge. Conventional chemical vapor deposition is often used to conformally deposit high purity semiconductors from gas-phase precursors as thin films on various substrates[43]. A slight pressure gradient drives the diffusion of gas molecules towards the substrate during deposition. However, in conventional/low-pressure CVD, the mean free path of gas molecules is several hundreds of nanometers. In the case of pores smaller than the mean free path, the transport of gas molecules is controlled by effusion which severely limits gas transport through the entire pore volume. This eventually leads to incomplete infiltration as a film is formed on the outer surface of the pores before the inner pore volume is filled, and this blocks further transport of gas molecules. However,

decreasing the mean free path of the gas molecules can address this problem and allow for the complete infiltration of nanopores. Badding *et al*. developed high-pressure chemical vapor deposition, which, as the name suggests, uses high pressure to decrease gas molecules' mean free path, allowing them to deposit high purity semiconductors (Si, Ge, ZnSe) in optical fiber templates containing nano and micropores[44,45]. A modified version of this method which used both high pressure and reactor confinement to reduce mean free path and prevent clogging of pores was used to infiltrate semiconductors in the nanoscale voids of the silica template[21,22,46,47]. Figure 1.6 shows changes in the mean free path as a function of pressure and reactor confinement. The semiconductor metalattices were infiltrated in the voids of silica template by pyrolysis of respective gaseous precursor (silane/germane) transported with a carrier gas (hydrogen/helium) as shown in equation 3.

$$GeH_4 \rightarrow Ge + 2H_2 - (3)$$

This reaction generates hydrogen gas as a by-product which diffuses out, leaving behind amorphous semiconductors in the voids. Thermal annealing is then performed to obtain a polycrystalline metalattice. Both TEM tomography as a microscopic technique and positronium annihilation lifetime spectroscopy as a bulk measurement have confirmed the void-free infiltration of the silica templates planar substrates for semiconductor metalattices[48].

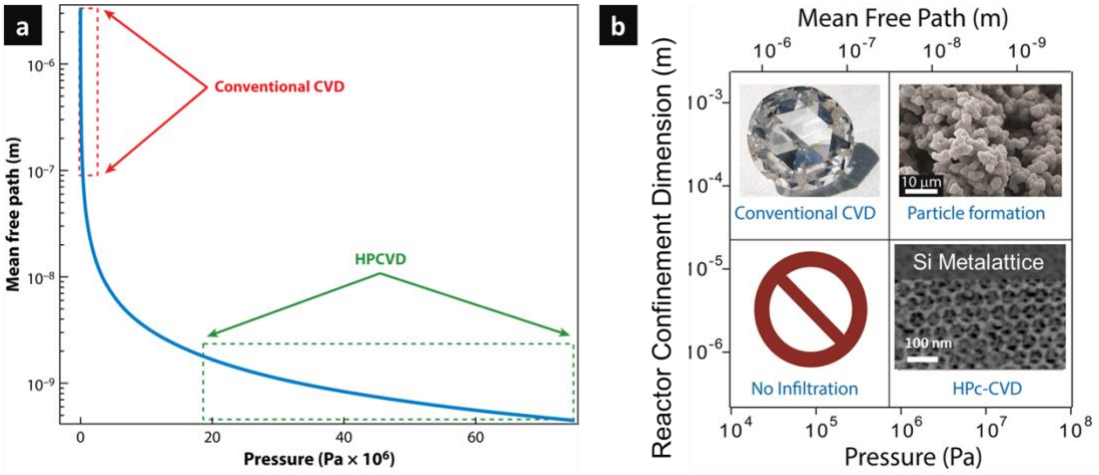

Figure 1.6. Mean free path as a function of (a) pressure, reprinted from Annual Review of Materials Research 43 (2013): 527-557, copyright 2013, Annual Review of Materials Research (b) reactor confinement and pressure, reprinted with permission from Dr. Hiu Yan Cheng.

This dissertation will discuss the chemical passivation of germanium metalattices in Chapter 2 and the detailed synthesis and structural characterization of silica nanoparticle template and metalattices in Chapter 3.

1.2 Synthesis and exfoliation of layered materials

1.2.1 Layered materials – their intercalation and exfoliation

Layered materials, which have been studied by chemists for over ~150 years, make an exciting class of compounds due to their anisotropic bonding. Layered materials consist of 2D host layers which have strong bonding in-plane within the layer but are weakly bonded out of the plane with the adjacent layers. This anisotropic interaction allows for intercalation chemistry between the layers and exfoliation of the 2D host layers as nanosheets[49–56]. The intercalation chemistry and exfoliation of a particular layered material are a function of the bonding strength between the adjacent layers, charge, and chemical composition of the 2D layer.

Several approaches have been developed to intercalate layered materials including electrochemical intercalation, vapor phase intercalation, or liquid-phase intercalation[49–52,56]. The earliest used technique is the vapor phase intercalation which involves temperature-controlled vapor transport of intercalants into the host material. A popular example of this method is the intercalation of graphene/TMDs with alkali metals ions[57] (Na, Li). The electrochemical method uses externally generated current to intercalate guest ions into host layers which act as the cathode and/or anode. Reversal of the direction of the applied current can lead to deintercalation and therefore this method is extensively used in energy storage devices such as secondary batteries[58,59]. In the case of the liquid phase method, intercalant ions and host material are both present in a liquid medium, and unlike the electrochemical method, the host and guest materials do not need to be conductive. The driving force for intercalation in the liquid phase is a stronger interaction between the host layer and guest molecules (electrostatic, charge-transfer) compared to the interaction between the adjacent layers. A significant advantage of this method is that it can be readily scaled for larger volumes. Some common examples of systems where this method has been applied are Li intercalation through n-butyl lithium solution in transition metal dichalcogenides[57], and intercalation of organic molecules such as dimethylformamide in MXenes[60]. This method is also commonly used to exchange ions in the interlayer gallery by another thermodynamically competitive ion in the solution, for example, proton exchange with bulky tetrabutylammonium ions in protonated titanates[61]. This dissertation uses the liquid intercalation method to exchange the interlayer anion and control the spacing between the layers of three types of layered double hydroxides (LDHs) – Co-Al LDH, Mg-Al LDH, and Zn-Al LDH.

Intercalation is also used as an intermediate step to exfoliate layered materials into 2D nanosheets. Exfoliated 2D nanosheets have physical and chemical properties different

from their bulk counterparts due to high surface area, confinement effects, and anisotropy. A wide range of 2D materials has emerged in the last few decades from different types of layered materials – graphite, hexagonal boron nitride, transition metal di(tri)chalcogenides, metal halides, oxides, hydroxides, clays, metal carbides and nitrides. Due to their novel properties, 2D materials have been used in transistors, thermoelectrics, superconducting composites, batteries, supercapacitors, catalysts, ferroelectrics, dielectrics, light-emitting diodes, electrochromics, non-linear optical materials, drug delivery materials, dye-sensitized solar cells, lightweight composites, electronic conductors and bio-composites.

These 2D materials can be obtained by exfoliation of their parent layered materials. There are two broad categories of exfoliation methods – micromechanical exfoliation[62] (Scotch-tape method) and liquid phase intercalation[53,63]. Within liquid phase intercalation, there are a lot of variants – mechanical liquid exfoliation, ion-exchange/displacement assisted exfoliation, selective erosion assisted exfoliation, and oxidation assisted exfoliation. In this dissertation, ion intercalation/exchange liquid phase exfoliation has been implemented to obtain nanosheets of layered silicates and layered double hydroxides. The general principle governing ion exchange exfoliation is the expansion of the interlayer gallery space by intercalating bulky ions or ions which bring in large quantities of solvent molecules leading to swelling of the host material (Figure 1.7). The swelling decreases the attraction between the 2D host layers which can then be delaminated/exfoliated by application of external forces such as shear and/or sonication[53,61].

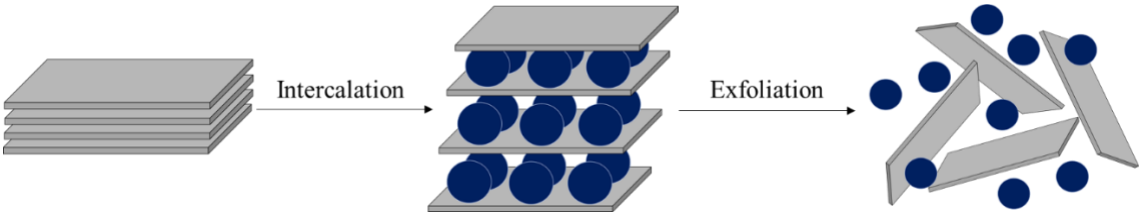

Figure 1.7. Schematic representation of the exfoliation of layered materials by intercalation.

1.2.2 Layered materials in this dissertation – NaTSM and layered double hydroxides

2:1 Layered silicate –Sodium flurotetrasilicic mica (NaTSM): 2:1 Layered silicates are a type of clay minerals that have 2D layers made up of stacked tetrahedral and octahedral

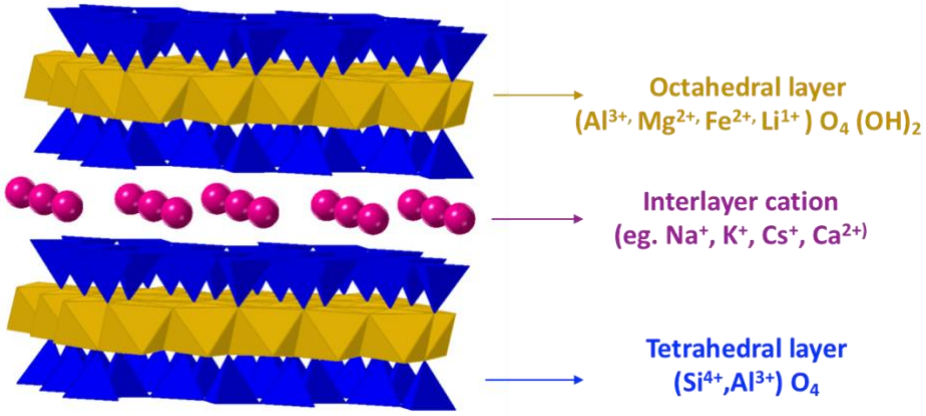

sheets. The building blocks of tetrahedral and octahedral sheets are four-coordinated Si/Al and six-coordinated Al/Mg/Fe/Li, respectively. In a T-O-T clay the octahedral sheet is sandwiched between two tetrahedral sheets, as shown in Figure 1.8. The isomorphic substitution in these sheets creates a charge deficit balanced by the presence of charged ions such as Na^+ in the interlayer gallery between the 2D layers.

Figure 1.8. Schematic representation of 2:1 layered silicates

Layered silicates are used to synthesize composites with polymers and nanoparticles, intercalation compounds, pillared materials, zeolites and mesoporous structures[64,65].

These varying forms of layered silicates/materials obtained from layered silicates have found applications in CO_2 adsorption, drug delivery, flame retardancy, gas sensing, catalysis and electronics[66–68]. NaTSM is a synthetic 2:1 layered silicate with the formula $Na_{0.66}Mg_{2.68}(Si_{3.98}Al_{0.02})O_{10.02}F_{1.96}$[69]. In this dissertation, we have used pre-synthesized NaTSM to obtain negatively charged nanosheets by exfoliation.

Layered Double Hydroxides: Commonly referred to as hydrotalcite-like anionic clays, layered double hydroxides are a type of layered materials that have positively charged brucite-like layers and charge-compensating anions and solvent molecules in the interlayer galleries[70] (Figure 1.9). They have a general formula of $[M_{1-x}^{2+}M_x^{3+}(OH)_2]^{x+}[A_{x/n}]^{n-}\cdot mH_2O$ where M^{2+} is a divalent metal ion like Mg, Zn, Co, or Ni, and M^{3+} is a trivalent metal ion like Al^{3+}, Fe^{3+}, or Mn^{3+}. The range of x can vary between ~0.17-0.33. Hydroxyl groups octahedrally coordinate M^{2+} and M^{3+}, and the excess M^{3+} ions impart the positive charge to the sheets. A^{n-} are organic/inorganic anions like CO_3^{2-}, Cl^-, NO_3^-, and SO_4^{3-}.

LDHs have gained popularity due to their ease of synthesis, positively charged 2D host layers, surface hydroxyl groups, exchangeable interlayer anions, tunable interlayer galleries, high chemical and thermal stability, and biocompatibility. These characteristics have led to their widespread applications in catalysis[71,72], anion conduction/exchange/selectivity[73–77], adsorbents[69], cosmetic formulations[78], polymer composites[79], separation systems for waste removal[80,81], hosts for biomolecules[82,83], and drug delivery[84–87].

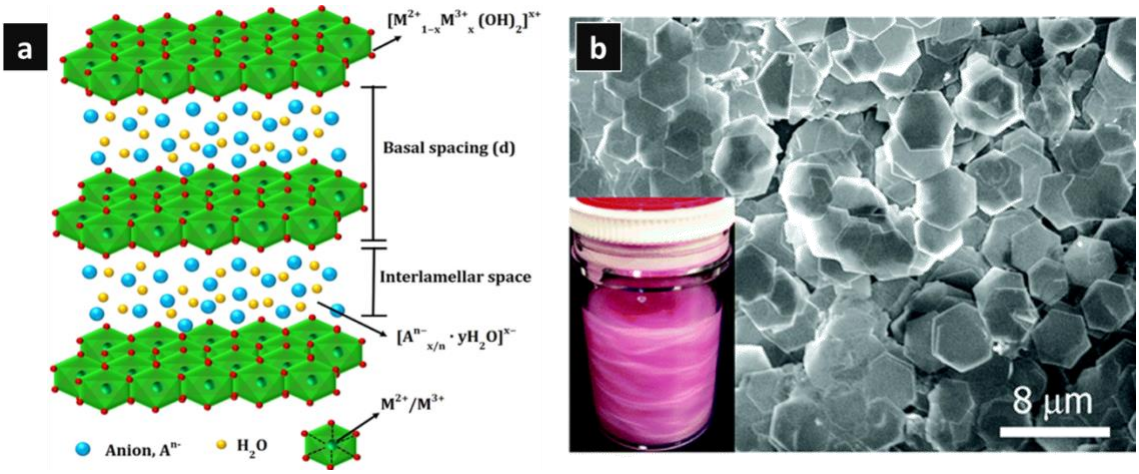

Figure 1.9. (a) LDH structure with CO_3^{2-} as the interlayer anion. Reprinted from (84), copyright 2018 Elsevier. (b) SEM image of Co-Al-CO_3^{2-} LDH platelet (inset of colloidal suspension). Reprinted from (95), copyright 2007 American Chemical Society.

Synthesis of LDHs - Several approaches have been developed to synthesize different divalent and trivalent metal-containing LDHs. The traditional method uses a solution-based process that involves mixing of divalent and trivalent metal salts in an alkaline environment created by the addition of NaOH or Na_2CO_3. The obtained gel-like precipitate is aged with heating to obtain crystalline LDHs. This method is defined as the co-precipitation method. To improve the crystallinity and size of the LDH platelets, a homogeneous precipitation method has been developed in which the alkalinity in the mixed salt solution is created by slow hydrolysis of urea/hexamethylenetetramine into ammonia[88–90]. This method allows for more controlled nucleation and growth of LDHs compared to the co-precipitation method, leading to more crystalline platelets. Some of the LDHs, which cannot be prepared directly from the above precipitation methods, are then designed by intercalation of the brucite-like metal hydroxide with an oxidant[91,92]. This method is called topochemical oxidation and has been useful for making non Al^{3+} LDHs with transition metals like Fe, Co, and Ni. For some LDHs, for example, Mg-Al LDH, it has

been noted that performing the mixed salt solution reaction under hydrothermal conditions gives improved crystallinity and larger platelets[88]. In this thesis work, we have used the homogeneous precipitation method to prepare Zn-Al LDH and Co-Al LDH. Mg-Al LDHs was prepared by using hydrothermal synthesis.

Ion exchange and exfoliation - The most common anion in the LDHs prepared by the approaches mentioned above are carbonate due to its exceptionally high affinity to the host layers and thereby facilitating the formation of highly crystalline LDHs. Although LDH's with other anions such as chloride[77] and dodecyl sulfate[93] have been made by creating a CO_2-free environment, the crystallinity of the obtained LDHs is poor. Therefore, another approach commonly used to add different anions is the ion exchange method (discussed in section 1.1.1) which uses highly crystalline carbonate-containing LDH and exchanges it with chloride anions by a salt-acid (NaCl-HCl) treatment[90,94,95]. The intercalated chloride anion, unlike carbonate, can be easily exchanged by other anions

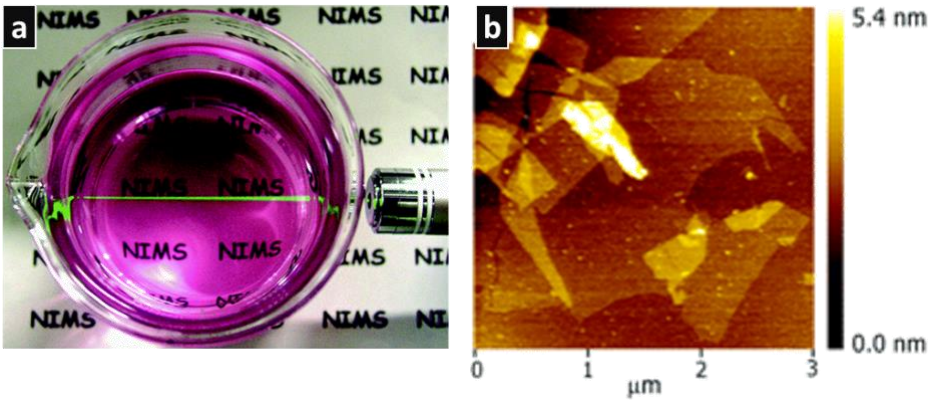

Figure 1.10. (a) Photograph of a Co-Al LDH nanosheet solution demonstrating Tyndall effect (b) AFM image of Co-Al LDH nanosheets. Reprinted from (90), copyright 2006 American Chemical Society

such as NO_3^-, SO_4^{3-}, ClO_4^- by treatment with their corresponding sodium and potassium salts[95].

The high affinity of carbonate to LDH host layers and the high charge density of the layers makes it challenging to exfoliate them into nanosheets. Therefore, LDHs with other anions with higher interlayer spacing like dodecyl sulfate or nitrate are used for delamination/exfoliation. Different solvents have been explored to exfoliate LDHs with different anions such as alcohols (butanol, hexanol, octanol, decanol), toluene, CCl_4, xylene, and water[93,96–101]. In the above-mentioned solvents, external sonication/heating was required to facilitate exfoliation. LDH crystallinity, lateral size, and exfoliation treatments affect the obtained nanosheets. LDHs synthesized using the co-precipitation method and with the above-discussed methods and solvents only provided nanosheets with a few tens of nanometer lateral size. A breakthrough in exfoliating LDHs was achieved by using formamide as a solvent for highly crystalline LDHs synthesized by the homogeneous precipitation method[90,102]. The carbonate in the as-synthesized LDH was exchanged with NO_3^- before exfoliation. Mechanical shaking in formamide for 1-2 days was sufficient to exfoliate these crystals into nanosheets with lateral sizes in the range of microns[90,102] (Figure 1.10).

The mechanism of this exfoliation is believed to be two-step as in other layered materials – swelling and exfoliation[61,103]. The water molecules in the interlayer gallery are replaced by formamide molecules, which have two electronegative atoms, making it an excellent candidate for hydrogen bonding with the host hydroxyl groups through the carbonyl group. However, formamide does not bond so effectively with the nitrate in the gallery. This leads to ‘osmotic swelling’ of the LDH structure, which under mechanical shaking exfoliates into 2D nanosheets. The sheets will restack if water is added due to the restoration of the hydrogen bonding network[90,104].

In this dissertation, we have synthesized three types of LDH with three different interlayer anions (CO_3^{2-}, Cl^-, NO_3^-). Chapter 4 discusses a potential method for controlled assembly of positively charged LDH sheets obtained from Co-Al LDH with negatively charged NaTSM sheets. Chapter 5 discusses the synthesis of Mg-Al and Zn-Al LDHs, their ion exchange to obtain different interlayer ions (chloride and nitrate), water loss from their interlayer gallery, and method development for ionic conductivity measurement between temperatures 100-250 °C to test their feasibility in intermediate temperature electrochemical cells.

1.3 References

(1) Kadic, M.; Milton, G. W.; van Hecke, M.; Wegener, M. 3D Metamaterials. *Nat. Rev. Phys. 2019 13* **2019**, *1* (3), 198–210. https://doi.org/10.1038/s42254-018-0018-y.

(2) Liu, Y.; Zhang, X. Metamaterials: A New Frontier of Science and Technology. *Chem. Soc. Rev.* **2011**, *40* (5), 2494–2507. https://doi.org/10.1039/C0CS00184H.

(3) Smith, D. R.; Pendry, J. B.; Wiltshire, M. C. K. Metamaterials and Negative Refractive Index. *Science (80-.).* **2004**, *305* (5685), 788–792. https://doi.org/10.1126/science.1096796.

(4) Liu, N.; Guo, H.; Fu, L.; Kaiser, S.; Schweizer, H.; Giessen, H. Three-Dimensional Photonic Metamaterials at Optical Frequencies. *Nat. Mater. 2008 71* **2007**, *7* (1), 31–37. https://doi.org/10.1038/nmat2072.

(5) Iwanaga, M. Photonic Metamaterials: A New Class of Materials for Manipulating Light Waves. *http://www.tandfonline.com/action/journalInformation?show=aimsScope&journalCode=tsta20#.VmBmuzZFCUk* **2012**, *13* (5), 17. https://doi.org/10.1088/1468-6996/13/5/053002.

(6) Joannopoulos, J. D.; Villeneuve, P. R.; Fan, S. Photonic Crystals: Putting a New Twist on Light. *Nat. 1997 3866621* **1997**, *386* (6621), 143–149. https://doi.org/10.1038/386143a0.

(7) El-Sayed, M. A. Small Is Different: Shape-, Size-, and Composition-Dependent Properties of Some Colloidal Semiconductor Nanocrystals. *Acc. Chem. Res.* **2004**, *37* (5), 326–333.

https://doi.org/10.1021/AR020204F.

(8) El-Sayed, M. A. Some Interesting Properties of Metals Confined in Time and Nanometer Space of Different Shapes. *Acc. Chem. Res.* **2001**, *34* (4), 257–264. https://doi.org/10.1021/AR960016N.

(9) Kagan, C. R.; Murray, C. B. Charge Transport in Strongly Coupled Quantum Dot Solids. *Nat. Nanotechnol. 2015 1012* **2015**, *10* (12), 1013–1026. https://doi.org/10.1038/NNANO.2015.247.

(10) Wang, Y.; Herron, N. Nanometer-Sized Semiconductor Clusters: Materials Synthesis, Quantum Size Effects, and Photophysical Properties. *J. Phys. Chem.* **2002**, *95* (2), 525–532. https://doi.org/10.1021/J100155A009.

(11) Takeoka, S.; Fujii, M.; Hayashi, S.; Yamamoto, K. *Size-Dependent near-Infrared Photoluminescence from Ge Nanocrystals Embedded in SiO 2 Matrices*; 1998.

(12) Chen, Z.; Moore, J.; Radtke, G.; Sirringhaus, H.; O'Brien, S. Binary Nanoparticle Superlattices in the Semiconductor-Semiconductor System: CdTe and CdSe. *J. Am. Chem. Soc.* **2007**, *129* (50), 15702–15709. https://doi.org/10.1021/JA076698Z/SUPPL_FILE/JA076698ZSI20071012_014347.TIF.

(13) Si, K. J.; Chen, Y.; Shi, Q.; Cheng, W. Nanoparticle Superlattices: The Roles of Soft Ligands. *Adv. Sci.* **2018**, *5* (1), 1700179. https://doi.org/10.1002/advs.201700179.

(14) Vanmaekelbergh, D.; Liljeroth, P. Electron-Conducting Quantum Dot Solids: Novel Materials Based on Colloidal Semiconductor Nanocrystals. *Chemical Society Reviews*. April 2005, pp 299–312. https://doi.org/10.1039/b314945p.

(15) Vanmaekelbergh, D.; Liljeroth, P. Electron-Conducting Quantum Dot Solids: Novel Materials Based on Colloidal Semiconductor Nanocrystals. *Chem. Soc. Rev.* **2005**, *34* (4), 299–312. https://doi.org/10.1039/B314945P.

(16) Armatas, G. S.; Kanatzidis, M. G. Hexagonal Mesoporous Germanium. *Science (80-.).* **2006**, *313* (5788), 817–820. https://doi.org/10.1126/science.1130101.

(17) Armatas, G. S.; Kanatzidis, M. G. Size Dependence in Hexagonal Mesoporous Germanium:

Pore Wall Thickness versus Energy Gap and Photoluminescence. *Nano Lett.* **2010**, *10* (9), 3330–3336. https://doi.org/10.1021/nl101004q.

(18) Agger, J. R.; Anderson, M. W.; Pemble, M. E.; Terasaki, O.; Nozue, Y. Growth of Quantum-Confined Indium Phosphide inside MCM-41. *J. Phys. Chem. B* **1998**, *102* (18), 3345–3353. https://doi.org/10.1021/JP972994U.

(19) Besson, S.; Gacoin, T.; Ricolleau, C.; Jacquiod, C.; Boilot, J. P. 3D Quantum Dot Lattice Inside Mesoporous Silica Films. *Nano Lett.* **2002**, *2* (4), 409–414. https://doi.org/10.1021/NL015685V.

(20) Brieler, F. J.; Grundmann, P.; Fröba, M.; Chen, L.; Klar, P. J.; Heimbrodt, W.; Von Nidda, H. A. K.; Kurz, T.; Loidl, A. Formation of Zn1-XMnxS Nanowires within Mesoporous Silica of Different Pore Sizes. *J. Am. Chem. Soc.* **2004**, *126* (3), 797–807. https://doi.org/10.1021/JA038960J.

(21) Chen, Y.; Liu, Y.; Moradifar, P.; Glaid, A. J.; Russell, J. L.; Mahale, P.; Yu, S.-Y.; Culp, T. E.; Kumar, M.; Gomez, E. D.; Mohney, S. E.; Mallouk, T. E.; Alem, N.; Badding, J. V.; Liu, Y. Quantum Transport in Three-Dimensional Metalattices of Platinum Featuring an Unprecedentedly Large Surface Area to Volume Ratio. *Phys. Rev. Mater.* **2020**, *4* (3), 035201. https://doi.org/10.1103/physrevmaterials.4.035201.

(22) Liu, Y.; Kempinger, S.; He, R.; Day, T. D.; Moradifar, P.; Yu, S. Y.; Russell, J. L.; Torres, V. M.; Xu, P.; Mallouk, T. E.; Mohney, S. E.; Alem, N.; Samarth, N.; Badding, J. V. Confined Chemical Fluid Deposition of Ferromagnetic Metalattices. *Nano Lett.* **2018**, *18* (1), 546–552. https://doi.org/10.1021/acs.nanolett.7b04633.

(23) Mahale, P.; Moradifar, P.; Cheng, H. Y.; Nova, N. N.; Grede, A. J.; Lee, B.; De Jesús, L. R.; Wetherington, M.; Giebink, N. C.; Badding, J. V.; Alem, N.; Mallouk, T. E. Oxide-Free Three-Dimensional Germanium/Silicon Core-Shell Metalattice Made by High-Pressure Confined Chemical Vapor Deposition. *ACS Nano* **2020**. https://doi.org/10.1021/acsnano.0c03559.

(24) Chen, W.; Talreja, D.; Eichfeld, D.; Mahale, P.; Nova, N. N.; Cheng, H. Y.; Russell, J. L.; Yu, S.-Y.; Poilvert, N.; Mahan, G.; Mohney, S. E.; Crespi, V. H.; Mallouk, T. E.; Badding, J.

V.; Foley, B.; Gopalan, V.; Dabo, I. Achieving Minimal Heat Conductivity by Ballistic Confinement in Phononic Metalattices. *ACS Nano* **2020**, acsnano.9b09487. https://doi.org/10.1021/acsnano.9b09487.

(25) Stöber, W.; Fink, A.; Bohn, E. Controlled Growth of Monodisperse Silica Spheres in the Micron Size Range. *J. Colloid Interface Sci.* **1968**, *26* (1), 62–69. https://doi.org/10.1016/0021-9797(68)90272-5.

(26) Van Blaaderen, A.; Van Geest, J.; Vrij, A. Monodisperse Colloidal Silica Spheres from Tetraalkoxysilanes: Particle Formation and Growth Mechanism. *J. Colloid Interface Sci.* **1992**, *154* (2), 481–501. https://doi.org/10.1016/0021-9797(92)90163-G.

(27) Ghimire, P. P.; Jaroniec, M. Renaissance of Stöber Method for Synthesis of Colloidal Particles: New Developments and Opportunities. *J. Colloid Interface Sci.* **2021**, *584*, 838–865. https://doi.org/10.1016/J.JCIS.2020.10.014.

(28) Han, Y.; Lu, Z.; Teng, Z.; Liang, J.; Guo, Z.; Wang, D.; Han, M. Y.; Yang, W. Unraveling the Growth Mechanism of Silica Particles in the Stöber Method: In Situ Seeded Growth Model. *Langmuir* **2017**, *33* (23), 5879–5890. https://doi.org/10.1021/ACS.LANGMUIR.7B01140/SUPPL_FILE/LA7B01140_SI_001.PDF .

(29) Nozawa, K.; Gailhanou, H.; Raison, L.; Panizza, P.; Ushiki, H.; Sellier, E.; Delville, J. P.; Delville, M. H. Smart Control of Monodisperse Stöber Silica Particles: Effect of Reactant Addition Rate on Growth Process. *Langmuir* **2004**, *21* (4), 1516–1523. https://doi.org/10.1021/LA048569R.

(30) Giesche, H. Synthesis of Monodispersed Silica Powders I. Particle Properties and Reaction Kinetics. *J. Eur. Ceram. Soc.* **1994**, *14*, 189–204.

(31) Arriagada, F. J.; Osseo-Asare, K. Synthesis of Nanosize Silica in a Nonionic Water-in-Oil Microemulsion: Effects of the Water/Surfactant Molar Ratio and Ammonia Concentration. *J. Colloid Interface Sci.* **1999**, *211* (2), 210–220. https://doi.org/10.1006/JCIS.1998.5985.

(32) Osseo-Asare, K.; Arriagada, F. J. Preparation of SiO2 Nanoparticles in a Non-Ionic Reverse

Micellar System. *Colloids and Surfaces* **1990**, *50* (C), 321–339. https://doi.org/10.1016/0166-6622(90)80273-7.

(33) Yokoi, T.; Wakabayashi, J.; Otsuka, Y.; Fan, W.; Iwama, M.; Watanabe, R.; Aramaki, K.; Shimojima, A.; Tatsumi, T.; Okubo, T. Mechanism of Formation of Uniform-Sized Silica Nanospheres Catalyzed by Basic Amino Acids. *Chem. Mater.* **2009**, *21* (15), 3719–3729. https://doi.org/10.1021/cm900993b.

(34) Davis, T. M.; Snyder, M. A.; Krohn, J. E.; Tsapatsis, M. Nanoparticles in Lysine-Silica Sols. *Chem. Mater.* **2006**, *18* (25), 5814–5816. https://doi.org/10.1021/CM061982V/SUPPL_FILE/CM061982VSI20061101_090253.PDF.

(35) Hartlen, K. D.; Athanasopoulos, A. P. T.; Kitaev, V. Facile Preparation of Highly Monodisperse Small Silica Spheres (15 to >200 Nm) Suitable for Colloidal Templating and Formation of Ordered Arrays. **2008**. https://doi.org/10.1021/la7025285.

(36) Watanabe, R.; Yokoi, T.; Kobayashi, E.; Otsuka, Y.; Shimojima, A.; Okubo, T.; Tatsumi, T. Extension of Size of Monodisperse Silica Nanospheres and Their Well-Ordered Assembly. *J. Colloid Interface Sci.* **2011**, *360* (1), 1–7. https://doi.org/10.1016/j.jcis.2010.09.001.

(37) Jiang, P.; Bertone, J. F.; Hwang, K. S.; Colvin, V. L. Single-Crystal Colloidal Multilayers of Controlled Thickness. **1999**. https://doi.org/10.1021/cm990080.

(38) Brewer, D. D.; Allen, J.; Miller, M. R.; Santos, J. M. D.; Kumar, S.; Norris, D. J.; Tsapatsis, M.; Scriven, L. E. Mechanistic Principles of Colloidal Crystal Growth by Evaporation-Induced Convective Steering. *Langmuir* **2008**, *24* (23), 13683–13693. https://doi.org/10.1021/LA802180D/SUPPL_FILE/LA802180D_SI_001.PDF.

(39) Ye, Y. H.; LeBlanc, F.; Haché, A.; Truong, V. Van. Self-Assembling Three-Dimensional Colloidal Photonic Crystal Structure with High Crystalline Quality. *Appl. Phys. Lett.* **2000**, *78* (1), 52. https://doi.org/10.1063/1.1337619.

(40) Blanco, A.; Chomski, E.; Grabtchak, S.; Ibisate, M.; John, S.; Leonard, S. W.; Lopez, C.; Meseguer, F.; Miguez, H.; Mondla, J. P.; Ozin, G. A.; Toader, O.; Van Driel, H. M. Large-Scale Synthesis of a Silicon Photonic Crystal with a Complete Three-Dimensional Bandgap

near 1.5 Micrometres. *Nature* **2000**, *405* (6785), 437–440. https://doi.org/10.1038/35013024.

(41) Hatton, B.; Mishchenko, L.; Davis, S.; Sandhage, K. H.; Aizenberg, J. Assembly of Large-Area, Highly Ordered, Crack-Free Inverse Opal Films. *Proc. Natl. Acad. Sci. U. S. A.* **2010**, *107* (23), 10354–10359. https://doi.org/10.1073/PNAS.1000954107/-/DCSUPPLEMENTAL.

(42) Russell, J. L.; Noel, G. H.; Warren, J. M.; Tran, N. L. L.; Mallouk, T. E. Binary Colloidal Crystal Films Grown by Vertical Evaporation of Silica Nanoparticle Suspensions. *Langmuir* **2017**, *33* (39), 10366–10373. https://doi.org/10.1021/acs.langmuir.7b02553.

(43) Chemical Vapour Deposition. **2008**. https://doi.org/10.1039/9781847558794.

(44) Sazio, P. J. A.; Amezcua-Correa, A.; Finlayson, C. E.; Hayes, J. R.; Scheidemantel, T. J.; Baril, N. F.; Jackson, B. R.; Won, D. J.; Zhang, F.; Margine, E. R.; Gopalan, V.; Crespi, V. H.; Badding, J. V. Microstructured Optical Fibers as High-Pressure Microfluidic Reactors. *Science (80-.).* **2006**, *311* (5767), 1583–1586. https://doi.org/10.1126/SCIENCE.1124281/SUPPL_FILE/SAZIO_SOM.PDF.

(45) Sparks, J. R.; Baril, N. F.; Keshavarzi, B.; Krishnamurthi, M.; Temnykh, I.; Sazio, P. J. A.; Peacock, A. C.; Borhan, A.; Gopalan, V.; Badding, J. V. High-Pressure Chemical Deposition for Void-Free Filling of Extreme Aspect Ratio Templates. *Adv. Mater.* **2010**, *22* (41), 4605–4611. https://doi.org/10.1002/adma.201001199.

(46) Chen, W.; Talreja, D.; Eichfeld, D.; Mahale, P.; Nova, N.; Cheng, H. Y.; Russell, J. L.; Yu, S.; Mahan, G. D.; Mohney, S. E.; Crespi, V. H.; Thomas, E.; Badding, J. V; Foley, B.; Gopalan, V. Achieving Minimal Heat Conductivity by Ballistic Confinement in Phononic Metalattices.

(47) Mahale, P.; Moradifar, P.; Cheng, H. Y.; Nova, N. N.; Grede, A. J.; Lee, B.; De Jesús, L. R.; Wetherington, M.; Giebink, N. C.; Badding, J. V.; Alem, N.; Mallouk, T. E. Oxide-Free Three-Dimensional Germanium/Silicon Core–Shell Metalattice Made by High-Pressure Confined Chemical Vapor Deposition. *ACS Nano* **2020**. https://doi.org/10.1021/acsnano.0c03559.

(48) Hiu Yan Cheng, Chemistry, E. college of S. HIGH PRESSURE CONFINED CHEMICAL VAPOR DEPOSITION OF ELECTRONIC METALATTICES AND SEMICONDUCTORS IN EXTREME GEOMETRIES, 2018. https://doi.org/10.1109/COMST.2015.2457491.

(49) Ma, R.; Sasaki, T. Nanosheets of Oxides and Hydroxides: Ultimate 2D Charge-Bearing Functional Crystallites. *Advanced Materials*. John Wiley & Sons, Ltd December 1, 2010, pp 5082–5104. https://doi.org/10.1002/adma.201001722.

(50) Wan, J.; Lacey, S. D.; Dai, J.; Bao, W.; Fuhrer, M. S.; Hu, L. Tuning Two-Dimensional Nanomaterials by Intercalation: Materials, Properties and Applications. *Chem. Soc. Rev.* **2016**, *45* (24), 6742–6765. https://doi.org/10.1039/C5CS00758E.

(51) Stark, M. S.; Kuntz, K. L.; Martens, S. J.; Warren, S. C. Intercalation of Layered Materials from Bulk to 2D. *Adv. Mater.* **2019**, *31* (27), 1808213. https://doi.org/10.1002/ADMA.201808213.

(52) Rajapakse, M.; Karki, B.; Abu, U. O.; Pishgar, S.; Musa, M. R. K.; Riyadh, S. M. S.; Yu, M.; Sumanasekera, G.; Jasinski, J. B. Intercalation as a Versatile Tool for Fabrication, Property Tuning, and Phase Transitions in 2D Materials. *npj 2D Mater. Appl. 2021 51* **2021**, *5* (1), 1–21. https://doi.org/10.1038/s41699-021-00211-6.

(53) Nicolosi, V.; Chhowalla, M.; Kanatzidis, M. G.; Strano, M. S.; Coleman, J. N. Liquid Exfoliation of Layered Materials. https://doi.org/10.1126/science.1194975.

(54) Zhang, H. Ultrathin Two-Dimensional Nanomaterials. *ACS Nano* **2015**, *9* (10), 9451–9469. https://doi.org/10.1021/ACSNANO.5B05040.

(55) Coleman, J. N.; Lotya, M.; O'Neill, A.; Bergin, S. D.; King, P. J.; Khan, U.; Young, K.; Gaucher, A.; De, S.; Smith, R. J.; Shvets, I. V.; Arora, S. K.; Stanton, G.; Kim, H. Y.; Lee, K.; Kim, G. T.; Duesberg, G. S.; Hallam, T.; Boland, J. J.; Wang, J. J.; Donegan, J. F.; Grunlan, J. C.; Moriarty, G.; Shmeliov, A.; Nicholls, R. J.; Perkins, J. M.; Grieveson, E. M.; Theuwissen, K.; McComb, D. W.; Nellist, P. D.; Nicolosi, V. Two-Dimensional Nanosheets Produced by Liquid Exfoliation of Layered Materials. *Science (80-.).* **2011**, *331* (6017), 568–571. https://doi.org/10.1126/SCIENCE.1194975.

(56) Zhou, J.; Lin, Z.; Ren, H.; Duan, X.; Shakir, I.; Huang, Y.; Duan, X.; Zhou, J.; Duan, X. D.; Lin, Z.; Ren, H.; Duan, X. F.; Shakir, I.; Huang, Y. Layered Intercalation Materials. *Adv. Mater.* **2021**, *33* (25), 2004557. https://doi.org/10.1002/ADMA.202004557.

(57) Jung, Y.; Zhou, Y.; Cha, J. J. Intercalation in Two-Dimensional Transition Metal Chalcogenides. *Inorg. Chem. Front.* **2016**, *3* (4), 452–463. https://doi.org/10.1039/C5QI00242G.

(58) Flandrois, S.; Masson, J. M.; Rouillon, J. C. Intercalation Compounds of Graphite with Nickel Chloride as Cathode Material for Alkaline Batteries. *Synth. Met.* **1981**, *3* (3–4), 195–200. https://doi.org/10.1016/0379-6779(81)90008-4.

(59) Inagaki, M. Applications of Graphite Intercalation Compounds. *J. Mater. Res.* **1989**, *4* (6), 1560–1568. https://doi.org/10.1557/JMR.1989.1560.

(60) Mashtalir, O.; Naguib, M.; Mochalin, V. N.; Dall'Agnese, Y.; Heon, M.; Barsoum, M. W.; Gogotsi, Y. Intercalation and Delamination of Layered Carbides and Carbonitrides. *Nat. Commun. 2013 41* **2013**, *4* (1), 1–7. https://doi.org/10.1038/ncomms2664.

(61) Sasaki, T.; Watanabe, M. Osmotic Swelling to Exfoliation. Exceptionally High Degrees of Hydration of a Layered Titanate. *J. Am. Chem. Soc.* **1998**, *120* (19), 4682–4689. https://doi.org/10.1021/JA974262L.

(62) Geim, A. K.; Novoselov, K. S. The Rise of Graphene. *Nat. Mater.* **2007**, *6* (3), 183–191. https://doi.org/10.1038/NMAT1849.

(63) Coleman, J. N.; Lotya, M.; O'Neill, A.; Bergin, S. D.; King, P. J.; Khan, U.; Young, K.; Gaucher, A.; De, S.; Smith, R. J.; Shvets, I. V.; Arora, S. K.; Stanton, G.; Kim, H. Y.; Lee, K.; Kim, G. T.; Duesberg, G. S.; Hallam, T.; Boland, J. J.; Wang, J. J.; Donegan, J. F.; Grunlan, J. C.; Moriarty, G.; Shmeliov, A.; Nicholls, R. J.; Perkins, J. M.; Grieveson, E. M.; Theuwissen, K.; McComb, D. W.; Nellist, P. D.; Nicolosi, V. Two-Dimensional Nanosheets Produced by Liquid Exfoliation of Layered Materials. *Science (80-.).* **2011**, *331* (6017), 568–571. https://doi.org/10.1126/science.1194975.

(64) Selvam, T.; Inayat, A.; Schwieger, W. Reactivity and Applications of Layered Silicates and

Layered Double Hydroxides. *Dalt. Trans.* **2014**, *43* (27), 10365–10387. https://doi.org/10.1039/C4DT00573B.

(65) Takahashi, N.; Kuroda, K. Materials Design of Layered Silicates through Covalent Modification of Interlayer Surfaces. *J. Mater. Chem.* **2011**, *21* (38), 14336–14353. https://doi.org/10.1039/C1JM10460H.

(66) Ahmadi, S. J.; Huang, Y. D.; Li, W. Synthetic Routes, Properties and Future Applications of Polymer-Layered Silicate Nanocomposites. *J. Mater. Sci. 2004 396* **2004**, *39* (6), 1919–1925. https://doi.org/10.1023/B:JMSC.0000017753.90222.96.

(67) Kaya, E.; Tanoğlu, M.; Okur, S. Layered Clay/Epoxy Nanocomposites: Thermomechanical, Flame Retardancy, and Optical Properties. *J. Appl. Polym. Sci.* **2008**, *109* (2), 834–840. https://doi.org/10.1002/APP.28168.

(68) Rodrigues, L. A. de S.; Figueiras, A.; Veiga, F.; de Freitas, R. M.; Nunes, L. C. C.; da Silva Filho, E. C.; da Silva Leite, C. M. The Systems Containing Clays and Clay Minerals from Modified Drug Release: A Review. *Colloids Surfaces B Biointerfaces* **2013**, *103*, 642–651. https://doi.org/10.1016/J.COLSURFB.2012.10.068.

(69) Hata, H.; Mallouk, T. E.; Kuroda, K. Color Tuning of an Acidic Blue Dye by Intercalation into the Basic Interlayer Galleries of a Poly(Allylamine)/Synthetic Fluoromica Nanocomposite. https://doi.org/10.1021/cm802664j.

(70) Wang, J.; Kalinichev, A. G.; Kirkpatrick, R. J.; Hou, X. Molecular Modeling of the Structure and Energetics of Hydrotalcite Hydration. *Chem. Mater.* **2000**, *13* (1), 145–150. https://doi.org/10.1021/CM000441H.

(71) Chen, G.; Wan, H.; Ma, W.; Zhang, N.; Cao, Y.; Liu, X.; Wang, J.; Ma, R. Layered Metal Hydroxides and Their Derivatives: Controllable Synthesis, Chemical Exfoliation, and Electrocatalytic Applications. *Adv. Energy Mater.* **2020**, *10* (11), 1–27. https://doi.org/10.1002/aenm.201902535.

(72) Deng, X.; Huang, J.; Wan, H.; Chen, F.; Lin, Y.; Xu, X.; Ma, R.; Sasaki, T. Recent Progress in Functionalized Layered Double Hydroxides and Their Application in Efficient

Electrocatalytic Water Oxidation. *Journal of Energy Chemistry*. Elsevier B.V. May 1, 2019, pp 93–104. https://doi.org/10.1016/j.jechem.2018.07.007.

(73) Sun, P.; Chen, F.; Zhou, W.; Liu, X.; Ma, R.; Sasaki, T. Superionic Conduction along Ordered Hydroxyl Networks in Molecular-Thin Nanosheets. *Mater. Horizons* **2019**, *6* (10), 2087–2093. https://doi.org/10.1039/c9mh00549h.

(74) Sun, P.; Ma, R.; Bai, X.; Wang, K.; Zhu, H.; Sasaki, T. Single-Layer Nanosheets with Exceptionally High and Anisotropic Hydroxyl Ion Conductivity. *Sci. Adv.* **2017**, *3* (4), e1602629. https://doi.org/10.1126/sciadv.1602629.

(75) Sun, P.; Ma, R.; Sasaki, T. Recent Progress on Exploring Exceptionally High and Anisotropic H+/OH- Ion Conduction in Two-Dimensional Materials. *Chemical Science*. Royal Society of Chemistry December 20, 2017, pp 33–43. https://doi.org/10.1039/c7sc04019a.

(76) Kim, H. S.; Yamazaki, Y.; Kim, J. D.; Kudo, T.; Honma, I. High Ionic Conductivity of Mg-Al Layered Double Hydroxides at Intermediate Temperature (100-200°C) under Saturated Humidity Condition (100% RH). *Solid State Ionics* **2010**, *181* (19–20), 883–888. https://doi.org/10.1016/j.ssi.2010.04.037.

(77) Hu, J.; Tang, X.; Dai, Q.; Liu, Z.; Zhang, H.; Zheng, A.; Yuan, Z.; Li, X. Layered Double Hydroxide Membrane with High Hydroxide Conductivity and Ion Selectivity for Energy Storage Device. *Nat. Commun. 2021 121* **2021**, *12* (1), 1–10. https://doi.org/10.1038/s41467-021-23721-9.

(78) Kesavan Pillai, S.; Kleyi, P.; de Beer, M.; Mudaly, P. Layered Double Hydroxides: An Advanced Encapsulation and Delivery System for Cosmetic Ingredients-an Overview. *Appl. Clay Sci.* **2020**, *199*, 105868. https://doi.org/10.1016/J.CLAY.2020.105868.

(79) Leroux, F.; Besse, J. Polymer Interleaved Layered Double Hydroxide: A New Emerging Class of Nanocomposites. *Chem. Mater.* **2001**, *13* (10), 3507–3515. https://doi.org/10.1021/CM0110268.

(80) Al Jaberi, M.; Mallet, M.; Greenwell, H. C.; Abdelmoula, M.; Ruby, C. Using CaFe Layered

Double Hydroxide Transformation to Optimise Phosphate Removal from Waste Waters. *Appl. Clay Sci.* **2019**, *182*, 105281. https://doi.org/10.1016/J.CLAY.2019.105281.

(81) Chen, D.; Li, Y.; Zhang, J.; Li, W.; Zhou, J.; Shao, L.; Qian, G. Efficient Removal of Dyes by a Novel Magnetic Fe3O4/ZnCr-Layered Double Hydroxide Adsorbent from Heavy Metal Wastewater. *J. Hazard. Mater.* **2012**, *243*, 152–160. https://doi.org/10.1016/J.JHAZMAT.2012.10.014.

(82) Costantino, U.; Ambrogi, V.; Nocchetti, M.; Perioli, L. Hydrotalcite-like Compounds: Versatile Layered Hosts of Molecular Anions with Biological Activity. *Microporous Mesoporous Mater.* **2008**, *107* (1–2), 149–160. https://doi.org/10.1016/J.MICROMESO.2007.02.005.

(83) Allou, N. B.; Saikia, P.; Borah, A.; Goswamee, R. L. Hybrid Nanocomposites of Layered Double Hydroxides: An Update of Their Biological Applications and Future Prospects. *Colloid Polym. Sci. 2017 2955* **2017**, *295* (5), 725–747. https://doi.org/10.1007/S00396-017-4047-3.

(84) Choy, J. H.; Jung, J. S.; Oh, J. M.; Park, M.; Jeong, J.; Kang, Y. K.; Han, O. J. Layered Double Hydroxide as an Efficient Drug Reservoir for Folate Derivatives. *Biomaterials* **2004**, *25* (15), 3059–3064. https://doi.org/10.1016/J.BIOMATERIALS.2003.09.083.

(85) Darder, M.; López-Blanco, M.; Aranda, P.; Leroux, F.; Ruiz-Hitzky, E. Bio-Nanocomposites Based on Layered Double Hydroxides. *Chem. Mater.* **2005**, *17* (8), 1969–1977. https://doi.org/10.1021/CM0483240.

(86) Alcântara, A. C. S.; Aranda, P.; Darder, M.; Ruiz-Hitzky, E. Bionanocomposites Based on Alginate – Zein /Layered Double Hydroxide Materials as Drug Delivery Systems. *J. Mater. Chem.* **2010**, *20* (42), 9495–9504. https://doi.org/10.1039/C0JM01211D.

(87) Khan, A. I.; Lei, L.; Norquist, A. J.; O'hare, D. Intercalation and Controlled Release of Pharmaceutically Active Compounds from a Layered Double Hydroxide. *Chem. Commun.* **2001**, *1* (22), 2342–2343. https://doi.org/10.1039/B106465G.

(88) Iyi, N.; Matsumoto, T.; Kaneko, Y.; Kitamura, K. A Novel Synthetic Route to Layered Double

Hydroxides Using Hexamethylenetetramine. *1122 Chem. Lett.* **2004**, *33* (9). https://doi.org/10.1246/cl.2004.1122.

(89) Iyi, N.; Ebina, Y.; Sasaki, T. Water-Swellable MgAl-LDH (Layered Double Hydroxide) Hybrids: Synthesis, Characterization, and Film Preparation. *Langmuir* **2008**, *24* (10), 5591–5598. https://doi.org/10.1021/la800302w.

(90) Liu, Z.; Ma, R.; Osada, M.; Iyi, N.; Ebina, Y.; Takada, K.; Sasaki, T. Synthesis, Anion Exchange, and Delamination of Co-Al Layered Double Hydroxide: Assembly of the Exfoliated Nanosheet/Polyanion Composite Films and Magneto-Optical Studies. *J. Am. Chem. Soc.* **2006**, *128* (14), 4872–4880. https://doi.org/10.1021/ja0584471.

(91) Liang, J.; Renzhi, M.; Iyi, N.; Ebina, Y.; Takada, K.; Sasaki, T. Topochemical Synthesis, Anion Exchange, and Exfoliation of Co-Ni Layered Double Hydroxides: A Route to Positively Charged Co-Ni Hydroxide Nanosheets with Tunable Composition. *Chem. Mater.* **2010**, *22* (2), 371–378. https://doi.org/10.1021/cm902787u.

(92) Ma, R.; Liang, J.; Liu, X.; Sasaki, T. General Insights into Structural Evolution of Layered Double Hydroxide: Underlying Aspects in Topochemical Transformation from Brucite to Layered Double Hydroxide. *J. Am. Chem. Soc.* **2012**, *134* (48), 19915–19921. https://doi.org/10.1021/ja310246r.

(93) Adachi-Pagano, M.; Forano, C.; Besse, J. P. Delamination of Layered Double Hydroxides by Use of Surfactants. *Chem. Commun.* **2000**, No. 1, 91–92. https://doi.org/10.1039/A908251D.

(94) Iyi, N.; Matsumoto, T.; Kaneko, Y.; Kitamura, K. Deintercalation of Carbonate Ions from a Hydrotalcite-like Compound: Enhanced Decarbonation Using Acid-Salt Mixed Solution. *Chem. Mater.* **2004**, *16* (15), 2926–2932. https://doi.org/10.1021/cm049579g.

(95) Zhaoping Liu; Renzhi Ma; Yasuo Ebina; Nobuo Iyi; Kazunori Takada, and; Sasaki*, T. General Synthesis and Delamination of Highly Crystalline Transition-Metal-Bearing Layered Double Hydroxides. *Langmuir* **2006**, *23* (2), 861–867. https://doi.org/10.1021/LA062345M.

(96) Jobbágy, M.; Regazzoni, A. E. Delamination and Restacking of Hybrid Layered Double

Hydroxides Assessed by in Situ XRD. *J. Colloid Interface Sci.* **2004**, *275* (1), 345–348. https://doi.org/10.1016/J.JCIS.2004.01.082.

(97) O'leary, S.; O'hare, D.; Seeley, G. Delamination of Layered Double Hydroxides in Polar Monomers: New LDH-Acrylate Nanocomposites. *Chem. Commun.* **2002**, *2* (14), 1506–1507. https://doi.org/10.1039/B204213D.

(98) Chen, W.; Feng, L.; Qu, B. Preparation of Nanocomposites by Exfoliation of ZnAl Layered Double Hydroxides in Nonpolar LLDPE Solution. *Chem. Mater.* **2004**, *16* (3), 368–370. https://doi.org/10.1021/CM0303484.

(99) Hibino, T.; Kobayashi, M. Delamination of Layered Double Hydroxides in Water. *J. Mater. Chem.* **2005**, *15* (6), 653–656. https://doi.org/10.1039/b416913a.

(100) Hibino, T. Delamination of Layered Double Hydroxides Containing Amino Acids. **2004**. https://doi.org/10.1021/cm048842a.

(101) Guo, Y.; Zhang, H.; Zhao, L.; Li, G. D.; Chen, J. S.; Xu, L. Synthesis and Characterization of Cd–Cr and Zn–Cd–Cr Layered Double Hydroxides Intercalated with Dodecyl Sulfate. *J. Solid State Chem.* **2005**, *178* (6), 1830–1836. https://doi.org/10.1016/J.JSSC.2005.03.020.

(102) Li, L.; Ma, R.; Ebina, Y.; Iyi, N.; Sasaki, T. Positively Charged Nanosheets Derived via Total Delamination of Layered Double Hydroxides. *Chem. Mater.* **2005**, *17* (17), 4386–4391. https://doi.org/10.1021/cm0510460.

(103) Kim, H. N.; Keller, S. W.; Mallouk, T. E.; Schmitt, J.; Decher, G. Characterization of Zirconium Phosphate/Polycation Thin Films Grown by Sequential Adsorption Reactions. *Chem. Mater.* **1997**, *9* (6), 1414–1421. https://doi.org/10.1021/CM970027Q.

(104) Ma, R.; Liu, Z.; Li, L.; Iyi, N.; Sasaki, T. Exfoliating Layered Double Hydroxides in Formamide : A Method to Obtain Positively Charged Nanosheets. *J. Mater. Chem.* **2006**, *16* (39), 3809–3813. https://doi.org/10.1039/B605422F.

CHAPTER 2 - Oxide-Free Three-Dimensional Germanium/Silicon Core–Shell Metalattice Made by High-Pressure Confined Chemical Vapor Deposition

(Reprinted from *ACS Nano* 2020, 14, 10, 12810–12818, copyright 2020 American Chemical Society)

2.1 Introduction

Strongly coupled and coherently connected semiconductor nanoparticles offer the possibility of bandlike electron transport in combination with size-dependent electronic and optical properties.[1,2] At the nanoscale, obtaining such delocalized electronic states requires an interconnected network of nanoparticles and a passivated surface. Meta structures with extended electronic states have been realized in nanoparticle/quantum dot superlattices that have a small interparticle distances, which are typically accessed synthetically by ligand stripping and/or exchange.[3−11] These structures can provide enhanced performance in electronic transistors, thermoelectric, optoelectronic light-emitting devices[1,2,12−14] and electrode materials for batteries.[15,16]

Even with ligand modifications, however, it is challenging to integrate particle interconnectivity, periodicity, and quantum confinement into one system. This problem has motivated other synthetic approaches to 3D interconnected periodic structures at the nanoscale, especially the synthesis of mesoporous structures by hard or soft templating methods.[17,18] Recently Liu et al. reported an approach to synthesizing completely connected, atomically crystalline three-dimensional metal structures using high-pressure confined chemical fluid deposition and silica nanoparticle colloidal crystal templates.[19,20] Using the vapor-phase counterpart of this technique, high-pressure confined chemical vapor deposition (HPcCVD), we are now infiltrating semiconductors into the nanoscale voids of the silica template.[21,22,23] These inverse structures, defined as metalattices, inherit the void structure of the template to form an interconnected periodic lattice.

As in other nanoscale structures, the interior surface of a semiconductor metalattice is a significant contributor to its electronic structure and physical properties. In this paper, we explore core–shell synthesis as a way to chemically passivate a Ge metalattice surface. As a group IV semiconductor, Ge has potential applications in electronics. However, despite its high carrier mobility and large exciton Bohr radius relative to Si, its integration into devices has been limited due to its complex surface oxidation chemistry. [24−26]

Depending on the oxidation conditions and the Ge surface exposed (100, 111), Ge forms Ge^{1+}, Ge^{2+}, Ge^{3+}, or Ge^{4+} or even a mixture of different oxides. [27−30] These native oxide layers on Ge are not stable and do not form a defect-free interface. Passivation techniques developed so far for Ge nanostructures such as thin films, wafers, and wires can be broadly classified into two kinds of techniques. The first are methods that terminate the surface with a Ge–M covalent bond, where M can be hydrogen, a halogen (Cl, Br, I), or an alkyl group, [31−38] and the second involves a core–shell approach that passivates the surface by forming a shell around the Ge core. [39−43] Surface modification inside a metalattice is more challenging in comparison to wires, films and nanocrystals due to the interconnected structure, high curvature, and high surface area to volume ratio. This added complexity makes it difficult to extend covalent passivation methods to metalattices. Most of the covalent passivation methods involve intermediate steps that etch the sample or high temperature annealing, which could result in metalattice collapse, delamination from the supporting substrate, or a rough passivated surface. The core–shell approach, which has been employed in Ge heterostructures, nanowires and nanoparticles, provides a conformal coating for passivation. In addition to passivation, the core–shell structures also enable band gap engineering, modulation doping, and multifunctionality.

The core–shell approach has been implemented in semiconductor nanocrystals via both solution and gas phase deposition methods. [3,43−46] In 2017, Hunter et al. [43] reported the

synthesis of Ge nanocrystals with Si shells using a nonthermal plasma method, which enabled more control of the core and shell dimensions in comparison to solution processes. Because of the versatility of the core–shell approach with structures and surfaces and its ability to integrate with the HPcCVD technique, we have applied it here to metalattices. In this paper, we demonstrate the chemical passivation of Ge metalattices by forming a Si shell and study the effect of the Si shell on the oxidation state/chemical composition of the Ge core. While the use of Si shells for Ge passivation is well established for 2D and 1D nanostructures, we present here the chemical passivation of a 3D interconnected Ge nanostructure using a Si shell.

Core–shell metalattices were synthesized by sequential infiltration of Ge and Si into silica templates using HPcCVD (see Figure 2.1), which provides access to the nanoscale voids in the template [47] and also creates a uniform and conformal shell on the Ge core. The effect of chemical passivation/modification of Ge nanocrystals/films on their electronic structure has been commonly probed by absorption or photoluminescence (PL) spectroscopy. In the absence of bulk defects and unpassivated surface states, quantum confinement effects in nanoscale Ge can be characterized by mapping the shifts in absorption edge or PL peak positions as has been reported in several earlier studies. [18,48−51] Core–shell metalattices did not show sharp emission features that could be attributed to Ge nanocrystals of specific sizes. Instead, broad photoluminescence was observed above the band gap energy (Figure A4), possibly due to the presence of Ge nanocrystals that have many different degrees of quantum confinement. Therefore, to probe the electronic structure at the local level in the metalattice we accessed the Ge 3d edge using electron energy loss spectroscopy (EELS) in the transmission electron microscope. This technique has been used before to probe electronic structure and bonding in a number of materials at nanometer resolution. [52] In our system, EELS coupled

with Raman spectroscopy to characterize the interdiffusion of Ge and Si atoms at the core–shell interface, provides information about the electronic effects of dimensional confinement and core–shell interdiffusion in the Ge metalattice.

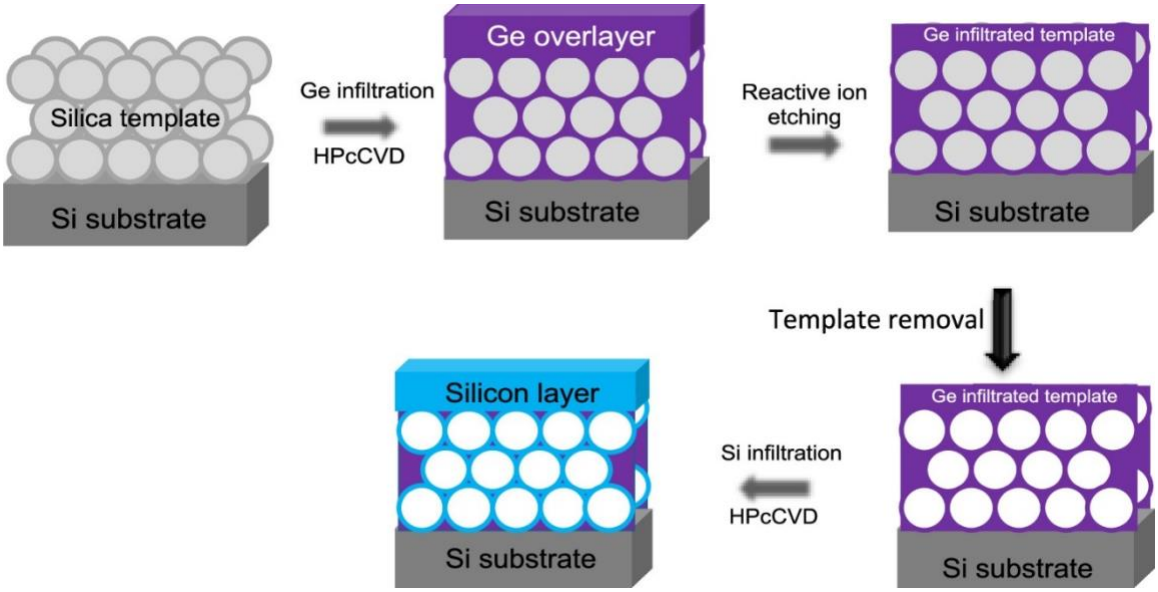

Figure 2.1. Schematic diagram of the steps involved in core–shell metalattice synthesis.

2.2 Experimental methods

2.2.1 Silica Nanoparticle Template Synthesis

Monodisperse spherical silica nanoparticles (diameter 69.2 ± 3.2 nm, Figure A1) were synthesized using the method of Watanabe et al. [67] A colloidal solution of as-synthesized silica nanoparticles was diluted 10× for deposition. Double-side polished undoped silicon wafers (University Wafers) of ~280 μm thickness and ⟨100⟩ orientation were cut into 3 cm × 1 cm pieces. Before deposition, the silicon wafer pieces were treated with freshly prepared piranha solution (3:1 concentrated H2SO4: 30% v/v H2O2) for 15–20 min. (Caution: Piranha solution is corrosive to skin and can react explosively with organic substances.) The wafers were then copiously rinsed with water followed by ethanol and

were dried in a stream of air. The diluted nanoparticle suspension was deposited on the Si wafers in open plastic vials at controlled temperature and humidity (40 °C at 80% RH) as described earlier by Russell et al.[68] Then 8 mm × 5 mm pieces were diced from the films obtained at the end of 2 weeks for metalattice infiltration. The thickness of these nanoparticle films, as measured by SEM, varied from 240 to 850 nm depending on the vertical position on the substrate. A representative SEM image of the silica nanoparticle template is shown in Figure A1.

2.2.2 Core–Shell Metalattice Synthesis

The synthesis of a core–shell metalattice is a three-step process involving infiltration of Ge into the interstitial voids of the template followed by template etching and finally infiltration with Si to form the shell. HPcCVD was used for both Ge and Si infiltration steps. In the HPcCVD process, high pressure ensures that the mean free path of precursor molecules is on the order of a few nanometers, enabling them to penetrate the nanoscale voids of the silica template prior to decomposition on the walls. Spatial confinement of the precursor molecules results in the formation of a smooth film because it inhibits vapor-phase homogeneous nucleation of Ge or Si. The process for synthesizing the core–shell metalattice is described briefly below.

Germane (GeH_4) at a partial pressure of 5–10% in helium carrier gas at a total pressure of 20–35 MPa was used as the Ge precursor. Spatial confinement was ensured by placing U-shaped stainless-steel spacers of 25 μm thickness between adjacent template pieces in the HPcCVD reactor. Amorphous germanium was deposited at a temperature of 325 °C for 1–3 h depending on the gas pressure and concentration. After the interstitial voids were completely filled by germanium, the germanium overlayer on top of the metalattice was removed by deep reactive ion etching (DRIE) in a chlorine plasma. The metalattice

was then treated with 3% hydrofluoric (HF) acid solution in water for 4 min to etch away the silica nanospheres. (Caution: HF is highly reactive, hazardous, and corrosive.) The metalattice was then rinsed with deionized water and dried using acetone. Immediately following this etching step (within 20 min), a silicon shell was deposited in the germanium metalattice at 400 °C using HPcCVD with silane (SiH_4) as the precursor in helium carrier gas. Silicon deposition was carried out for 30–60 min, depending on the gas pressure and concentration, to form a thin shell around Ge. The germanium core was crystallized afterward using rapid thermal annealing (RTA) at 550 °C for 120 s to promote rapid crystallization without fusion of the metalattice or significant oxygen contamination by diffusion into the structure. Figure A2 shows a Ge metalattice obtained after infiltration and etching of silica template.

2.2.3 Characterization

2.2.3.1 Scanning Electron Microscopy

Silica nanoparticles and the templates were imaged and sized by using a Zeiss SIGMA VP-FESEM and ImageJ software, respectively.

2.2.3.2 X-ray Diffraction

XRD on core–shell metalattice films and a Si reference sample was performed on a Malvern Panalytical Xpert Pro MPD, and the analysis was performed using Jade and Origin software.

2.2.3.3 TEM and EELS

A FEI Helios Nanolab 660 FIB/FESEM was used for TEM sample preparation. STEM images and EDS maps were collected using a Talos F200X scanning/transmission

electron microscope equipped with a XEDS detector at 200 kV accelerating voltage. A double aberration corrected Titan Transmission Electron Microscope with Gatan GIF and a monochromator was used for STEM-EELS. The accelerating voltage was 80 kV with a spot size of 14 nm and an energy resolution of ~0.14 eV. A C3 aperture of 50 μm and C2 aperture of 150 μm were used for data acquisition with a dwell time for 10 ms for each spectrum. EELS analysis was performed in Digital Micrograph and OriginPro. The background from the plasmon peak at ~16 eV was subtracted to obtain the Ge 3d edge onset on a flat baseline. A constrained power law equation, 69 $y(x) = a((x + m)^{(-r)}) + b$, where a, b, r, and m are fitting parameters, was used to fit the background, and the background-corrected spectra were compared (Figure A6). The inflection point was chosen as the edge onset.

2.2.3.4 Raman Spectroscopy

Raman spectra were collected using an ND-MDT confocal Raman (Renishaw) spectrometer. An excitation wavelength of 532 nm was used at 1 mW with a 100× objective, and the signal was collected by using a Peltier-cooled Andor CCD detector. The exposure time was limited to 20 s to prevent damage to the sample. The spectra were collected at multiple spots to confirm the uniformity of the sample.

2.2.3.5 X-ray Photoelectron Spectroscopy

XPS experiments were performed using a Physical Electronics Versa Probe II instrument equipped with a monochromatic Al Kα X-ray source (hv = 1,486.7 eV) and a concentric hemispherical analyzer. Measurements were made at a takeoff angle of 45° with respect to the sample surface plane. This resulted in a typical sampling depth of 3–6 nm (95% of the signal originated from this depth or shallower). The sample was ion milled (20 nm) in situ to obtain a freshly cleaned surface for compositional analysis. The Si 2p and Ge 3d

spectra were curve fitted into metallic and oxidized forms using CasaXPS software (version 2.3.19rev1.0k). The Si 2p spectra were fitted with 3/2 and 1/2 spin orbit doublets with peaks constrained for identical full-width-at-half-maximum (fwhm), peak area (2:1) and an offset of +0.607 eV. The Ge 3d spectra were also fitted with matching fwhm, a 3d 5/2 to 3/2 peak area ratio of 3:2 and offsets of +0.59 eV.

2.2.3.6 Photoluminescence Spectroscopy

Measurements were made inside a cryostat (Janis Research ST-300R) using a continuous liquid nitrogen flow and illumination with a 785 nm laser diode (Coherent OBIS) operated at 50 mW with a spot size of ~2 mm diameter. The Ge film sample was illuminated by 640 nm diode laser operated at 100 mW. The emitted light was collected from a ~400 um diameter spot through a long pass filter (900 nm) and measured in a spectrometer (Horiba iHR320) with an InGaAs array (Horiba Symphony). Data are proportional to the photon flux by calibration through the same optical setup with a calibrated light source (Ocean Optics LS-1-cal).

2.2.3.7 Small Angle X-ray Scattering

Synchrotron SAXS measurements were performed at beamline 12-ID-B at the Advanced Photon Source, Argonne National Laboratory. An X-ray beam with energy of 14 keV and a spot size of 200 × 100 μm2 was used, with 1s exposure time. The 2D pattern was collected in transmission mode on Pilatus 2 M detector.

2.3 Results and Discussion

The synthesis of a core–shell metalattice is a multistep process as discussed in the Experimental Methods and illustrated in Figure 2.1. The silica sphere template is etched away using aqueous HF between the sequential deposition of Ge and Si. This step serves

the dual purpose of template removal and termination of the Ge surface with Ge–H bonds. Even though the hydride-terminated Ge surface is stable for only a short time (maximum a few hours), [53] it protects the surface from oxidation prior to shell formation. Both Ge and Si are infiltrated in their amorphous forms by HPcCVD. The Ge core is annealed after the Si shell is added to ensure formation of a conformal coating. Because Ge crystallizes at a lower temperature than Si, we could selectively crystallize only the Ge core by rapid thermal annealing. TEM EDS shown in Figure 2.2 confirms the formation of the core–shell metalattice, and high-resolution TEM shows the amorphous Si shell and polycrystalline Ge core. X-ray diffraction (XRD) of the core–shell metalattice film also confirms the crystallinity of the Ge core (Figure A3). We observed that the width of the Ge (111) peak is approximately twice the instrumental line width, obtained from a corresponding peak of a crystalline Si standard as shown in Figure A3. The broadening and asymmetry of the Ge peak are a function of nanocrystallite size and Si–Ge lattice mismatch-induced strain in the structure. According to the Scherrer formula (see Appendix A), the width of the Ge (111) reflection corresponds to a crystalline domain size of ~47 nm, which is about twice the size of the largest voids in the 69 nm silica sphere template (~29 nm) and much larger than the diameter of the necks between voids, which is ~11 nm. This indicates that the crystalline domains extend beyond a single meta-atom. In addition, there is significant strain in the Ge lattice, as evidenced by the shift and asymmetry of the Ge–Ge Raman peak (Figure 2.3), and this effect contributes to the X-ray line broadening. Thus, the relatively narrow peak width of the Ge (111) reflection implies crystalline domains that extend across at least several interconnected meta-atoms in the core–shell structure.

In addition to TEM, we used Raman spectroscopy to gain insight into the structural composition of the core–shell structure. Figure 2.3 shows a comparison of a Ge–Si core–

shell metalattice with the corresponding Ge metalattice and a CVD grown Ge film. We observe a first-order optical phonon mode for Ge–Ge at ~300 cm^{-1} for all three Ge structures—thin film, metalattice, and core–shell—indicating successful infiltration of Ge (Table A1). In addition to the Ge–Ge mode, optical phonon modes for Ge–Si and Si–Si are also present in the core–shell metalattice. The shapes of the peaks (sharp *vs* broad) confirm the presence of polycrystalline Ge and an amorphous Si shell, in agreement with the TEM images.

Following initial structural characterization of the core-shell metalattice, we investigated the possible presence of Ge oxide in the structure using XPS as shown in Figure 2.4. Oxidation of the exposed metalattice surface containing both Ge and Si was expected as

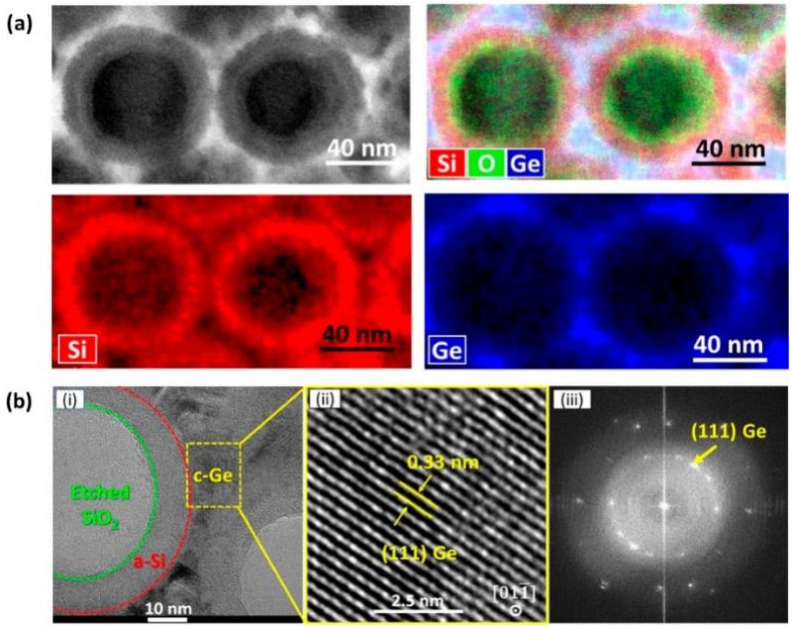

Figure 2.2 (a) TEM image with energy-dispersive X-ray spectroscopy (EDS) maps of the Ge–Si core–shell structure showing formation of the interconnected Ge structure within a Si shell. (b) High-resolution TEM image showing (i) the crystalline Ge core, amorphous Si shell, and etched silica sphere regions;(ii) magnified region from the Ge core showing Ge lattice fringes; (iii) fast Fourier transform (FFT) of the Ge core region.

the sample was not stored in an inert atmosphere. However, after *in-situ* ion milling of the top layer (20 nm), no Ge oxide signal was detected. We do not observe any Ge oxide in the structure within the detection limit of XPS. Si, on the other hand, shows the presence of an oxide after ion milling.

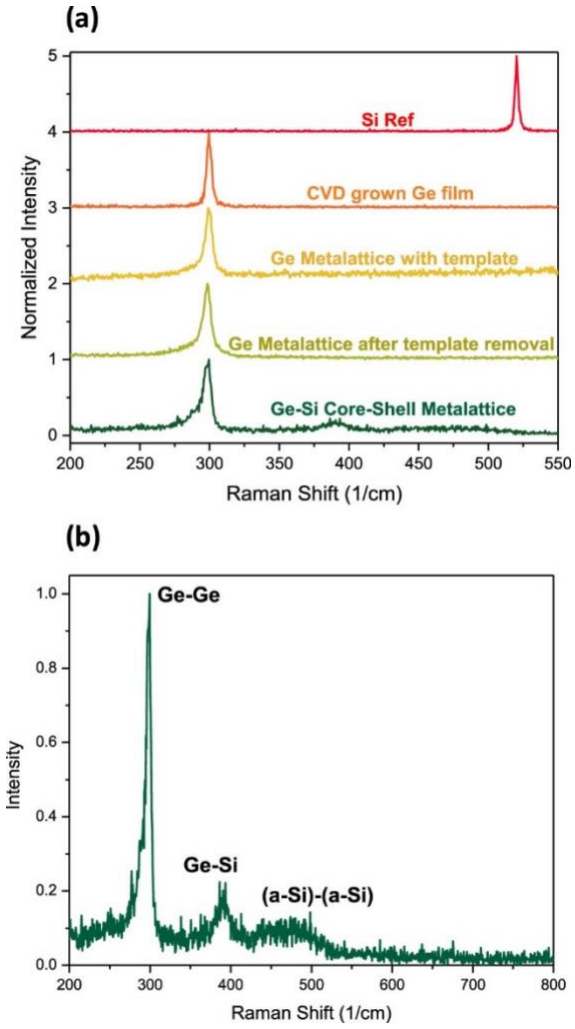

Figure 2.3 (a) Raman spectrum at different steps of the sample preparation. The sharp Ge–Ge peak at ~300 cm^{-1} indicates the presence of crystalline Ge in the metalattice. (b) Raman spectrum of the core–shell metalattice. The appearance of a Ge–Si band at ~390 cm^{-1} indicates possible interdiffusion of Si and Ge.

This can be attributed to the oxidation of the protective Si shell, which upon exposure to air forms a native oxide layer and passivates the material against further oxidation of metalattice. Another source of silicon oxide could be from the silica nanoparticles. We have observed partial etching in these samples in some regions using both SEM and TEM. This means the residual SiO_2 particles could also be contributing to the oxide in the XPS spectrum.

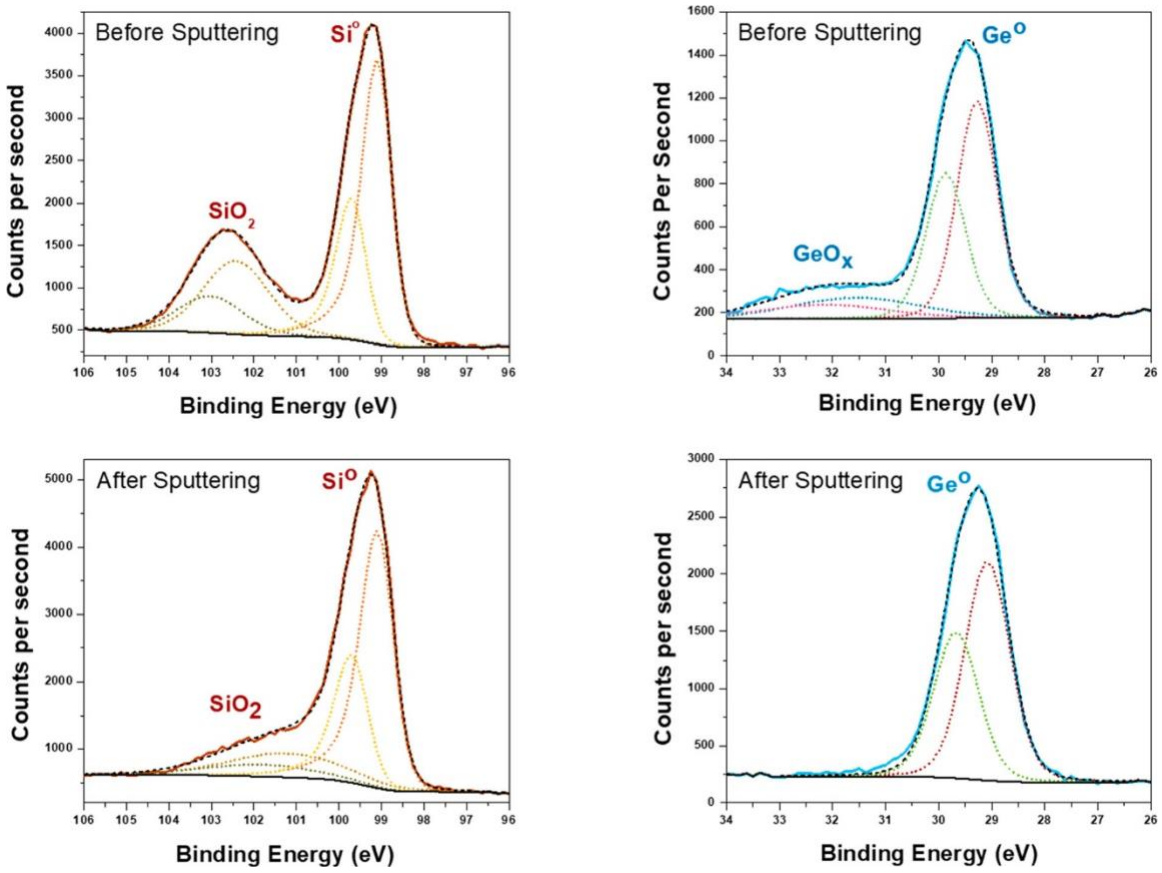

Figure 2.4. High-resolution Ge 3d and Si 2p X-ray photoelectron spectra of core–shell metalattice before and after in situ ion milling top 20 nm film. The dotted lines represent fitting for respective peaks.

As noted above, one of the major challenges in implementing Ge in electronic devices or in even studying the fundamental properties of Ge nanostructures is the oxidation and reconstruction of the Ge surface, which leads to defect formation. The preparation of an

oxide-free Ge metalattice allows us to investigate the effect of structural confinement and the Si shell on the local electronic properties of the Ge metalattice. Since the measured PL spectrum was broad (Figure A4), possibly due to different degrees of confinement at different sites within the macroscopic collection area, we used EELS to study the structure at microscopic level. With the energy and spatial resolution of EELS in the electron microscope, it is possible to obtain the Ge 3d edge energies locally at different sites in the metalattice.

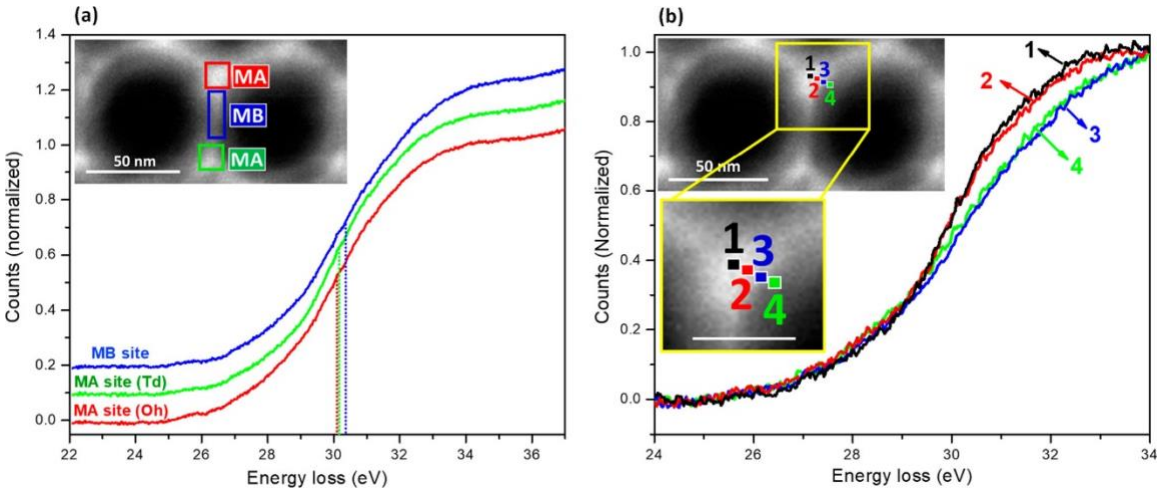

Figure 2.5. Normalized EELS spectra of the Ge 3d core-edge at (a) different sites in the metalattice structure. The spectra are stacked to highlight the shift in the inflection point (inset shows representative MA and MB sites) and (b) different points in the core/shell structure (inset shows representative core, interface, and shell points with a magnified view of the points). Scale bar in the magnified image is 25 nm.

The Ge metalattice conforms to the void structure of the silica nanoparticle template as shown in Figure A2 and maintains the long-range order of the template as observed in the small-angle X-ray scattering (SAXS) pattern (Figure A5). The Ge replica of the close-packed silica sphere lattice can be conceptually divided into meta-atoms and meta-bonds (MA and MB), where the meta-atoms are formed in the tetrahedral/octahedral voids of the

silica nanoparticle template and the meta-bonds correspond to the thin connections between these voids. We were able to selectively probe the Ge 3d edge at MA and MB sites as shown in Figure 2.5a.

A small shift of ~0.2 eV in the 3d edge onset between the MA and MB regions was observed (Table A2). This shift in the edge onset should be interpreted cautiously due to the several contributing parameters that include structural confinement, defects, and strain. Earlier studies by Hanrath *et al.* [54] and Batson *et al.* [55] on Ge nanowires and Si clusters, respectively, have found a size-dependent variation in the edge onset mapped by EELS, which is characteristic of the quantum confinement that has been seen in other studies of Ge quantum dots and nanowires. [18,48–51,56] At the microscopic level, we also expect to see a variation in the degree of confinement of Ge in the metalattice due to the different sizes of the voids in the template from which it is formed. In a template composed of 69 nm diameter silica spheres, the void sizes range from 11 to 29 nm, providing different degrees of confinement for crystalline Ge, which has an exciton Bohr radius of 24 nm. [51] This structural confinement by the template affects the average size of the Ge crystalline domains in the MA and MB sites and thus can contribute to the variation in the edge energy. The shift toward higher energy with decreasing void size is consistent with quantum confinement. The two types of voids labeled as MA sites in Figure 2.5a cannot be distinguished in the 2D image, but we speculate the trend on the basis of void size. However, structural confinement may not be the only factor determining the size of the Ge crystalline domains. Several other factors including the rate and type of nucleation and growth could also affect their size and thus the edge onset. We observe a comparable shift in the same types of sites across several samples, possibly due to variation in the average size of the crystalline domains as influenced by these other factors.

Even though structural confinement could be a significant contributor to the blue shift in edge onset, other factors in a polycrystalline core–shell system such as grain boundaries and interfacial strain may also contribute. We accessed the Ge 3d edge at different positions from core to shell to understand the local effects of the Si shell and its interaction with the Ge core. Figure 2.5b shows an average spectrum representing each of these sites. The Ge edge at sites 1 and 2 does not show any shift in onset energy indicating no change in the oxidation state or bonding of Ge in the core. However, as we progress into the shell, there is a shift of ~0.2–0.3 eV in the edge onset (Table A3). We speculate that a change in the chemical environment of Ge and strain at the interface can lead to these shifts. Earlier studies of core–shell Ge–Si nanocrystals have also noted a blue shift in the absorption edge onset due to strain. [43] Ge and Si have a lattice mismatch of ~4%, [40] and it has been shown that lattice mismatch-induced strain is often compensated by interdiffusion of Ge and Si. [40,57−60] The shift in the Ge 3d edge in close proximity to the shell and the presence of a Ge–Si vibrational mode in the Raman spectrum indicate the possibility of interdiffusion leading to a change in the bonding environment of Ge. Since the shift in the Ge 3d edge occurs at sites close to or in the shell, we believe that the Ge–Si region is localized at the interface/shell and not in the Ge core.

From the trends in the EELS data, we identify two parameters that can be used to tune the electronic properties of the Ge–Si core–shell metalattice. The first parameter is the size of the voids in the template, which are defined by the size of the silica spheres used. The void size controls the degree of confinement of Ge and hence the band gap and distribution (discreteness) of electronic states. With a large exciton Bohr radius (24 nm), it is possible to confine Ge using the silica templating method. The shell and core interaction serve as a second parameter. The shell thickness and controlled interdiffusion of Ge and

Si have been used previously in nanostructures to modify the strain and alloy composition at the interface, providing control of the band offset, band gap and charge carrier distribution in the material. [39,40,43,58,61–66] The confinement of both electrons and holes in an oxide free Ge nanostructure can be realized in a core–shell metalattice and in principle can be tuned to affect the charge carrier mobility.

2.4 Conclusions

Crystalline semiconductor metalattices have been synthesized by combining HPcCVD and silica nanoparticle assembly. In this study, we have demonstrated a core–shell approach for chemical passivation and obtain an oxide-free Ge metalattice. A uniform Si shell infiltrated using HPcCVD around the Ge core prevents oxide formation as confirmed by XPS. Further structural characterization performed using TEM, Raman, and XRD confirms the formation of a core–shell structure with an amorphous Si shell and a polycrystalline Ge core. Microscopic details of structural confinement and the effect of the Si shell on the Ge core were explored locally using EELS. We observe a blue shift in the Ge 3d edge with decreasing void size, indicating the possibility of quantum confinement in the metalattices, which arises from the structure of the template. Mapping of the 3d edge along the core–shell interface indicates a chemically uniform core and possible interdiffusion of Ge and Si, as also evidenced in Raman spectra as the formation of Ge–Si bonds near the shell. The HPcCVD method enables the formation of a uniform Si shell on the Ge core, which protects it from oxidation. EELS data from the core–shell structure suggest that the degree of quantum confinement can be controlled by adjusting the size of the template spheres and the interdiffusion of Ge and Si at the core–shell interface in order to tune the band gap and charge carrier distributions. In addition, the core–shell

approach demonstrated here can, in principle, be extended to different semiconductor material systems as core and shell for controlled tuning of electronic structure.

2.5 References

(1) Kagan, C. R.; Murray, C. B. Charge Transport in Strongly Coupled Quantum Dot Solids. Nat. Nanotechnol. 2015, 10, 1013− 1026.

(2) Vanmaekelbergh, D.; Liljeroth, P. Electron-Conducting Quantum Dot Solids: Novel Materials Based on Colloidal Semiconductor Nanocrystals. Chem. Soc. Rev. 2005, 34, 299−312.

(3) Talapin, D. V.; Lee, J. S.; Kovalenko, M. V.; Shevchenko, E. V. Prospects of Colloidal Nanocrystals for Electronic and Optoelectronic Applications. Chem. Rev. 2010, 110, 389−458.

(4) Brown, P. R.; Kim, D.; Lunt, R. R.; Zhao, N.; Bawendi, M. G.; Grossman, J. C.; Bulovic, V. Energy Level Modification in Lead´ Sulfide Quantum Dot Thin Films through Ligand Exchange. ACS Nano 2014, 8, 5863−5872.

(5) Kovalenko, M. V.; Scheele, M.; Talapin, D. V. Colloidal Nanocrystals with Molecular Metal Chalcogenide Surface Ligands. Science 2009, 324, 1417−1420.

(6) Nag, A.; Kovalenko, M. V.; Lee, J. S.; Liu, W.; Spokoyny, B.; Talapin, D. V. Metal-Free Inorganic Ligands for Colloidal Nanocrystals: S2-, HS-, Se2-, HSe-, Te2-, HTe-, TeS32-, OH-, and NH 2- as Surface Ligands. J. Am. Chem. Soc. 2011, 133, 10612−10620.

(7) Fafarman, A. T.; Koh, W. K.; Diroll, B. T.; Kim, D. K.; Ko, D. K.; Oh, S. J.; Ye, X.; Doan-Nguyen, V.; Crump, M. R.; Reifsnyder, D. C.; Murray, C. B.; Kagan, C. R. Thiocyanate-Capped Nanocrystal Colloids: Vibrational Reporter of Surface Chemistry and SolutionBased Route to Enhanced Coupling in Nanocrystal Solids. J. Am. Chem. Soc. 2011, 133, 15753−15761.

(8) Baumgardner, W. J.; Whitham, K.; Hanrath, T. Confined-ButConnected Quantum Solids via Controlled Ligand Displacement. Nano Lett. 2013, 13, 3225−3231.

(9) Zhang, H.; Hu, B.; Sun, L.; Hovden, R.; Wise, F. W.; Muller, D. A.; Robinson, R. D. Surfactant Ligand Removal and Rational Fabrication of Inorganically Connected Quantum Dots. Nano Lett. 2011, 11, 5356−5361.

(10) Boles, M. A.; Ling, D.; Hyeon, T.; Talapin, D. V. The Surface Science of Nanocrystals. Nat. Mater. 2016, 15, 141−153.

(11) Wheeler, L. M.; Nichols, A. W.; Chernomordik, B. D.; Anderson, N. C.; Beard, M. C.; Neale, N. R. All-Inorganic Germanium Nanocrystal Films by Cationic Ligand Exchange. Nano Lett. 2016, 16, 1949−1954.

(12) Talgorn, E.; Gao, Y.; Aerts, M.; Kunneman, L. T.; Schins, J. M.; Savenije, T. J.; Van Huis, M. A.; Van Der Zant, H. S. J.; Houtepen, A. J.; Siebbeles, L. D. A. Unity Quantum Yield of Photogenerated Charges and Band-Like Transport in Quantum-Dot Solids. Nat. Nanotechnol. 2011, 6, 733−739.

(13) Lee, J. S.; Kovalenko, M. V.; Huang, J.; Chung, D. S.; Talapin, D. V. Band-Like Transport, High Electron Mobility and High Photoconductivity in All-Inorganic Nanocrystal Arrays. Nat. Nanotechnol. 2011, 6, 348−352.

(14) Choi, J. H.; Fafarman, A. T.; Oh, S. J.; Ko, D. K.; Kim, D. K.; Diroll, B. T.; Muramoto, S.; Gillen, J. G.; Murray, C. B.; Kagan, C. R. Bandlike Transport in Strongly Coupled and Doped Quantum Dot Solids: A Route to High-Performance Thin-Film Electronics. Nano Lett. 2012, 12, 2631−2638.

(15) Li, X.; Yang, Z.; Fu, Y.; Qiao, L.; Li, D.; Yue, H.; He, D. Germanium Anode with Excellent Lithium Storage Performance in a Germanium/Lithium-Cobalt Oxide Lithium-Ion Battery. ACS Nano 2015, 9, 1858−1867.

(16) Zhou, L.; Zhang, K.; Hu, Z.; Tao, Z.; Mai, L.; Kang, Y.-M.; Chou, S.-L.; Chen, J. Recent Developments on and Prospects for Electrode Materials with Hierarchical Structures for Lithium-Ion Batteries. Adv. Energy Mater. 2018, 8, 1701415.

(17) Armatas, G. S.; Kanatzidis, M. G. Hexagonal Mesoporous Germanium. Science 2006, 313, 817−820. (18) Armatas, G. S.; Kanatzidis, M. G. Size Dependence in Hexagonal Mesoporous Germanium: Pore Wall Thickness versus Energy Gap and Photoluminescence. Nano Lett. 2010, 10, 3330− 3336.

(18) Armatas, G. S.; Kanatzidis, M. G. Size Dependence in Hexagonal Mesoporous Germanium: Pore Wall Thickness versus Energy Gap and Photoluminescence. Nano Lett. 2010, 10, 3330− 3336.

(19) Liu, Y.; Kempinger, S.; He, R.; Day, T. D.; Moradifar, P.; Yu, S. Y.; Russell, J. L.; Torres, V. M.; Xu, P.; Mallouk, T. E.; Mohney, S. E.; Alem, N.; Samarth, N.; Badding, J. V. Confined Chemical Fluid Deposition of Ferromagnetic Metalattices. Nano Lett. 2018, 18, 546− 552.

(20) Chen, Y.; Liu, Y.; Moradifar, P.; Glaid, A. J.; Russell, J. L.; Mahale, P.; Yu, S.-Y.; Culp, T. E.; Kumar, M.; Gomez, E. D.; Mohney, S. E.; Mallouk, T. E.; Alem, N.; Badding, J. V.; Liu, Y. Quantum Transport in Three-Dimensional Metalattices of Platinum Featuring an Unprecedentedly Large Surface Area to Volume Ratio. Phys. Rev. Mater. 2020, 4, 035201.

(21) Chen, W.; Talreja, D.; Eichfeld, D.; Mahale, P.; Nova, N. N.; Cheng, H. Y.; Russell, J. L.; Yu, S.-Y.; Poilvert, N.; Mahan, G.; Mohney, S. E.; Crespi, V. H.; Mallouk, T. E.; Badding, J. V.; Foley, B.; Gopalan, V.; Dabo, I. Achieving Minimal Heat Conductivity by Ballistic Confinement in Phononic Metalattices. ACS Nano 2020, 14, 4235−4243.

(22) Abad, B.; Knobloch, J. L.; Frazer, T. D.; Hernandez-Charpak, J. N.; Cheng, H. Y.; Grede, A. J.; Giebink, N. C.; Mallouk, T. E.; Mahale, P.; Nova, N. N.; Tomaschke, A. A.; Ferguson, V. L.; Crespi, V. H.; Gopalan, V.; Kapteyn, H. C.; Badding, J. V.; Murnane, M. M. Nondestructive Measurements of the Mechanical and Structural Properties of Nanostructured Metalattices. Nano Lett. 2020, 20, 3306−3312.

(23) Yu, S.-Y.; Cheng, H. Y.; Dysart, J. L.; Huang, Z.; Wang, K.; Mallouk, T. E.; Crespi, V. H.; Badding, J. V.; Mohney, S. E. Scanning Transmission Electron Tomography and Electron Energy Loss Spectroscopy of Silicon Metalattices. 2020, arXiv:2009.01111. arXiv.org e-Print active. https://arxiv.org/abs/2009.01111.

(24) Collins, G.; Holmes, J. D. Chemical Functionalisation of Silicon and Germanium Nanowires. J. Mater. Chem. 2011, 21, 11052−11069.

(25) Loscutoff, P. W.; Bent, S. F. Reactivity of the germanium surface: Chemical Passivation and Functionalization. Annu. Rev. Phys. Chem. 2006, 57, 467−495.

(26) Buriak, J. M. Organometallic Chemistry on Silicon and Germanium Surfaces. Chem. Rev. 2002, 102, 1271−1308.

(27) Schmeisser, D.; Schnell, R. D.; Bogen, A.; Himpsel, F. J.; Rieger, D.; Landgren, G.; Morar, J. F. Surface Oxidation States of Germanium. Surf. Sci. 1986, 172, 455−465.

(28) Sasada, T.; Nakakita, Y.; Takenaka, M.; Takagi, S. Surface Orientation Dependence of Interface Properties of GeO2/Ge MetalOxide-Semiconductor Structures Fabricated by Thermal Oxidation. J. Appl. Phys. 2009, 106, 073716.

(29) Prabhakaran, K.; Ogino, T. Oxidation of Ge(100) and Ge(111) Surfaces: An UPS and XPS Study. Surf. Sci. 1995, 325, 263−271.

(30) Yang, M.; Wu, R. Q.; Chen, Q.; Deng, W. S.; Feng, Y. P.; Chai, J. W.; Pan, J. S.; Wang, S. J. Impact of Oxide Defects on Band Offset at GeO2/Ge Interface. Appl. Phys. Lett. 2009, 94, 142903.

(31) Amy, S. R.; Chabal, Y. J. Passivation and Characterization of Germanium Surfaces. In Advanced Gate Stacks for High-Mobility Semiconductors; Springer: Berlin, 2007; Vol. 27, pp 73−113.

(32) Hanrath, T.; Korgel, B. A. Chemical Surface Passivation of Ge Nanowires. J. Am. Chem. Soc. 2004, 126, 15466−15472.

(33) Choi, K.; Buriak, J. M. Hydrogermylation of Alkenes and Alkynes on Hydride-Terminated Ge(100) Surfaces. Langmuir 2000, 16, 7737−7741.

(34) Muthuswamy, E.; Zhao, J.; Tabatabaei, K.; Amador, M. M.; Holmes, M. A.; Osterloh, F. E.; Kauzlarich, S. M. Thiol-Capped Germanium Nanocrystals: Preparation and Evidence for Quantum Size Effects. Chem. Mater. 2014, 26, 2138−2146.

(35) Taylor, B. R.; Fox, G. A.; Hope-Weeks, L. J.; Maxwell, R. S.; Kauzlarich, S. M.; Lee, H. W. H. Solution Preparation of Ge Nanoparticles with Chemically Tailored Surfaces. Mater. Sci. Eng., B 2002, 96, 90−93.

(36) Ma, X.; Wu, F.; Kauzlarich, S. M. Alkyl-Terminated Crystalline Ge Nanoparticles Prepared from NaGe: Synthesis, Functionalization and Optical Properties. J. Solid State Chem. 2008, 181, 1628−1633.

(37) Purkait, T. K.; Swarnakar, A. K.; De Los Reyes, G. B.; Hegmann, F. A.; Rivard, E.; Veinot, J. G. C. One-Pot Synthesis of ACS Nano www.acsnano.org Article https://dx.doi.org/10.1021/acsnano.0c03559 ACS Nano 2020, 14, 12810−12818 12817 Functionalized Germanium Nanocrystals from a Single Source Precursor. Nanoscale 2015, 7, 2241−2244.

(38) Fok, E.; Shih, M.; Meldrum, A.; Veinot, J. G. C. Preparation of Alkyl-Surface Functionalized Germanium Quantum Dots via Thermally Initiated Hydrogermylation. Chem. Commun. 2004, 10, 386− 387.

(39) Kuo, Y. H.; Lee, Y. K.; Ge, Y.; Ren, S.; Roth, J. E.; Kamins, T. I.; Miller, D. A. B.; Harris, J. S. Strong Quantum-Confined Stark Effect in Germanium Quantum-Well Structures on Silicon. Nature 2005, 437, 1334−1336.

(40) Hu, S.; Kawamura, Y.; Huang, K. C. Y.; Li, Y.; Marshall, A. F.; Itoh, K. M.; Brongersma, M. L.; McIntyre, P. C. Thermal Stability and Surface Passivation of Ge Nanowires Coated by Epitaxial SiGe Shells. Nano Lett. 2012, 12, 1385−1391.

(41) Lu, W.; Xiang, J.; Timko, B. P.; Wu, Y.; Lieber, C. M. OneDimensional Hole Gas in Germanium/Silicon Nanowire Heterostructures. Proc. Natl. Acad. Sci. U. S. A. 2005, 102, 10046−10051.

(42) Nestoklon, M. O.; Poddubny, A. N.; Voisin, P.; Dohnalova, K. Tuning Optical Properties of Ge Nanocrystals by Si Shell. J. Phys. Chem. C 2016, 120, 18901−18908.

(43) Hunter, K. I.; Held, J. T.; Mkhoyan, K. A.; Kortshagen, U. R. Nonthermal Plasma Synthesis of Core/Shell Quantum Dots: Strained Ge/Si Nanocrystals. ACS Appl. Mater. Interfaces 2017, 9, 8263−8270.

(44) Dabbousi, B. O.; Rodriguez-Viejo, J.; Mikulec, F. V.; Heine, J. R.; Mattoussi, H.; Ober, R.; Jensen, K. F.; Bawendi, M. G. (CdSe)ZnS Core-Shell Quantum Dots: Synthesis and Characterization of a Size Series of Highly Luminescent Nanocrystallites. J. Phys. Chem. B 1997, 101, 9463−9475.

(45) Littau, K. A.; Szajowski, P. J.; Muller, A. J.; Kortan, A. R.; Brus, L. E. A Luminescent Silicon Nanocrystal Colloid via a HighTemperature Aerosol Reaction. J. Phys. Chem. 1993, 97, 1224−1230.

(46) Yang, C. S.; Kauzlarich, S. M.; Wang, Y. C. Synthesis and Characterization of Germanium/Si-Alkyl and Germanium/Silica Core-Shell Quantum Dots. Chem. Mater. 1999, 11, 3666−3670.

(47) Sparks, J. R.; Baril, N. F.; Keshavarzi, B.; Krishnamurthi, M.; Temnykh, I.; Sazio, P. J. A.; Peacock, A. C.; Borhan, A.; Gopalan, V.; Badding, J. V. High-Pressure Chemical Deposition for Void-Free Filling of Extreme Aspect Ratio Templates. Adv. Mater. 2010, 22, 4605−4611.

(48) Ruddy, D. A.; Johnson, J. C.; Smith, E. R.; Neale, N. R. Size and Bandgap Control in the Solution-Phase Synthesis of Near-InfraredEmitting Germanium Nanocrystals. ACS Nano 2010, 4, 7459−7466.

(49) Lee, D. C.; Pietryga, J. M.; Robel, I.; Werder, D. J.; Schaller, R. D.; Klimov, V. I. Colloidal Synthesis of Infrared-Emitting Germanium Nanocrystals. J. Am. Chem. Soc. 2009, 131, 3436−3437.

(50) Takeoka, S.; Fujii, M.; Hayashi, S.; Yamamoto, K. SizeDependent Near-Infrared Photoluminescence from Ge Nanocrystals Embedded in SiO2 Matrices. Phys. Rev. B: Condens. Matter Mater. Phys. 1998, 58, 7921−7925.

(51) Wheeler, L. M.; Levij, L. M.; Kortshagen, U. R. Tunable Band Gap Emission and Surface Passivation of Germanium Nanocrystals Synthesized in the Gas Phase. J. Phys. Chem. Lett. 2013, 4, 3392− 3396.

(52) Keast, V. J.; Scott, A. J.; Brydson, R.; Williams, D. B.; Bruley, J. Electron Energy-Loss Near-Edge Structure - A Tool for the Investigation of Electronic Structure on the Nanometre Scale. J. Microsc. 2001, 203, 135−175.

(53) Deegan, T.; Hughes, G. An X-Ray Photoelectron Spectroscopy Study of the HF Etching of Native Oxides on Ge(111) and Ge(100) Surfaces. Appl. Surf. Sci. 1998, 123−124, 66−70.

(54) Hanrath, T.; Korgel, B. A. A Comprehensive Study of Electron Energy Losses in Ge Nanowires. Nano Lett. 2004, 4, 1455−1461.

(55) Batson, P. E.; Heath, J. R. Electron Energy Loss Spectroscopy of Single Silicon Nanocrystals: The Conduction Band. Phys. Rev. Lett. 1993, 71, 911−914.

(56) Millo, O.; Balberg, I.; Azulay, D.; Purkait, T. K.; Swarnakar, A. K.; Rivard, E.; Veinot, J. G. C. Direct Evaluation of the Quantum Confinement Effect in Single Isolated Ge Nanocrystals. J. Phys. Chem. Lett. 2015, 6, 3396−3402.

(57) Henstrom, W. L.; Liu, C. P.; Gibson, J. M.; Kamins, T. I.; Williams, R. S. Dome-To-Pyramid Shape Transition in Ge/Si Islands Due to Strain Relaxation by Interdiffusion. Appl. Phys. Lett. 2000, 77, 1623−1625.

(58) Xia, G. Interdiffusion in Group IV Semiconductor Material Systems: Applications, Research Methods and Discoveries. Science Bulletin 2019, 64, 1436−1455.

(59) Chang, S. J.; Wang, K. L.; Bowman, R. C.; Adams, P. M. Interdiffusion in a Symmetrically Strained Ge/Si Superlattice. Appl. Phys. Lett. 1989, 54, 1253−1255.

(60) Gavelle, M.; Bazizi, E. M.; Scheid, E.; Armand, C.; Fazzini, P. F.; Marcelot, O.; Campidelli, Y.; Halimaoui, A.; Cristiano, F. Study of Silicon-Germanium Interdiffusion from Pure Germanium Deposited Layers. Mater. Sci. Eng., B 2008, 154−155, 110−113.

(61) Lu, W.; Xiang, J.; Timko, B. P.; Wu, Y.; Lieber, C. M. OneDimensional Hole Gas in Germanium/Silicon Nanowire Heterostructures. Proc. Natl. Acad. Sci. U. S. A. 2005, 102, 10046−10051.

(62) Menendez, J.; Kouvetakis, J. Type-I Ge/Ge 1-x-YSi XSn y′ Strained-Layer Heterostructures with a Direct Ge Bandgap. Appl. Phys. Lett. 2004, 85, 1175−1177.

(63) Xu, C.; Gallagher, J. D.; Senaratne, C. L.; Menendez, J.;′ Kouvetakis, J. Optical Properties of Ge-Rich G E1-x S IX Alloys: Compositional Dependence of the Lowest Direct and Indirect Gaps. Phys. Rev. B: Condens. Matter Mater. Phys. 2016, 93, 125206.

(64) Hu, C. W.; Menndez, J.; Tsong, I. S. T.; Tolle, J.; Chizmeshya,′ A. V. G.; Ritter, C.; Kouvetakis, J. Low-Temperature Pathways to GeRich Si 1-x Ge x Alloys via Single-Source Hydride Chemistry. Appl. Phys. Lett. 2005, 87, 1−3.

(65) Ryu, M. Y.; Harris, T. R.; Yeo, Y. K.; Beeler, R. T.; Kouvetakis, J. Temperature-Dependent Photoluminescence of Ge/Si and Ge 1- YSny/Si, Indicating Possible Indirect-To-Direct Bandgap Transition at Lower Sn Content. Appl. Phys. Lett. 2013, 102, 171908.

(66) Barry, S. D.; Yang, Z.; Kelly, J. A.; Henderson, E. J.; Veinot, J. G. C. Synthesis of SixGe1-x Nanocrystals Using Hydrogen Silsesquioxane and Soluble Germanium Diiodide Complexes. Chem. Mater. 2011, 23, 5096−5103.

(67) Watanabe, R.; Yokoi, T.; Kobayashi, E.; Otsuka, Y.; Shimojima, A.; Okubo, T.; Tatsumi, T. Extension of Size of Monodisperse Silica Nanospheres and Their Well-Ordered Assembly. J. Colloid Interface Sci. 2011, 360, 1−7.

(68) Russell, J. L.; Noel, G. H.; Warren, J. M.; Tran, N.-L. L.; Mallouk, T. E. Binary Colloidal Crystal Films Grown by Vertical Evaporation of Silica Nanoparticle Suspensions. Langmuir 2017, 33, 10366−10373.

(69) Wilson, A. R. Detection and Quantification of Low Energy, Low Level Electron Energy Loss Edges. Microsc., Microanal., Microstruct. 1991, 2, 269−279.

CHAPTER 3 - Small-Angle X-Ray Scattering Analysis of Colloidal Crystals and Replica Materials Made From L-Arginine Stabilized Silica Nanoparticles

3.1 Introduction

Colloids are interesting for both fundamental and practical reasons, ranging from their use as model systems of atomic motion in crystals to applications in cosmetics, electronics, optics, catalysis, batteries, diagnostics, and drug delivery.[1–6] A defining characteristic of colloidal systems is the ability to control the size, shape, and surface chemistry of the constituent particles. This flexibility has enabled colloidal particles to be used as building blocks for structurally well-defined two-dimensional (2D) and 3D assemblies that are periodic over nanometer to micron length scales.[7–12] Colloidal assembly is also a starting point for interconnected replica structures of metals, semiconductors, polymers, and inorganic oxides with applications in filtration, sensing, catalysis, optics, and electronics.[13–21]

Latex/polystyrene and silica particles have been widely used as building blocks of colloidal crystals and replica structures because of their ease of synthesis, flexible surface chemistry, colloidal stability, and ease of template removal post-infiltration. However, in both cases, it has been challenging to obtain highly monodisperse particles in the sub-30 nm size range. Stöber *et al.* [22] introduced the ammonia-catalyzed hydrolysis of silicon alkoxides in aqueous media in 1968, and this method and its modifications enabled the synthesis of monodisperse silica nanoparticles with diameters greater than 200 nm. A surfactant-assisted microemulsion approach was later developed to make silica colloids in the 30–60 nm size range.[23,24] The use of non-polar organic solvents and large amounts of surfactants, however, limited the microemulsion approach to certain

applications. A significant breakthrough by Yokoi *et al.* [25] enabled the synthesis of 12–23 nm silica nanoparticles in aqueous media by using amino acids as the catalyst for hydrolysis and condensation of silicon alkoxides. Amino acids stabilized the silica nanoparticles due to their interactions with the surface under basic conditions. Hartlen *et al.*[26] and Watanabe *et al.*[27] further developed this approach and optimized it for sizes ranging from 15 to 200 nm. Their modifications included heterogenous delivery of the silica precursor from an organic layer and separation of the nucleation and growth stages by using a seed-regrowth approach. The as-synthesized silica nanoparticles formed stable colloids due to their high surface charge and hence were suitable for assembly.[26] We have used these particles to make colloidal crystal replica structures of semiconductors, magnetic materials, metals, and composite materials.[28–32]

The successful synthesis of these replica structures has enabled researchers to explore properties in 3D nanostructures, in which the characteristic length scale of a physical phenomenon is comparable to the structural lattice parameter. The ability to control the size of silica nanoparticles in the sub-100 nm regime has also enabled systemic size-dependent studies in these nanostructures.[28]

Previous papers have discussed the effects of void size and ordering in the template colloidal crystalline films on the structure and semiconducting, magnetic, acoustic, and plasmonic properties of replica materials.[28–32] Some of these properties are a function of the porosity of the structure, for example, thermal transport, whereas others such as quantum confinement in semiconductors depend more on the pore size of the template. Transport properties such as electronic conductivity and cooperative phenomena such as ferromagnetism are significantly affected by the interconnectivity and long-range order of the nanostructures. Therefore, understanding of the structures and degree of order in the

nanoparticle templates is crucial to understand and tune the properties of the derived replicas.

The 3D structure of colloidal assemblies made from particles of different sizes and compositions has been characterized by real-space imaging and by reciprocal space techniques. Real-space imaging techniques include confocal microscopy,[33–35] FIB-scanning electron microscopy (SEM)/transmission electron microscopy (TEM) tomography,[36,37] and X-ray tomography/microscopy,[38–40] and reciprocal space techniques include light scattering (static, dynamic, small angle, and multiple angle),[41–43] and X-ray scattering (small angle,[44–47] grazing incidence,[48–50] micro radian, [51] and ultra-small angle[52–55]). Often real and reciprocal space techniques are used in combination as complementary techniques. The adequacy of the characterization technique is determined from the system characteristics (particle size and electron density contrast) and the problems being addressed (size determination, 3D structure, grain size, particle orientation, and defects).

Light scattering and confocal microscopy for 3D structure determination are best suited for structures/particles in the hundreds of nanometers to several microns range due to the diffraction limit of light. Electron/X-ray microscopy tomographic techniques extend on the sub-100 nm scale. They are useful in identifying the local crystal structure and defects. However, rigorous statistical analysis is required to determine the average behavior on a larger scale. X-ray scattering techniques provide information about the structure and particle orientation averaged over several microns with particle sizes ranging from a few nanometers to a few microns. Therefore, grazing-incidence and small-angle X-ray scattering have been commonly used to study large-scale structures and kinetics of nanoparticle superlattices.[56]

Silica colloidal crystals and their replicas in the micro- or nano-meter regime have been studied previously by using light scattering,[57–61] confocal microscopy,[35] TEM/SEM, [61–64] X-ray tomography,[65] and small-angle X-ray scattering (SAXS).[60] The observed crystal structures include hexagonal close-packed (hcp)/random hcp, [59,65] face-centered cubic (fcc),[57,58,64,66,67] and body-centered cubic (bcc), [57,58] depending on the particle size, inter-particle interaction, volume fraction, external forces (centrifugation, shear, and electric field), substrate, and deposition methods/conditions.

In this study, amino acid-stabilized silica particles in the range of 20–125 nm have been synthesized and assembled into colloidal crystals. Earlier reports have shown that the amino acids facilitate hydrogen bonding between particles as they assemble allowing formation of ordered periodic structures as characterized by SEM. [26,27,63] Here, we provide a detailed characterization of the structures of these colloidal materials and their replica by using SAXS and SEM.

3.2 Experimental Methods

3.2.1 Silica nanoparticle synthesis and assembly

Monodisperse silica nanoparticles of 20 to 125 nm diameter were synthesized by using the method described by Hartlen *et al.*[26] and Watanbe *et al.*,[27] as discussed in detail by Russell.[68] The synthesis involves base-catalyzed hydrolysis of a silica precursor, tetraethylorthosilicate (TEOS), in an aqueous medium. Both approaches can be applied to the synthesis of nanoparticles between 14 and 200 nm diameter, and the seed-regrowth approach can be used to obtain larger sizes. However, they implemented different strategies to gain control of the size and dispersity. Hartlen's approach includes a two-

phase reaction with a floating organic layer of cyclohexane to slowly add TEOS to the aqueous reaction mixture. The cyclohexane does not participate in the reaction but slows down the hydrolysis of TEOS, providing control over the nucleation and growth rate of the particles. In the Watanabe synthesis, the organic layer is absent and ethanol is used as co-solvent in the regrowth steps to obtain larger particle sizes.

We used the Watanabe method for synthesis of 20.3, 69.7, and 122.7 nm diameter particles and the Hartlen method for synthesis of 22.7, 31.1, and 48.8 nm particles. All reagents were purchased from Sigma-Aldrich, and nanopure water (Barnstead) was used for synthesis. Table B1 summarizes the type of reaction, concentration of the reagents used for the synthesis, reaction conditions, and deposition conditions. A brief description for both types of reactions is provided below, and a schematic is shown in Figure B1:

One-phase synthesis—20.3 nm particles were prepared by mixing 0.49 mmol of L-arginine, 4.8 mol of water, and 25 mmol of TEOS in a round-bottom flask under constant stirring. The mixture was heated at 70 °C for 24 h. These particles were used as seeds for the synthesis of 69.7 and 122.7 nm particles in a similar one-phase reaction. Briefly, for 122.7 nm particles, 0.27 g of seed solution was added to 1.2 mol of water, 1.5 mol of ethanol containing 0.5 mol of L-arginine, and 25 mmol of TEOS in a round-bottom flask. This solution was heated at 70 °C for 24 h. A similar procedure was followed with different concentrations for the synthesis of 69.7 nm particles as given in Table S1.

Two-phase synthesis ─ For the synthesis of ~22.7 nm particles, a solution of 3.8 mol of water and 0.52 mmol of L-arginine was prepared in a round-bottom flask and maintained with constant stirring. A floating layer of 0.042 mol of cyclohexane was slowly added to the top of this aqueous solution, and the reaction mixture was heated to 60 °C. Once the final temperature was reached, 25 mmol of TEOS was added to the cyclohexane layer slowly and dropwise. The reaction was allowed to continue for 20 h. These particles were

used as seeds for the synthesis of 31.1 and 48.8 nm particles. Briefly, for 31.1 nm particles, 20 mL of seed solution was added to 4 mol of water in a round-bottom flask under constant stirring. A floating layer of 0.09 mol of cyclohexane was added to the solution and heated to 60 °C before dropwise addition of 32 mmol of TEOS. The reaction was left undisturbed for 30 h. 48.8 nm particles were obtained by increasing the reaction time to 48 h with the same reaction mixture.

Vertical deposition for particle assembly—Nanoparticle films were prepared using the vertical deposition technique described by Russell *et al.*[68,86] Briefly, silicon wafers (University Wafers) of ~280 μm thickness and ⟨100⟩ orientation were used as substrates for the colloidal film growth. The wafers were cut into 3 cm × 1 cm pieces and were pre-treated with piranha solution (3:1 concentrated H_2SO_4/30% v/v H_2O_2) for 15–20 min and rinsed with water before deposition (*note*: piranha solution is corrosive and can react violently with organic substances).

The as-prepared silica nanoparticle solutions were diluted to 10× (122.7, 69.7, and 48.8 nm) and 7.5× (20.3, 22.7, and 31.1 nm) for deposition without any further purification. The Si wafers were immersed in the nanoparticle solution at a 30° angle in open plastic vials as shown in Figure S2. These vials were left undisturbed for 2 weeks in a temperature- and humidity-controlled oven. Sizes 20.3, 22.7, 31.1, 48.8, and 69.7 nm were deposited at 40 °C with 82% relative humidity (RH). 122.7 nm particles were deposited at 45 °C and 75–80% RH. The RH was controlled by placing an open crystallizing dish containing an appropriate concentration of NaCl in water in the oven.

The thickness of the films varied between 300 nm and 1.5 μm depending on the nanoparticle size and the position in the substrate. Figure S3 shows a cross-sectional view of films derived from 20.3 to 122.7 nm particles. Smaller nanoparticle sizes tended to result in thicker films.

3.2.2 Infiltration of germanium into the colloidal crystalline films and template etching

HPcCVD was used to fabricate germanium replicas using a 5–10% partial pressure of germane in helium carrier gas with a total pressure of 25–30 MPa. Template films were kept 25 μm apart to ensure spatial confinement in the HPcCVD reactor. Germanium was infiltrated at 325 °C with deposition time ranging from 1 to 3 h depending on template particle size, germane partial pressure, and total pressure of the system. An overlayer of germanium was formed during infiltration after voids in the template were fully filled. The overlayer was removed using chlorine-based reactive ion etching. To prepare germanium replicas without the nano-template, the infiltrated sample was treated with an aqueous 3% HF solution to selectively remove silica, followed by a water and acetone rinse.

3.2.3 Scanning electron microscopy

Silica nanoparticles and films were imaged using a Zeiss SIGMA VP-FESEM and Quanta scanning electron microscope. The particle size analysis was performed using ImageJ software. 50 nanoparticles were measured to obtain each size distribution. For smaller sizes, due to lower image resolution, three particles were measured to obtain the mean size and standard deviation.

3.2.4 Small Angle X-ray Scattering

Transmission SAXS measurements were performed at the Advanced Photon Source, Argonne National Laboratory (Beamline 12-ID-B). A spot size of 200 × 100 μm^2 of 14 keV X-rays was used with 1 s exposure time to collect 2D patterns on a Pilatus 2M detector. Several 2D patterns across different regions on the samples and replica structures were recorded.

2D patterns were indexed assuming the densest layer to be parallel to the substrate. Azimuthal averaging was performed to obtain 1D patterns. Details of close-packed structure simulation are included in the Appendix B.

3.3 Results and Discussion

As in earlier reports,[28,30,31,68] we used evaporation-driven vertical deposition[61] to assemble L-arginine-capped silica nanoparticles into multilayer colloidal crystal films. As the solvent evaporates, particles accumulate at the solvent–air interface as shown in Figure B2. Slow evaporation (controlled by fixed temperature and humidity) results in the growth of ordered films.

Figure 3.1 shows top-view SEM images of colloidal films assembled on silicon wafer substrates. As in other evaporation-based assembly techniques, the drying of the films leads to crack formation, which can be easily seen in SEM images as shown in Figure B4. Boundaries separating grains of different orientations can also be observed (Figure 3.2). For example, regions marked 1 and 2 in Figure 3.2 have grains that are oriented at an angle of ~23° with respect to each other, and region 3 has grains with both (or more) orientations as indicated by its corresponding fast Fourier transform (FFT) pattern. This polycrystalline texture is present in films of silica nanoparticles ranging from 20 to 123 nm diameter and can be identified in their SEM images. Other defects such as vacancies and twin boundaries are also observed in the assembled colloidal crystal films (Figure B4).

In the imaged 2D plane, the particles appear to be in a close-packed arrangement with apparent sixfold symmetry that could represent 111, 0001, and/or 110 planes of fcc, hcp, and bcc structures, respectively. However, the lack of 3D information in the SEM images and the limited 2D views of the top surfaces of the multilayer films do not provide

conclusive information about their bulk structures.

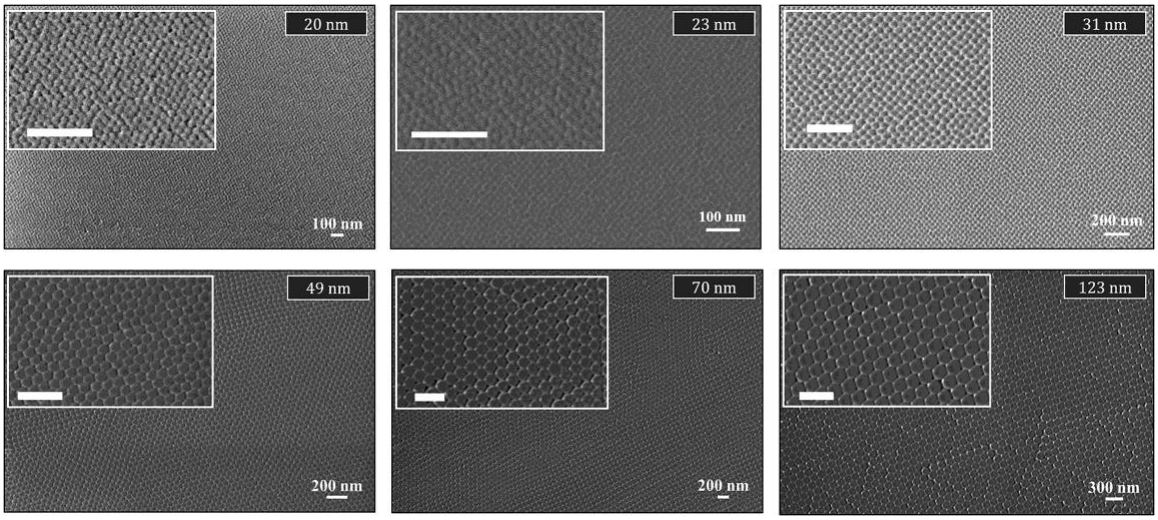

Figure 3.1. Top view of silica nanoparticles assembled as multilayer films on silicon substrates using the vertical deposition technique. Inset images show magnified regions of the corresponding SEM images. The scale bars in the insets correspond to the same lengths as in their parent images.

In SAXS, using a beam spot of 200 × 100 μm^2, a much larger region is interrogated and the 3D arrangement of particles throughout the film (300 nm to 1.5 μm) contributes to the scattering pattern. Thus, 2D SAXS patterns collected in transmission contain information about the structure, orientation, and crystallinity of the colloidal crystal films. We identified representative 2D patterns for each nanoparticle size from scattering patterns of multiple spots in the same sample and/or from multiple samples grown under the same conditions. Figure 3.3 shows representative 2D scattering patterns for 20.3 and 22.7 nm silica particle templates. The scattering patterns can be explained by using the bcc structure with lattice

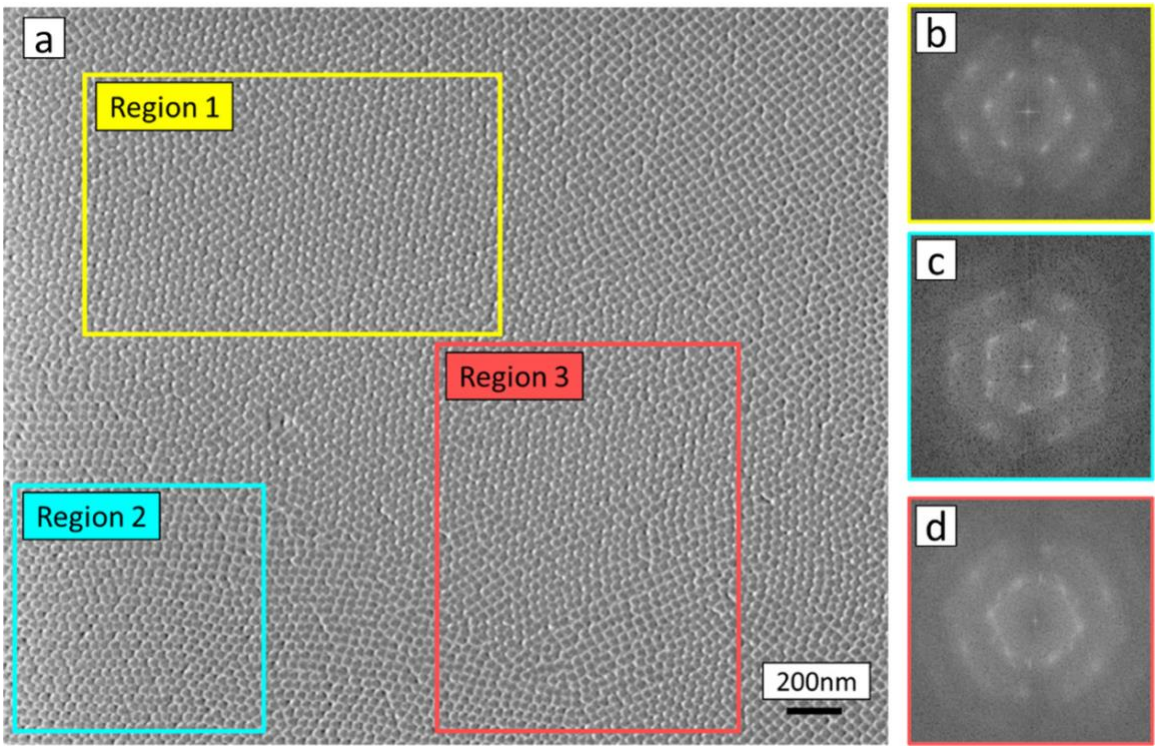

Figure 3.2. SEM images showing grain boundaries and different orientation of grains in a film of 34 nm silica spheres (a) SEM image of top view (b) FFT of region 1 marked in (a), (c) FFT of region 2 and (d) FFT of region 3. In both (a) and FFTs of the corresponding regions, different orientations of the grains can be identified. The grains in regions 1 and 2 appear at an angle of ~23° and region 3 contain multiple grains. Grains of different orientations were observed with other particle sizes as well.

parameters of 25.2 and 32.5 nm for the 20.3 and 22.7 nm templates, respectively. The rings in the 2D patterns represent bcc-structure 3D powders without specific orientations. However, the 2D patterns of the templates also contain bright spots that can be explained by indexing them to oriented single crystals. The indexing of some of these reflections is shown in Figure 3.3; however all of them can be indexed by in-plane rotations of this single-crystal orientation (Figure B5). This implies the presence of multiple crystallites at different angles in the 2D plane with bcc as their 3D structure. Other 2D scattering patterns observed for these two sizes are shown and indexed in the bcc structure in Figures B6

and B7. For sizes larger than 22.7 nm, we use a combination of 2D scattering patterns and their azimuthally averaged 1D patterns to determine the 3D crystal structure. Figure 3.4 shows 2D hexagonal indexing for 48.8, 69.7, and 122.7 nm templates. The 2D patterns can be indexed using 2D-hexagonal system space group *p6mm* with close-packed plane orientation perpendicular to the X-ray beam. The reflections which are not indexed in Figure 3.4 are indexed by rotation of the crystallite in the 2D plane as shown in Figure B8.

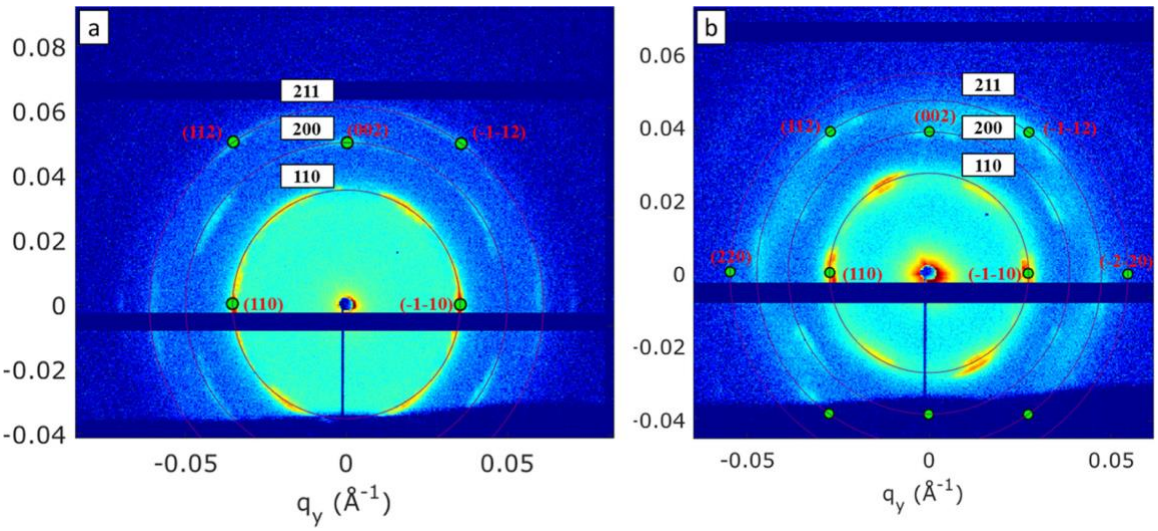

Figure 3.3. (a) 20.3 nm 2D scattering pattern with powder and single crystal fit showing bcc structure (a = 25.2 nm, 2r = 21.8). (b) 23 nm 2D scattering pattern with powder and single crystal indexing showing bcc structure (a = 32.5, 2r = 28.2). Rotations of the orientation of crystallites in the 2D plane explain all the diffraction spots. (Figure B5)

The indexed 2D scattering patterns were used to extract the lattice parameter for these templates. In order to understand the 3D arrangement of the close-packed planes in these templates, azimuthally averaged 1D scattering patterns of simulated close-packed structures were compared with the 1D patterns of the templates. Figure 3.5a shows the simulated 1D patterns for five differently oriented close-packed structures—fcc, hcp, 2D hexagonal (HEX), and random hexagonal close-packed (rhcp) structures.

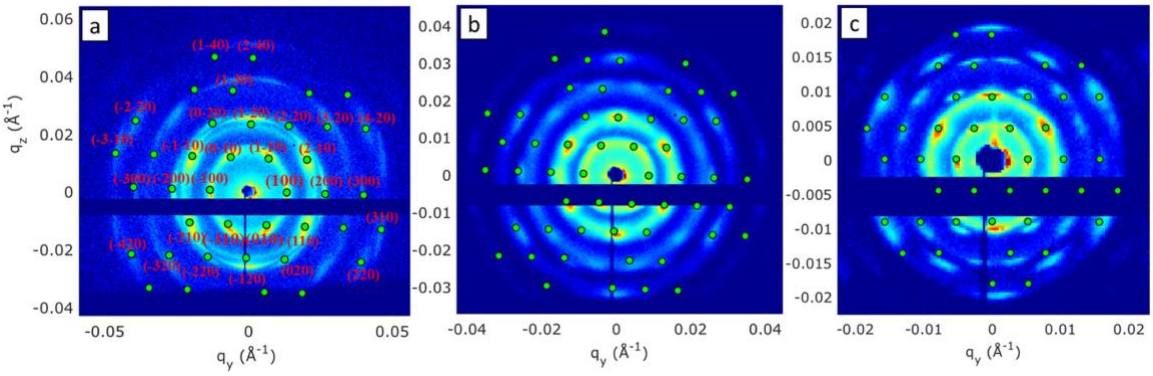

Figure 3.4. 2D hex fit using p6mm space-group and orientation of close pack plane perpendicular to the beam direction (a) 48.8 nm, a = 54.4 (b) 69.7 nm, a = 82.5 nm and (c) 122.7 nm, a = 137.7 nm. The reflections not indexed here can be explained by a different crystallite orientation in the 2D plane as shown in Figure B8.

2D hexagonal represents a 2D close-packed structure labeled A/B/C. In the fcc structure, the stacking of close-packed planes is ABCABC and the 111 plane is perpendicular to the beam. Likewise, for the hcp structure, the 100 plane is perpendicular to the X-ray beam and the stacking is ABABA. In rhcp structures, this stacking of close-packed planes (A/B/C) is random. Figure 3.5a has two types of rhcp structures, where rhcp1 considers the peak shape is still round and rhcp2 assumes the peak shape elongation along the q_z axis.

The 1D patterns obtained by azimuthal averaging of the simulated 2D patterns (Figure B11) highlight the difference between differently oriented close-packed structures. The first reflections observed in fcc is the one at $qD/2\pi = 2$, corresponding to the position of {110} of 2D hexagonal. In hcp, the peak that corresponds to {100} reflection of 2D hexagonal shows up. The major difference between various structures is the relative peak intensity of the first two reflections {100} and {110} reflections. 2D hexagonal shows the highest {100} peak intensity followed by hcp. The rhcp could show any intensity between

that of hcp and fcc depending on the degree of randomness. If there is no registration along the *Z* axis at all, for example, if an AA stacking can occur, rhcp would be no different from 2D hexagonal. The 1D patterns for templates were adjusted using the lattice parameter obtained from the 2D-indexed patterns to overlay with the simulated 1D patterns. From Figure 3.5b, it is evident that the template structure is not fcc. In order to distinguish between the remaining structures, the peak 1/peak 2 ratio was compared. Table B2 shows the peak ratios for different simulated close-packed structures and the different-sized silica templates. The peak ratios for 31.1, 69.7, and 122.7 nm are between rhcp1 and rhcp2, and for 48.8 nm, the peak ratio is between rhcp2 and hcp. These values indicate that the particles assemble in the rhcp structure with possible peak shape elongation along q_z axes. This elongation is also observed in the 2D scattering patterns. However, the reflections are predominantly broad as seen in both 1D/2D patterns, indicating presence of the disordered hexagonal phase.[69] Some sharp reflections are also present, for example, at 48.8 nm $\sim q$ = 1, 2.04 $Å^{-1}$, which indicate a crystalline behavior.

Thus, the smaller sizes 20.3 and 22.7 nm assemble into non-close-packed body-centered cubic structures and sizes 48.8, 69.7, and 122.7 nm assemble into rhcp structures with disordered hexagonal phase. The larger sizes have short-range translational order, and in contrast, smaller sizes have long-range translational order (sharp reflections). In this trend, 31.1 nm is the transition size; its 1D pattern shows similarity with the rhcp1 structure, but there are reflections which cannot be explained by just one structure. These could be multiple structures as shown in Figure B12. The lattice parameter from SAXS for the 31.1 nm template is reported corresponding to *p*6*mm* indexing as carried out for other larger sizes.

There are several factors (both kinetic and thermodynamic)[70−74] that determine the final structure of a colloidal crystal film made by evaporative assembly of charged nanoparticles. The interplay of these parameters is complex, and therefore, it is non-trivial to evaluate each independently. However, we can qualitatively evaluate some of the dominant factors in our system such as charge-based repulsion, poly-dispersity, van der Waals attraction, and shear. Body-centered cubic structures for spherical systems are favored when there is long-range repulsion[75−77] with high dispersity[78,79] and are also formed due to shear-induced transition from close-packed structures.[80,81] Furthermore, investigation is needed to determine their independent influence and combined interplay on the assembly in this study. We have evidence of higher polydispersity in smaller (20.3 and 22.7 nm) sizes compared to larger size (Table B1). The standard deviation in smaller sizes (20.3 and 22.7 nm) was found to be around 5–6.5% whereas for larger sizes, it was lower than 4–5%. This high dispersity could be a contributing factor for formation of the bcc structure. The transition size in this trend, 31.1 nm, also has high dispersity which could be the reason behind its complex behavior with multiple structures.

For larger sizes, the rhcp structure is observed. This behavior is common in sheared spherical colloids. During the vertical deposition process, the particles experience shear, which is known to cause slipping of planes, leading to random stacking.[82] Increased attraction between the larger particles potentially leads to/disorder in these hexagonally packed layers.

This is also reflected in the subtle variation of the number of unit cells in an average grain as a function of particle size. The grain sizes were determined using the full width at half-maximum of the first-order reflections and the Debye Scherrer equation (see Supporting Information for details of the calculation) for different-sized nanoparticle templates. The average number of unit cells in an average grain shows a gradual decrease with the

increasing particle size (Figure 3.6). This trend supports the decrease in the translational order in the templates with increasing size as previously discussed. However, a significant variation is observed in the grain size for all sizes. Grain sizes are known to be influenced by particle size dispersity and by deposition conditions.[83,84]

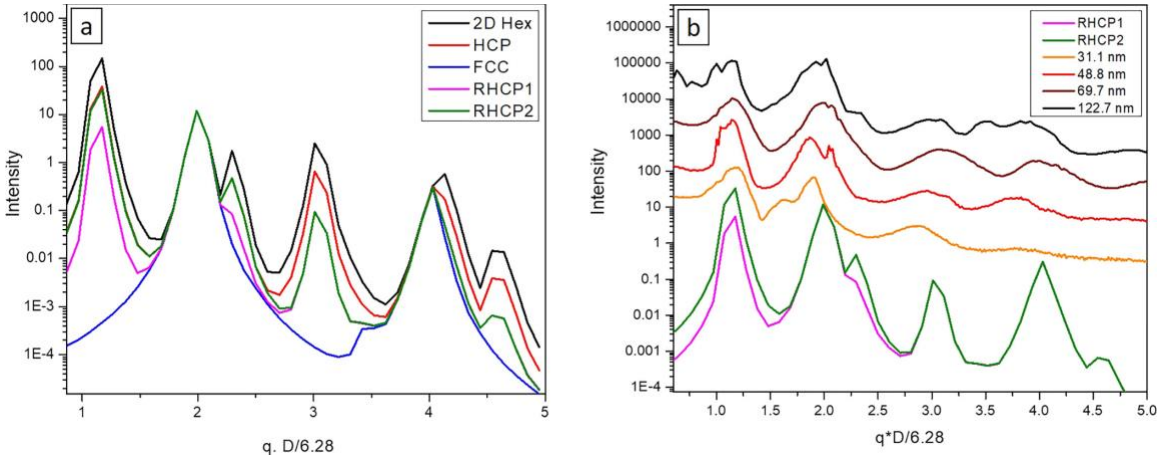

Figure 3.5. (a) Simulated azimuthally averaged 1D patterns of different oriented close pack structures. Corresponding 2D patterns are in Figure B11. (b) Comparison of azimuthally averaged 1D patterns of different sizes with the simulated 1D patterns shown in (a) and Figure B12. Particle size is calculated from the lattice parameter in the SAXS for consistency.

SEM images also show grain boundaries and defects in proximity to anomalously sized particles, as shown in Figure B4. Narrower particle size distributions and a controlled rate of deposition can help to lower the variation in grain size and further decrease the density of grain boundaries. Both large grains and uniform grain sizes are desirable for certain applications of colloidal crystals and their replicas.

The voids in these colloidal crystal films can be infiltrated using high-pressure confined chemical vapor deposition (HPcCVD) and high-pressure supercritical fluid deposition with semiconductors and metals as shown for 48.8 nm template films in Figure 3.7. In order to understand the properties of these 3D nanostructures independent of the template, we used HF to selectively etch away the silica nanoparticles. SEM images after etching

confirm the formation of an interconnected Ge nanostructure as shown in Figure 3.7d. TEM tomography of these systems reported previously has analyzed the variation in the structure between different voids and interconnections.[85] However, as previously discussed, this information is limited to a small region or field of view in the TEM. Because the nanostructure only occupies ~26–32% of the film volume, it is important to confirm the preservation of the long-range structure and ordering in the replica films after template etching.

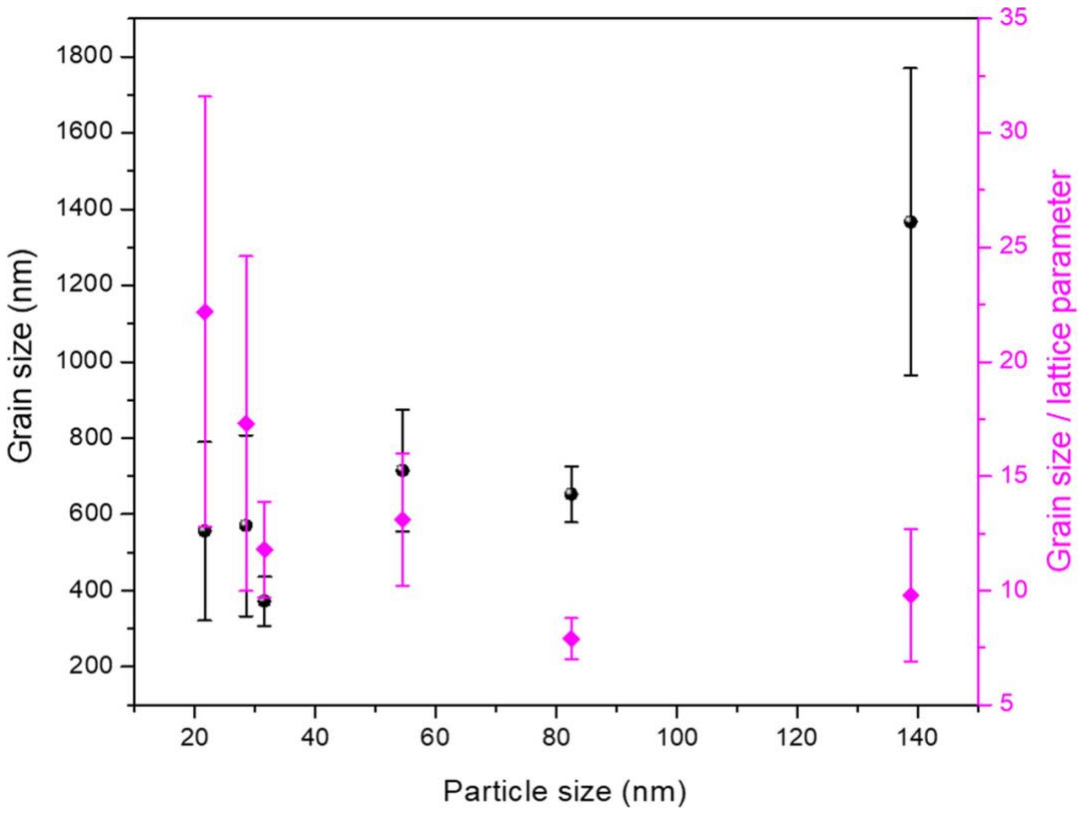

Figure 3.6. Variation in grain size and number of unit cells in a grain as a function of particle size.

Figure 3.7 shows 1D SAXS patterns for a 48.8 nm silica film template, the Ge-infiltrated film, and the Ge nanostructure following template etching. We chose Ge rather than Si for this study due its contrast with silica in the SAXS measurement. The 48.8 nm infiltrated

template and inverse Ge structure also show a similar structure to the template structure. The peak 1/peak 2 ratios in infiltrated and inverse structures are between simulated rhcp1 and rhcp 2. Thus, akin to the template, these also have a rhcp structure with broad reflections, indicating presence of the disordered hexagonal phase. The indexed 2D patterns are shown in Figure B14.

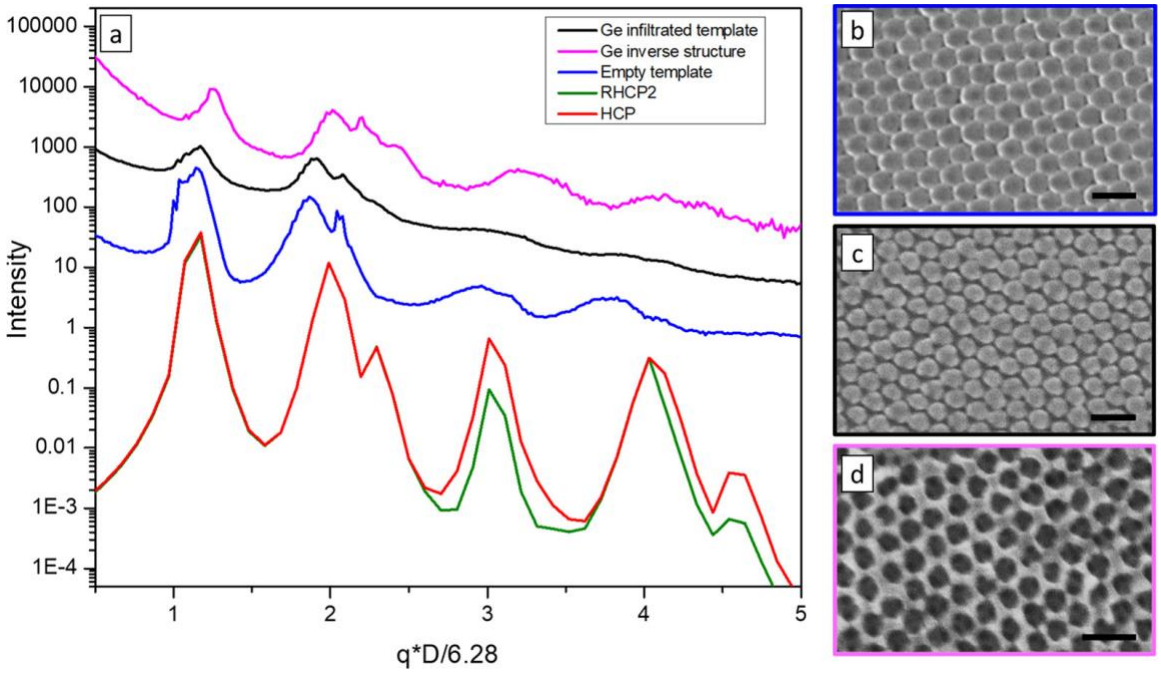

Figure 3.7. (a) Comparison of azimuthally averaged 1D patterns for 48.8 nm empty template, Ge infiltrated template and Ge inverse structure after template removal with simulated 1D patterns for rhcp and hcp. Representative SEM images (top view) of (b) empty silica template film (c) Ge-infiltrated template film and (d) inverse Ge structure. Inset scale bar in SEM images is 100 nm.

This behavior of the inherited template structure is observed at other sizes as well. For smaller sizes, 20.3 and 22.7 nm, inverse Ge also shows a bcc structure like their corresponding templates as shown in Figure B15. In case of 31.1, 69.7, and 122.7 nm, a rhcp structure is formed with peak1/peak 2 ratios varying between rhcp1 and hcp

simulated structures, indicating different stacking patterns and elongation along *z* axes (Table B5 and Figure B17). In these larger sizes, just like their templates, presence of disordered hexagonal phase is observed in the form of broad reflections. This comparison confirms the retention of the structure following semiconductor infiltration and template etching.

3.4 Conclusion

Sub-100 nm monodisperse silica nanoparticles have been synthesized and assembled into 3D structures as films using evaporation-induced vertical deposition. These nanoparticle films were used as templates and infiltrated with germanium to obtain a 3D interconnected replica. Using SEM and SAXS, we have characterized the structure and ordering of the silica nanoparticle templates and the replica materials derived from them. From SEM images, information on particle size and shape, their relative arrangement in the 2D plane, crystallinity, and type of defects was obtained. The particles are spherical in shape with standard deviations in particle size within 6.5% and appear to be in close-packed arrangements within the 2D surface plane. Several SEM images show grains with different orientations in all the films, indicating polycrystallinity. Other defects such as vacancies and cracks due to drying of the films were also observed in SEM images.

More detailed information about the 3D arrangement of the particles could be obtained by SAXS. A size-dependent variation was observed in the colloidal crystal silica films. Particles smaller than 31.1 nm assembled into the non-close-packed bcc structure, whereas particles larger than 31.1 nm assemble into rhcp with disordered hexagonal phase.

We extended this analysis to the infiltrated templates and replica nanostructures after template removal. Using SAXS, we confirmed that the high-temperature and -pressure

infiltration of the template does not affect its structure or ordering. After etching, the replica material retains the template structure.

This study confirms that silica nanoparticle assembly forms a robust model system for template-mediated design of 3D interconnected and periodic nanostructures on the sub-100 nm length scale. A detailed understanding of particle arrangements in the template can help in establishing structure–property relationships in the replica nanostructures. The formation of non-close-packed structures without the use of specific ligand interaction or substrate modification can likely be attributed to particle size dispersity and shear forces in the assembly process. These parameters can in principle be tuned to obtain different structures as needed.

3.5 References

(1) Talapin, D. V.; Lee, J.-S.; Kovalenko, M. V.; Shevchenko, E. V. Prospects of Colloidal Nanocrystals for Electronic and Optoelectronic Applications. Chem. Rev. 2010, 110, 389−458.

(2) Manoharan, V. N. Colloidal Matter: Packing, Geometry, and Entropy. Science 2015, 349, 1253751.

(3) Kumar, S. K.; Kumaraswamy, G.; Prasad, B. L. V.; Granick, S.; Gang, O.; Manoharan, V. N.; Frenkel, D.; Kotov, N. A.; Kotov, N. A. Nanoparticle Assembly: A Perspective and Some Unanswered Questions. Curr. Sci. 2017, 112, 1635−1641.

(4) Boles, M. A.; Engel, M.; Talapin, D. V. Self-Assembly of Colloidal Nanocrystals: From Intricate Structures to Functional Materials. Chem. Rev. 2016, 116, 11220−11289.

(5) Li, F.; Josephson, D. P.; Stein, A. Colloidal Assembly: The Road from Particles to Colloidal Molecules and Crystals. Angew. Chem., Int. Ed. 2011, 50, 360−388.

(6) Pellegrino, T.; Kudera, S.; Liedl, T.; Muñoz Javier, A.; Manna, L.; Parak, W. J. On the Development of Colloidal Nanoparticles towards Multifunctional Structures and Their Possible Use for Biological Applications. Small 2004, 1, 48−63.

(7) Glotzer, S. C.; Solomon, M. J.; Kotov, N. A. Self-Assembly: From Nanoscale to Microscale Colloids. AIChE J. 2004, 50, 2978−2985.

(8) Xu, L.; Ma, W.; Wang, L.; Xu, C.; Kuang, H.; Kotov, N. A. Nanoparticle Assemblies: Dimensional Transformation of Nanomaterials and Scalability. Chem. Soc. Rev. 2013, 42, 3114−3126.

(9) Derrien, T. L.; Hamada, S.; Zhou, M.; Smilgies, D.-M.; Luo, D. Three-Dimensional Nanoparticle Assemblies with Tunable Plasmonics via a Layer-by-Layer Process. Nano Today 2020, 30, 100823.

(10) Park, J. e.; Hickey, D. R.; Jun, S.; Kang, S.; Hu, X.; Chen, X. J.; Park, S. J. Surfactant-Assisted Emulsion Self-Assembly of Nanoparticles into Hollow Vesicle-Like Structures and 2D Plates. Adv. Funct. Mater. 2016, 26, 7791−7798.

(11) Majewski, P. W.; Michelson, A.; Cordeiro, M. A. L.; Tian, C.; Ma, C.; Kisslinger, K.; Tian, Y.; Liu, W.; Stach, E. A.; Yager, K. G.; Gang, O. Resilient Three-Dimensional Ordered Architectures Assembled from Nanoparticles by DNA. Sci. Adv. 2021, 7, No. eabf0617.

(12) Choi, J. J.; Bealing, C. R.; Bian, K.; Hughes, K. J.; Zhang, W.; Smilgies, D.-M.; Hennig, R. G.; Engstrom, J. R.; Hanrath, T. Controlling Nanocrystal Superlattice Symmetry and Shape-Anisotropic Interactions through Variable Ligand Surface Coverage. J. Am. Chem. Soc. 2011, 133, 3131−3138.

(13) Shields, C. W.; Velev, O. D. The Evolution of Active Particles: Toward Externally Powered Self-Propelling and Self-Reconfiguring Particle Systems. Chem 2017, 3, 539−559.

(14) Johnson, S. A.; Ollivier, P. J.; Mallouk, T. E. Ordered Mesoporous Polymers of Tunable Pore Size from Colloidal Silica Templates. Science 1999, 283, 963−965.

(15) Yan, H.; Blanford, C. F.; Holland, B. T.; Parent, M.; Smyrl, W. H.; Stein, A. A Chemical Synthesis of Periodic Macroporous NiO and Metallic Ni. Adv. Mater. 1999, 11, 1003−1006.

(16) Braun, P. V.; Wiltzius, P. Electrochemically Grown Photonic Crystals. Nature 1999, 402, 603−604.

(17) Vlasov, Y. A.; Yao, N.; Norris, D. J. Synthesis of Photonic Crystals for Optical Wavelengths from Semiconductor Quantum Dots. Adv. Mater. 1999, 11, 165−169.

(18) Zakhidov, A. A.; Baughman, R. H.; Iqbal, Z.; Cui, C.; Khayrullin, I.; Dantas, S. O.; Marti, J.; Ralchenko, V. G. Carbon Structures with Three-Dimensional Periodicity at Optical Wavelengths. Science 1998, 282, 897−901.

(19) Gates, B.; Yin, Y.; Xia, Y. Fabrication and Characterization of Porous Membranes with Highly Ordered Three-Dimensional Periodic Structures. Chem. Mater. 1999, 11, 2827−2836.

(20) Velev, O. D.; Jede, T. A.; Lobo, R. F.; Lenhoff, A. M. Porous Silica via Colloidal Crystallization [9]. Nature 1997, 389, 447−448.

(21) Kotov, N. A.; Liu, Y.; Wang, S.; Cumming, C.; Eghtedari, M.; Vargas, G.; Motamedi, M.; Nichols, J.; Cortiella, J. Inverted Colloidal Crystals as Three-Dimensional Cell Scaffolds. Langmuir 2004, 20, 7887−7892.

(22) Stöber, W.; Fink, A.; Bohn, E. Controlled Growth of Monodisperse Silica Spheres in the Micron Size Range. J. Colloid Interface Sci. 1968, 26, 62−69.

(23) Osseo-Asare, K.; Arriagada, F. J. Preparation of SiO2 Nanoparticles in a Non-Ionic Reverse Micellar System. Colloids Surf. 1990, 50, 321−339.

(24) Arriagada, F. J.; Osseo-Asare, K. Synthesis of Nanosize Silica in a Nonionic Water-in-Oil Microemulsion: Effects of the Water/ Surfactant Molar Ratio and Ammonia Concentration. J. Colloid Interface Sci. 1999, 211, 210−220.

(25) Yokoi, T.; Wakabayashi, J.; Otsuka, Y.; Fan, W.; Iwama, M.; Watanabe, R.; Aramaki, K.; Shimojima, A.; Tatsumi, T.; Okubo, T. Mechanism of Formation of Uniform-Sized Silica Nanospheres Catalyzed by Basic Amino Acids. Chem. Mater. 2009, 21, 3719−3729.

(26) Hartlen, K. D.; Athanasopoulos, A. P. T.; Kitaev, V. Facile Preparation of Highly Monodisperse Small Silica Spheres (15 to >200 nm) Suitable for Colloidal Templating and Formation of Ordered Arrays. Langmuir 2008, 24, 1714−1720.

(27) Watanabe, R.; Yokoi, T.; Kobayashi, E.; Otsuka, Y.; Shimojima, A.; Okubo, T.; Tatsumi, T. Extension of Size of Monodisperse Silica Nanospheres and Their Well-Ordered Assembly. J. Colloid Interface Sci. 2011, 360, 1−7.

(28) Chen, W.; Talreja, D.; Eichfeld, D.; Mahale, P.; Nova, N. N.; Cheng, H. Y.; Russell, J. L.; Yu, S.-Y.; Poilvert, N.; Mahan, G.; Mohney, S. E.; Crespi, V. H.; Mallouk, T. E.; Badding, J. V.; Foley, B.; Gopalan, V.; Dabo, I. Achieving Minimal Heat Conductivity by Ballistic Confinement in Phononic Metalattices. ACS Nano 2020, 14, 4235−4243. (29) Abad, B.; Knobloch, J. L.; Frazer, T. D.; Hernández-Charpak, J. N.; Cheng, H. Y.; Grede, A. J.; Giebink, N. C.; Mallouk, T. E.; Mahale, P.; Nova, N. N.; Tomaschke, A. A.; Ferguson, V. L.; Crespi, V. H.; Gopalan, V.; Kapteyn, H. C.; Badding, J. V.; Murnane, M. M. Nondestructive Measurements of the Mechanical and Structural Properties of Nanostructured Metalattices. Nano Lett. 2020, 20, 3306−3312.

(30) Mahale, P.; Moradifar, P.; Cheng, H. Y.; Nova, N. N.; Grede, A. J.; Lee, B.; De Jesus, L. R.; Wetherington, M.; Giebink, N. C.;´ Badding, J. V.; Alem, N.; Mallouk, T. E. Oxide-Free ThreeDimensional Germanium/Silicon Core-Shell Metalattice Made by High-Pressure Confined Chemical Vapor Deposition. ACS Nano 2020, 14, 12810−12818.

(31) Liu, Y.; Kempinger, S.; He, R.; Day, T. D.; Moradifar, P.; Yu, S.- Y.; Russell, J. L.; Torres, V. M.; Xu, P.; Mallouk, T. E.; Mohney, S. E.; Alem, N.; Samarth, N.; Badding, J. V. Confined Chemical Fluid Deposition of Ferromagnetic Metalattices. Nano Lett. 2018, 18, 546− 552.

(32) Chen, Y.; Liu, Y.; Moradifar, P.; Glaid, A. J.; Russell, J. L.; Mahale, P.; Yu, S. Y.; Culp, T. E.; Kumar, M.; Gomez, E. D.; Mohney, S. E.; Mallouk, T. E.; Alem, N.; Badding, J. V.; Liu, Y. Quantum Transport in Three-Dimensional Metalattices of Platinum Featuring an Unprecedentedly Large Surface Area to Volume Ratio. Phys. Rev. Mater. 2020, 4, 035201.

(33) Mohraz, A.; Solomon, M. J. Direct Visualization of Colloidal Rod Assembly by Confocal Microscopy. Langmuir 2005, 21, 5298− 5306.

(34) Varadan, P.; Solomon, M. J. Direct Visualization of Long-Range Heterogeneous Structure in Dense Colloidal Gels. Langmuir 2003, 19, 509−512.

(35) Van Blaaderen, A.; Wiltzius, P. Real-Space Structure of Colloidal Hard-Sphere Glasses. Science 1995, 270, 1177−1179.

(36) Van Der Hoeven, J. E. S.; Van Der Wee, E. B.; De Winter, D. A. M.; Hermes, M.; Liu, Y.; Fokkema, J.; Bransen, M.; Van Huis, M. A.; Gerritsen, H. C.; De Jongh, P. E.; Van Blaaderen, A. Bridging the Gap: 3D Real-Space Characterization of Colloidal Assemblies via FIBSEM Tomography. Nanoscale 2019, 11, 5304−5316.

(37) Boneschanscher, M. P.; Evers, W. H.; Qi, W.; Meeldijk, J. D.; Dijkstra, M.; Vanmaekelbergh, D. Electron Tomography Resolves a Novel Crystal Structure in a Binary Nanocrystal Superlattice. Nano Lett. 2013, 13, 1312−1316.

(38) Hilhorst, J.; Van Schooneveld, M. M.; Wang, J.; De Smit, E.; Tyliszczak, T.; Raabe, J.; Hitchcock, A. P.; Obst, M.; De Groot, F. M. F.; Petukhov, A. V. Three-Dimensional Structure and Defects in Colloidal Photonic Crystals Revealed by Tomographic Scanning Transmission x-Ray Microscopy. Langmuir 2012, 28, 3614−3620.

(39) Furlan, K. P.; Larsson, E.; Diaz, A.; Holler, M.; Krekeler, T.; Ritter, M.; Petrov, A. Y.; Eich, M.; Blick, R.; Schneider, G. A.; Greving, I.; Zierold, R.; Janßen, R. Photonic Materials for HighTemperature Applications: Synthesis and Characterization by X-Ray Ptychographic Tomography. Appl. Mater. Today 2018, 13, 359−369.

(40) Shabalin, A. G.; Meijer, J.-M.; Dronyak, R.; Yefanov, O. M.; Singer, A.; Kurta, R. P.; Lorenz, U.; Gorobtsov, O. Y.; Dzhigaev, D.; Kalbfleisch, S.; Gulden, J.; Zozulya, A. V.; Sprung, M.; Petukhov, A. V.; Vartanyants, I. A. Revealing Three-Dimensional Structure of an Individual Colloidal Crystal Grain by Coherent X-Ray Diffractive Imaging. Phys. Rev. Lett. 2016, 117, 138002.

(41) Wang, J.; Ahl, S.; Li, Q.; Kreiter, M.; Neumann, T.; Burkert, K.; Knoll, W.; Jonas, U. Structural and Optical Characterization of 3D Binary Colloidal Crystal and Inverse Opal Films Prepared by Direct Co-Deposition. J. Mater. Chem. 2008, 18, 981−988.

(42) Bareigts, G.; Kiatkirakajorn, P.-C.; Li, J.; Botet, R.; Sztucki, M.; Cabane, B.; Goehring, L.; Labbez, C. Packing Polydisperse Colloids into Crystals: When Charge-Dispersity Matters. Phys. Rev. Lett. 2020, 124, 058003.

(43) Pusey, P. N.; Van Megen, W. Phase Behaviour of Concentrated Suspensions of Nearly Hard Colloidal Spheres. Nature 1986, 320, 340−342.

(44) Meijer, J.-M.; Hagemans, F.; Rossi, L.; Byelov, D. V.; Castillo, S. I. R.; Snigirev, A.; Snigireva, I.; Philipse, A. P.; Petukhov, A. V. SelfAssembly of Colloidal Cubes via Vertical Deposition. Langmuir 2012, 28, 7631−7638.

(45) Macfarlane, R. J.; Lee, B.; Jones, M. R.; Harris, N.; Schatz, G. C.; Mirkin, C. A. Nanoparticle Superlattice Engineering with DNA. Science 2011, 334, 204−208.

(46) Korgel, B. A.; Fullam, S.; Connolly, S.; Fitzmaurice, D. Assembly and Self-Organization of Silver Nanocrystal Superlattices: Ordered “Soft Spheres”. J. Phys. Chem. B 1998, 102, 8379−8388.

(47) Lokteva, I.; Koof, M.; Walther, M.; Grübel, G.; Lehmkühler, F. Coexistence of Hcp and Bct Phases during In Situ Superlattice Assembly from Faceted Colloidal Nanocrystals. J. Phys. Chem. Lett. 2019, 10, 6331−6338.

(48) Weidman, M. C.; Yager, K. G.; Tisdale, W. A. Interparticle Spacing and Structural Ordering in Superlattice PbS Nanocrystal Solids Undergoing Ligand Exchange. Chem. Mater. 2015, 27, 474− 482.

(49) Corricelli, M.; Altamura, D.; Curri, M. L.; Sibillano, T.; Siliqi, D.; Mazzone, A.; Depalo, N.; Fanizza, E.; Zanchet, D.; Giannini, C.; Striccoli, M. GISAXS and GIWAXS Study on Self-Assembling Processes of Nanoparticle Based Superlattices. CrystEngComm 2014, 16, 9482−9492.

(50) Kuhlmann, M.; Feldkamp, J. M.; Patommel, J.; Roth, S. V.; Timmann, A.; Gehrke, R.; Müller-Buschbaum, P.; Schroer, C. G. Grazing Incidence Small-Angle X-Ray Scattering Microtomography Demonstrated on a Self-Ordered Dried Drop of Nanoparticles. Langmuir 2009, 25, 7241−7243.

(51) Thijssen, J. H. J.; Petukhov, A. V.; 't Hart, D. C.; Imhof, A.; Van Der Werf, C. H. M.; Schropp, R. E. I.; Van Blaaderen, A. Characterization of Photonic Colloidal Single Crystals by Microradian X-Ray Diffraction. Adv. Mater. 2006, 18, 1662−1666.

(52) Reus, V.; Belloni, L.; Zemb, T.; Lutterbach, N.; Versmold, H. Fusion of Colloidal Crystals Induced by Monovalent and Asymmetric Salt: An Osmotic Pressure and Ultra-Small-Angle X-Ray Scattering Study. Colloids Surf., A 1999, 151, 449−460.

(53) Abramova, V. V.; Sinitskii, A. S.; Grigor'eva, N. A.; Grigor'ev, S. V.; Belov, D. V.; Petukhov, A. V.; Mistonov, A. A.; Vasil'eva, A. V.; Tret'yakov, Y. D. Ultrasmall-Angle X-Ray Scattering Analysis of Photonic Crystal Structure. J. Exp. Theor. Phys. 2009, 109, 29−34.

(54) Matsuoka, H.; Harada, T.; Yamaoka, H. An Exact Evaluation of Salt Concentration Dependence of Interparticle Distance in Colloidal Crystals by Ultra-Small-Angle X-Ray Scattering. Langmuir 2002, 10, 4423−4425.

(55) Harada, T.; Matsuoka, H.; Ikeda, T.; Yamaoka, H. The Mystery of Colloidal Crystal Formation□Novel Aspects Obtained by UltraSmall-Angle X-Ray Scattering. Colloids Surf., A 2000, 174, 79−98.

(56) Li, T.; Senesi, A. J.; Lee, B. Small Angle X-Ray Scattering for Nanoparticle Research. Chem. Rev. 2016, 116, 11128−11180.

(57) Okubo, T. Melting Temperature of Colloidal Crystals of Monodisperse Silica Spheres. J. Chem. Phys. 1992, 96, 2261−2268.

(58) Okubo, T.; Okada, S.; Tsuchida, A. Kinetic Study on the Colloidal Crystallization of Silica Spheres in the Highly Diluted and Exhaustively Deionized Suspensions as Studied by Light-Scattering and Reflection Spectroscopy. J. Colloid Interface Sci. 1997, 189, 337− 347.

(59) Verhaegh, N. A. M.; Van Duijneveldt, J. S.; Van Blaaderen, A.; Lekkerkerker, H. N. W. Direct Observation of Stacking Disorder in a Colloidal Crystal. J. Chem. Phys. 1995, 102, 1416.

(60) Schaefer, D. W.; Martin, J. E.; Wiltzius, P.; Cannell, D. S. Fractal Geometry of Colloidal Aggregates. Phys. Rev. Lett. 1984, 52, 2371.

(61) Jiang, P.; Bertone, J. F.; Hwang, K. S.; Colvin, V. L. SingleCrystal Colloidal Multilayers of Controlled Thickness. Chem. Mater. 1999, 11, 2132−2140.

(62) Russell, J. L.; Tran, N.-L. L.; Mallouk, T. E. Adaptive Shape Ripening and Interparticle Bridging of L-Arginine-Stabilized Silica Nanoparticles during Evaporative Colloidal Crystal Assembly. ACS Appl. Mater. Interfaces 2019, 11, 4568−4577.

(63) Yokoi, T.; Sakamoto, Y.; Terasaki, O.; Kubota, Y.; Okubo, T.; Tatsumi, T. Periodic Arrangement of Silica Nanospheres Assisted by Amino Acids. J. Am. Chem. Soc. 2006, 128, 13664−13665.

(64) Míguez, H.; Meseguer, F.; López, C.; Mifsud, A.; Moya, J. S.; Vázquez, L. Evidence of FCC Crystallization of SiO2 Nanospheres. Langmuir 1997, 13, 6009−6011.

(65) Davis, K. E.; Russel, W. B.; Glantschnig, W. J. Settling Suspensions of Colloidal Silica: Observations and X-Ray Measurements. J. Chem. Soc., Faraday Trans. 1991, 87, 411−424.

(66) Míguez, H.; Meseguer, F.; López, C.; Holgado, M.; Andreasen, G.; Mifsud, A.; Fornés, V. Germanium FCC Structure from a Colloidal Crystal Template. Langmuir 2000, 16, 4405−4408.

(67) Hoogenboom, J. P.; Derks, D.; Vergeer, P.; Van Blaaderen, A. Stacking Faults in Colloidal Crystals Grown by Sedimentation. J. Chem. Phys. 2002, 117, 11320.

(68) Russell, J. L.; Noel, G. H.; Warren, J. M.; Tran, N.-L. L.; Mallouk, T. E. Binary Colloidal Crystal Films Grown by Vertical Evaporation of Silica Nanoparticle Suspensions. Langmuir 2017, 33, 10366−10373.

(69) Marcus, A. H.; Rice, S. A. Observations of First-Order Liquidto-Hexatic and Hexatic-to-Solid Phase Transitions in a Confined Colloid Suspension. Phys. Rev. Lett. 1996, 77, 2577.

(70) Weidman, M. C.; Smilgies, D.-M.; Tisdale, W. A. Kinetics of the Self-Assembly of Nanocrystal Superlattices Measured by RealTime in Situ X-Ray Scattering. Nat. Mater. 2016, 15, 775−781.

(71) Korgel, B. A.; Fitzmaurice, D. Small-Angle x-Ray-Scattering Study of Silver-Nanocrystal Disorder-Order Phase Transitions. Phys. Rev. B: Condens. Matter Mater. Phys. 1999, 59, 14191−14201.

(72) Park, J.; Zheng, H.; Lee, W. C.; Geissler, P. L.; Rabani, E.; Alivisatos, A. P. Direct Observation of Nanoparticle Superlattice Formation by Using Liquid Cell Transmission Electron Microscopy. ACS Nano 2012, 6, 2078−2085.

(73) Smith, D. K.; Goodfellow, B.; Smilgies, D.-M.; Korgel, B. A. Self-Assembled Simple Hexagonal AB2 Binary Nanocrystal Superlattices: SEM, GISAXS, and Defects. J. Am. Chem. Soc. 2009, 131, 3281−3290.

(74) Goodfellow, B. W.; Yu, Y.; Bosoy, C. A.; Smilgies, D.-M.; Korgel, B. A. The Role of Ligand Packing Frustration in BodyCentered Cubic (Bcc) Superlattices of Colloidal Nanocrystals. J. Phys. Chem. Lett. 2015, 6, 2406−2412.

(75) Ackerson, B. J.; Clark, N. A. Shear-Induced Partial Translational Ordering of a Colloidal Solid. Phys. Rev. A: At., Mol., Opt. Phys. 1984, 30, 906.

(76) Kremer, K.; Robbins, M. O.; Grest, G. S. Phase Diagram of Yukawa Systems: Model for Charge-Stabilized Colloids. Phys. Rev. Lett. 1986, 57, 2694.

(77) Monovoukas, Y.; Gast, A. P. The Experimental Phase Diagram of Charged Colloidal Suspensions. J. Colloid Interface Sci. 1989, 128, 533−548.

(78) Cabane, B.; Li, J.; Artzner, F.; Botet, R.; Labbez, C.; Bareigts, G.; Sztucki, M.; Goehring, L. Hiding in plain view: colloidal selfassembly from polydisperse populations. Phys. Rev. Lett. 2016, 116, 208001.

(79) Botet, R.; Cabane, B.; Goehring, L.; Li, J.; Artzner, F. How Do Polydisperse Repulsive Colloids Crystallize? Faraday Discuss. 2016, 186, 229−240.

(80) Bang, J.; Lodge, T. P. Mechanisms and Epitaxial Relationships between Close-Packed and BCC Lattices in Block Copolymer Solutions. J. Phys. Chem. B 2003, 107, 12071−12081.

(81) Park, M. J.; Bang, J.; Harada, T.; Char, K.; Lodge, T. P. Epitaxial Transitions among FCC, HCP, BCC, and Cylinder Phases in a Block Copolymer Solution. Macromolecules 2004, 37, 9064−9075.

(82) Ackerson, B. J.; Hayter, J. B.; Clark, N. A.; Cotter, L. Neutron Scattering from Charge Stabilized Suspensions Undergoing Shear. J. Chem. Phys. 1986, 84, 2344.

(83) Weidman, M. C.; Nguyen, Q.; Smilgies, D.-M.; Tisdale, W. A. Impact of Size Dispersity, Ligand Coverage, and Ligand Length on the Structure of PbS Nanocrystal Superlattices. Chem. Mater. 2018, 30, 807−816.

(84) Gasser, U. Crystallization in three-and two-dimensional colloidal suspensions. J. Phys.: Condens. Matter 2009, 21, 203101.

(85) Yu, S.-Y.; Cheng, H. Y.; Dysart, J. L.; Huang, Z.; Wang, K.; Mallouk, T. E.; Crespi, V. H.; Badding, J. V.; Mohney, S. E. Scanning Transmission Electron Tomography and Electron Energy Loss Spectroscopy of Silicon Metalattices. Sept 2, 2020, arXiv:2009.01111. arXiv preprint.

(86) Russell, J. L.; Tran, N.-L. L.; Mallouk, T. E. Adaptive Shape Ripening and Interparticle Bridging of L-Arginine-Stabilized Silica Nanoparticles during Evaporative Colloidal Crystal Assembly. ACS Appl. Mater. Interfaces 2019, 11, 4568−4577.

CHAPTER 4 – Synthesis, exfoliation, and assembly of oppositely charged nanosheets

4.1 Introduction

Hierarchical functional materials such as superlattices/heterostructures made by 2D nanosheets as building blocks are gaining popularity due to their novel properties arising from the synergistic and interfacial effects between the 2D host layers at a molecular scale[1–3]. The interaction between the vertically stacked 2D sheets has led to enhanced charge transfer/separation, structural changes, improved stabilization, magneto-optical response[4,5], based on the type and composition of 2D nanosheets used for material design.

The emergence of these novel properties in heterostructures has facilitated their applications in catalysis, energy storage, rechargeable batteries, electronic devices (transistors)[6–10]. Hierarchical functional materials based on 2D nanosheets as building blocks range from composite materials (organic-inorganic hybrid materials, polymer-based composites, nanoparticles with 2D nanosheets), meso/microporous lamellar solids, and thin films on planar/curved substrates. For this study, we will focus on the methods for superlattices of only 2D nanosheets, excluding composite materials with nanoparticles, polymers, and hybrid organic materials.

Based on the type of 2D nanosheets – van der Waals (VdW) or charge bearing (oxides and hydroxides) several approaches have been developed to synthesize and tune the superlattice-based nanoarchitectures. In the case of VdW heterostructures composed of chalcogenides, graphene, hBN nanosheets, methods of synthesizing heterostructures include CVD-based direct growth methods, physical or CVD epitaxy, mechanical lift, and stack[1,11].

Charge-bearing nanosheets of oxides and hydroxides are often obtained by exfoliation in solution, and therefore different solution-based approaches have been developed to design their heterostructures[3]. There are broadly three types of assembling methods with nanometer control to synthesize superlattice type heterostructures from charged nanosheets – flocculation, electrostatic deposition, and Langmuir deposition[3,6], as shown in Figure 4.1. Flocculation involves the addition of oppositely charged ions to the existing colloidal solution of nanosheets. This leads to the spontaneous restacking of sheets due to electrostatic attraction. It has been most beneficial in intercalating different ions/polymers/polyoxometalates between the restacked nanosheets. It has also been extended to create lamellar solids from oppositely charged nanosheets example, reduced graphene oxide (rGO) and titanates[12], where the sheets stack alternately, as shown in Figure 4.2a. A significant drawback of this method is that the stacking is random without a defined layer registry and nanosheet orientation.

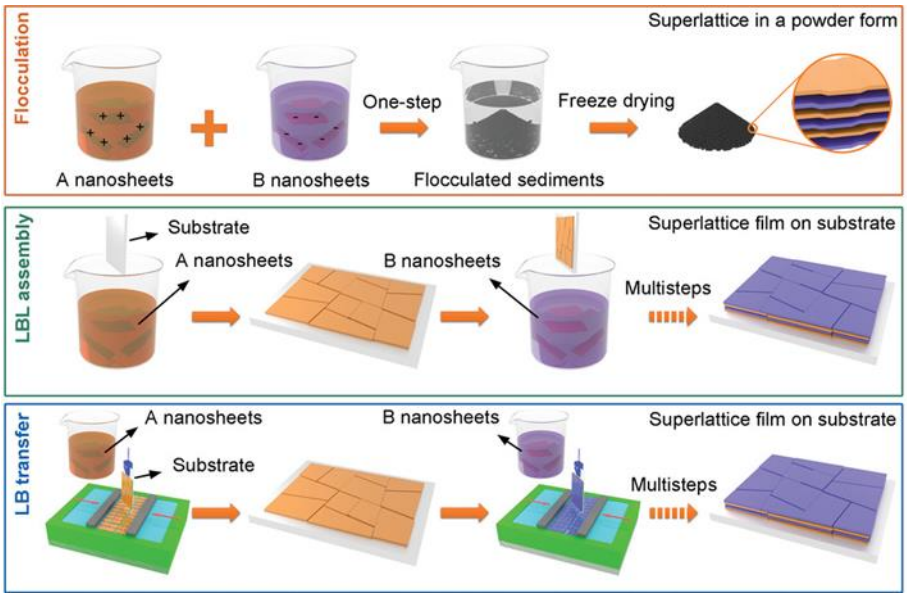

Figure 4.1. Schematic of different approaches to assemble oppositely charged nanosheets. Reprinted from (6), copyright 2019 Advanced Materials

In layer-by-layer deposition, a multilayer is created by alternatingly dipping the substrate in a colloidal suspension of nanosheets and oppositely charged polycation/nanosheet[4,13]. The properties of the multilayer superlattices can be tuned by controlling the cycles of the sequential deposition and thus the thickness[14] (Figure 4.2c). This method has been extended beyond planar substrates to hollow capsules. Layer by layer deposition of nanosheets on colloidal polystyrene particles followed by thermal removal of particles gives hollow crystalline capsules with a larger surface area than a film on a planar substrate[15]. Since this method involves random adsorption of 2D nanosheets, gaps and overlaps exist between the sheet in the multilayer structure. The Langmuir-Blodgett (LB) technique allows for finer control of the deposition process. This method involves the formation of a monolayer of tiled nanosheets at the air-water interface, which can then be transferred by dipping or pulling to a substrate. The obtained nanofilms and nanostructures are densely packed, highly ordered and organized with quality comparable to vapor deposition techniques but with the added advantage of being solution based. This technique has been widely used to make organized crystalline structures with molecular level thickness control and also provide seed layers of nanosheets on variety of substrates. Despite its strengths, the precise control of tuning parameters in this method like the role of substrate surface on the film formation, compression to induce orderly tiling, can make this cumbersome compared to bulk flocculation. Figure 4.2e shows a superlattice created by using the LB technique[16].

The methods mentioned above provide an opportunity to design heterostructures of 2D nanosheets with oppositely charged ions, polymers, and nanosheets. However, there is space to develop a scalable method in bulk like flocculation which provides more precise control over the registry of the 3D arrangement of the 2D nanosheets like obtained in LB deposition.

This type of control on the 3D arrangement of oppositely charged building blocks is well established in the case of nanoparticles. Numerous ways such as ligand-based covalent bonding, polymer-based steric interactions, salt-based screening of electrostatic interactions, and their combinations have been used to create 3D periodic nanostructures[17,18]. In a recent study published by Hueckel *et al*[19]., they introduce a "polymer attenuated Coulombic self-assembly approach" to design nanostructures from

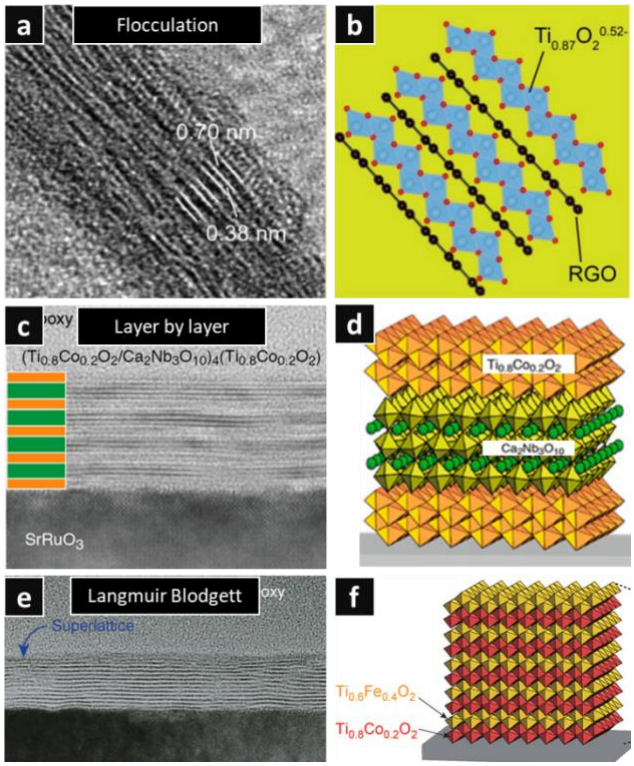

Figure 4.2. TEM and schematic of 2D nanosheet heterostructures made by (a), (b) flocculation. Reprinted from J. Am. Chem. Soc. 2015, 137, 8, 2844–2847, copyright 2015 American Chemical Society (c), (d) layer by layer. Reprinted from J. Am. Chem. Soc. 2016, 138, 24, 7621–7625, copyright 2016 American Chemical Society (e), (f) Langmuir Blodgett. Reprinted from ACS Nano 2011, 5, 9, 6871–6879, copyright 2011 American Chemical Society.

oppositely charged polystyrene nanoparticles. The polystyrene particles have Pluronic surfactants adsorbed on their surface, which act as brushes that allow for the overlap of

electrical double layers and cause steric repulsion, which prevents particles from entering the van der Waals region. The polymer brushes' length and electrostatic attraction were tuned in the system by using different Pluronic surfactants and by adding salt to screen the charges on the particles. This balance between the steric and electrostatic interaction allowed tuning of Debye screening length and, therefore, the assembly of particles. Different structure types such as cesium chloride, C60, sodium chloride, and aluminum diboride were obtained. The self-assembled crystals can also be pulled out of the solution and dried into solid structures.

The approach developed by Heuckel *et al.*[19] has two significant advantages – (1) it is a relatively simple approach based on polymer adsorption to the particle surface and doesn't need covalent bonding and specific functional groups to control particle assembly and (2) It has several convenient tuning parameters such as the length of the polymer brushes, particle sizes and salt concentration to control the final structure of the particles. Considering the uniqueness and versatility of this approach, in this study, we attempted to implement the use of polymer brushes and the steric interaction caused by them to control the assembly of oppositely charged nanosheets in the solution. We used NaTSM and Co-Al LDH as the layered systems for this study.

4.2 Experimental methods

4.2.1 Exfoliation of NaTSM in water and formamide

NaTSM was exfoliated in water/formamide as described by Hata et al20. Briefly, 0.75 g of NaTSM was added to 74.25 g of water (75 ml formamide) and stirred for 24 hours at 500 rpm.

4.2.2 Synthesis and anion exchange of Co-Al LDH

Co-Al carbonate, chloride, and nitrate was synthesized as described by Liu et al[21]. Co-Al carbonate LDH was synthesized by a reflux reaction under nitrogen flow in a two-neck flask. $CoCl_2.6H_2O$, $AlCl_3.6H_2O$, and urea were added to water in the molar ratio of 2:1:7, and the reaction was carried out at 97 °C for 48 hours with stirring at 360 rpm. The transparent solution becomes cloudy as the reaction progresses, and a solid pink precipitate forms. The solution was vacuum filtered and washed with nanopure water and anhydrous ethanol to extract the pink solid which was then dried in air or vacuum at room temperature. The anion exchange of Co-Al carbonate (~0.2 g) was carried out in 200 ml of 3mM HCl solution with 1M NaCl in a conical flask.

The mixture was shaken at 200 rpm for 12 hours to facilitate the exchange. The resulting product was filtered and washed as described for carbonate synthesis. Care was taken to avoid carbonate contamination by using degassed water (purged by nitrogen) for solution preparation and filtration. Co-Al nitrate LDH was synthesized by treating 0.1 g Co-Al chloride with 100 ml 0.1 M KNO_3 and mixing the solution on a shaker at 200 rpm for 12 hours. The filtration and washing treatment was similar to the chloride exchange reaction.

4.2.3 Polymer adsorption

1 ml of exfoliated NaTSM was added to 10 ml of the required concentration (0.8 mM - 6.4 mM) of Pluronic F127 solution prepared in water/formamide and was mixed on a rocking shaker for ~5 min. The mixture was then allowed to sit for 1 hour. The mixture was then centrifuged at 4000 rpm for 10 min, three times to remove excess surfactant. The resulting gel/powder was used for measurements.

4.2.4 X-ray diffraction

Powder X-ray diffraction (XRD) was performed on a Rigaku SmartLab SE with a Cu-Kα radiation source (λ = 0.154 nm) with a tube voltage of 45 mV and a tube current of 40 mA. Diffraction patterns were obtained with a step size of 0.01° (2θ) between 5-70° at a scanning rate of 4° min^{-1}.

4.2.5 Infrared spectroscopy

FT-IR spectroscopy was measured on a Nicolet iS5 spectrometer over a range of 4000 cm^{-1} to 400 cm^{-1} at a resolution of 4 cm^{-1}.

4.2.6 Zeta potential

Zeta potential measurements were done on Malvern Pan-analytical zeta sizer. Values from 10 runs were averaged for each sample.

4.2.7 Scanning electron microscopy

SEM was performed on FEI Quanta 600 FEG Mark II. 10-30 kV voltage was applied, and multiple regions were imaged for each sample.

4.3 Results and discussion

Figure 4.3a shows the XRD of the layered NaTSM structure. The d spacing corresponding to the 001 reflection is 12.28 Å. XRD of the exfoliated nanosheets was collected in both powder and gel form, as shown in Figure 4.3. The powder form restacks back to the layered structure, but the gel form may have some swollen/restacked/flocculated nanosheets, which results in broadening of the reflections, loss of the precise 3D structure, and shift towards lower two theta for some 00l reflections. These observations are complemented by the TEM images of the sheets Figure 4.3c. AFM is required to confirm if the exfoliation process led to single-layer nanosheets or delamination of the layered

crystals into multilayer nanosheets. In this study, we refer to the obtained product as exfoliated NaTSM.

The exfoliated NaTSM was treated with Pluronic F127 to facilitate its adsorption. As shown in Figure 4.4a, the interlayer gallery spacing in the pluronic-treated NaTSM increases from 15.2 Å to 17.6 Å. This increase in gallery height of ~0.24 nm could be due to the adsorption of the polymer on the exfoliated NaTSM surface. Infrared spectroscopy of the polymer-treated NaTSM shows modes characteristic of F127 and NaTSM, as shown in Figure 4.5. Exfoliated NaTSM has a zeta potential of -20 ± -1.18 mV, and post polymer treatment, it is -17.6 ± -0.99 mV. Given the neutral nature of the F127 polymer, the exfoliated system's zeta potential doesn't change after polymer treatment as expected.

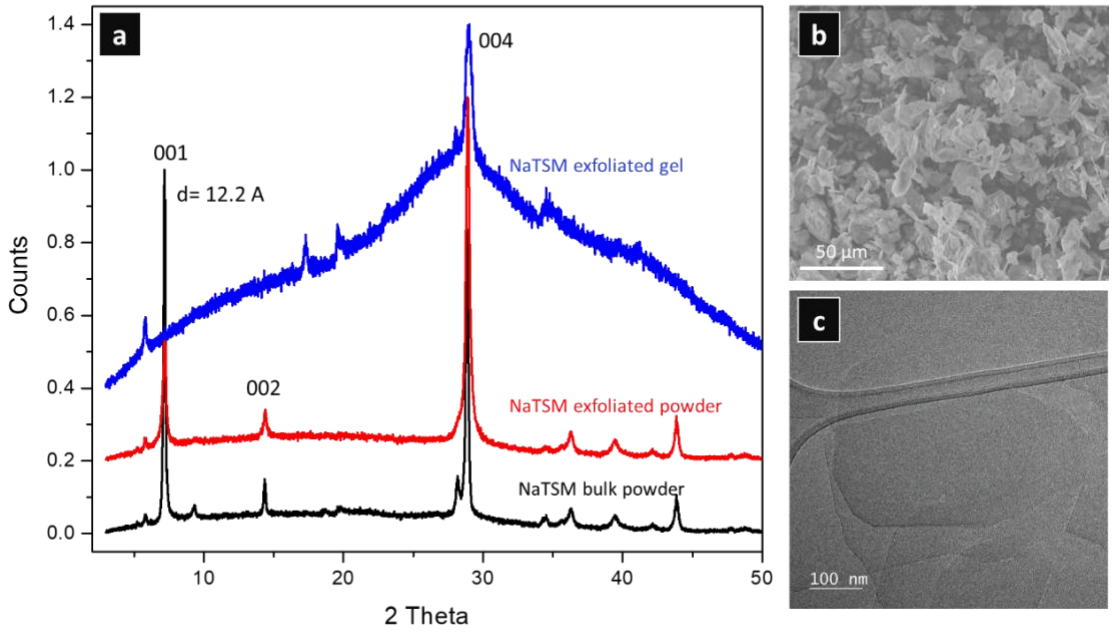

Figure 4.3. (a) XRD of NaTSM powder as purchased, NaTSM exfoliated powder, and NaTSM exfoliated gel (b) SEM image of NaTSM powder (c) TEM image of exfoliated NaTSM.

XRD, TEM and IR measurements indicate the adsorption of polymer on the NaTSM surface but do not provide information about the orientation or density of the polymer on the NaTSM surface. The desired brush effect for steric interactions between oppositely

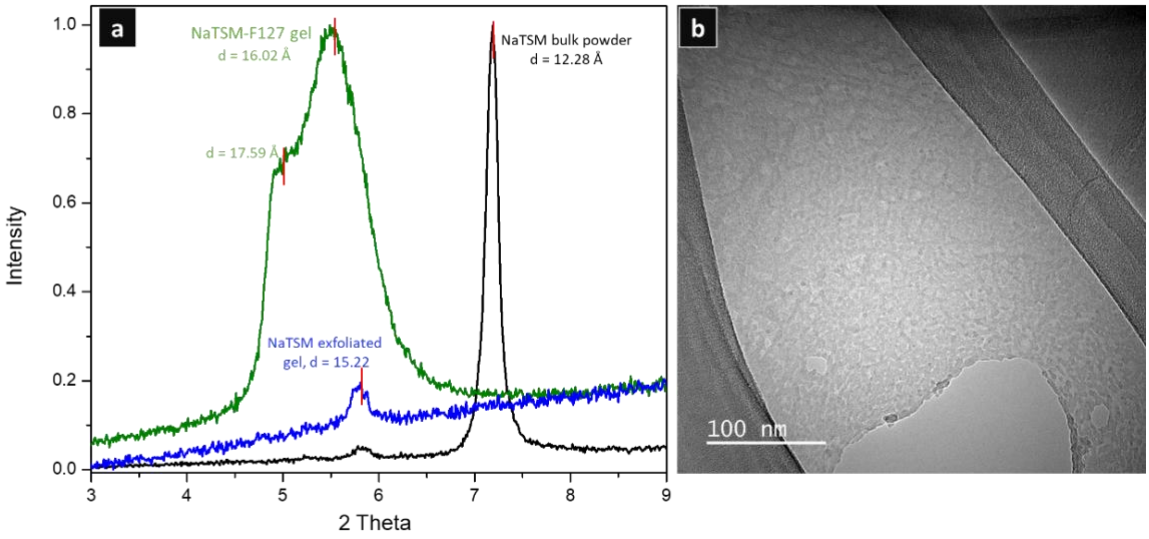

Figure 4.4. (a) XRD of NaTSM exfoliated gel and polymer treated NaTSM exfoliated gel. (b) TEM image of the NaTSM-F127.

charged nanosheets, as described by Heuckel *et al.*[19], is achieved if the F127 adsorbs through the PPO unit uniformly on the surface and the PEO segment extends from the surface (Figure 4.5c). This orientation of polymer adsorption occurs in certain hydrophilic solvents when the PPO block has more affinity for the surface compared to the solvent. The more hydrophilic PEO units dangle into the solution, creating a steric barrier and brush-like effect as the surface is saturated by more preferentially adsorbed PPO units. The surface density of the adsorbed polymer is an interplay of energy of adsorption (-ve) and osmotic repulsion between the brushes (+ve).

These energies are a function of the polymer characteristics (molecular weight, PPO: PEO length ratio), surface-polymer interaction, and the surrounding solvent. The size of a fully extended PEO segment in F127 is ~ 40 nm[22]. However, the thickness of absorbed F127 on a flat surface is a function of the amount of F127 adsorbed and the percentage of PEO

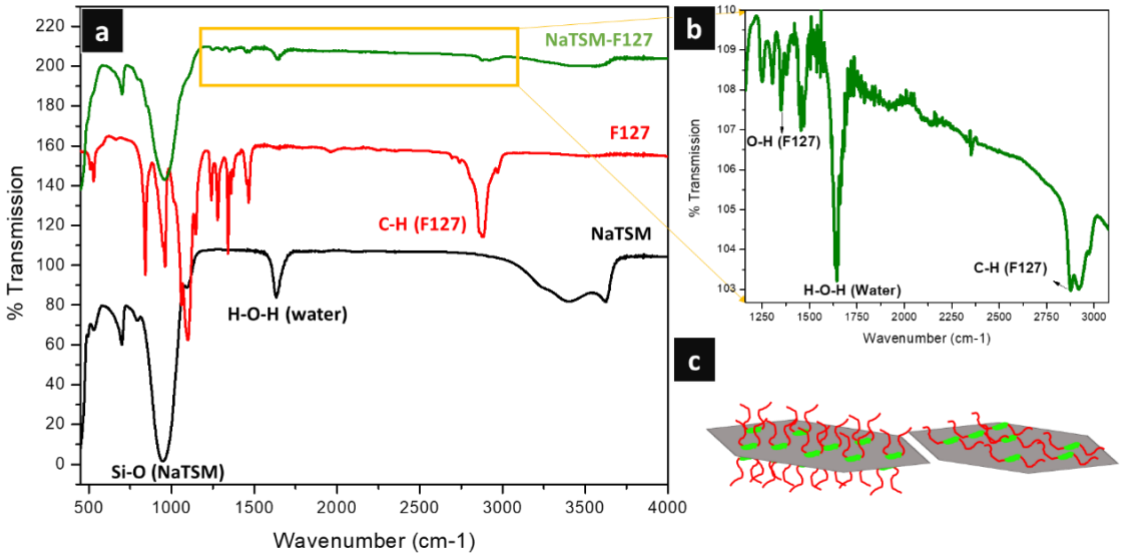

Figure 4.5. (a) IR of NaTSM, F127 and NaTSM-F127. (b) Magnified IR of NaTSM-F127 and (c) Possible confirmations of polymer on NaTSM surface.

extended/coiled from the adsorbed surface. Previous studies on carbon black, silica particles, latex, and laponite crystals have shown an adsorbed thickness of 7.1 nm, 2.5 nm, 8 nm and 3.7 nm for F127, respectively[22,23]. NaTSM could have behavior closest to laponite due to similar chemical and surface composition. Considering the length of fully extended PEO in F127 and the thickness increase in laponite-F127 system, the increase in d spacing observed in NaTSM-F127 implies a coiled/non-extended PEO segment.

One method implemented for obtaining extended orientation of the PEO segment is by increasing the surface density of adsorbed F127. However, in the NaTSM-F127 system increasing the concentration of Pluronic in the solution mixture up to 8x to increase

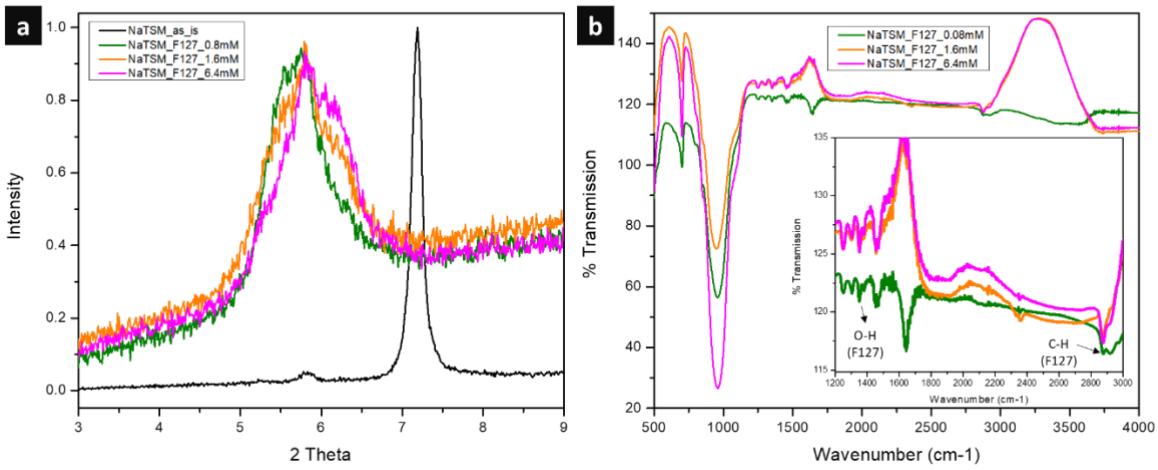

Figure 4.6. XRD and IR of NaTSM-F127 at different F127 concentrations.

adsorption didn't change the interlayer distance (Figure 4.6). At different concentrations, the d spacing remains the same as seen in XRD, and IR shows the presence of modes characteristic of F127.

In this study, the positively charged nanosheets were obtained from Co-Al LDH. As discussed in the methods section, Co-Al LDH were synthesized using a homogeneous co-precipitation method that leads to carbonate as the interlayer anion. Figure 4.7 shows XRD of as-synthesized carbonate Co-Al LDH indexed using Appleman 2 software. The carbonate of the Co-Al LDH was exchanged with chloride anion by a salt-acid treatment. The chloride ion can be easily exchanged with other anions by treating with their sodium/potassium salts. Co-Al LDH with nitrate anion was obtained, as shown in Figure 4.8 and 4.9. The interlayer spacing between the 2D layers changes with different anions, 0.75 nm for Co-Al-CO_3^{2-}, 0.77 nm for Co-Al Cl, and 0.88 nm for Co-Al NO_3^-. The nitrate LDH can be exfoliated in formamide, as discussed in 4.1.1.

Due to the hydrogen bonding between water, interlayer anions, and 2D host layers in LDH, it is exceptionally challenging to exfoliate it into nanosheets in water. Studies have shown that LDH swells and exfoliates in formamide into nanosheets of lateral size in microns[21,24]. Therefore, the solvent system for exfoliation and polymer adsorption was switched from water to formamide.

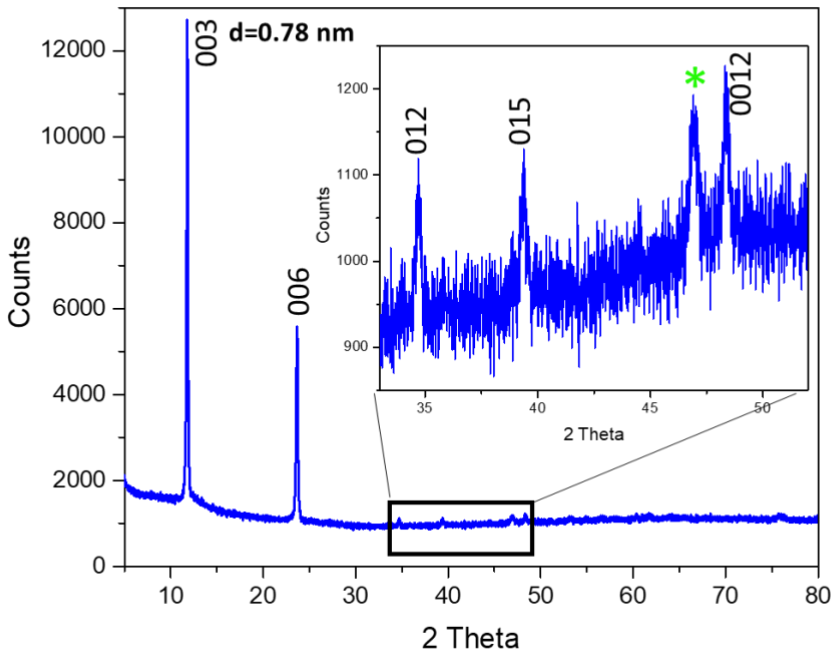

Figure 4.7. XRD of Co-Al carbonate.

Figure 4.10 shows the XRD of NaTSM after exfoliation in formamide. The d spacing is larger in formamide, perhaps due to more swelling. However, with a similar treatment for polymer adsorption, this interlayer spacing doesn't increase as observed in the water phase.

The adsorption and orientation of the polymer as discussed above depends on the polymer's higher affinity to the heterogenous surface compared to the solvent. Formamide being less polar than water could change this affinity of the polymer, and the polymer could prefer staying in solution to being adsorbed on the surface under these reaction conditions.

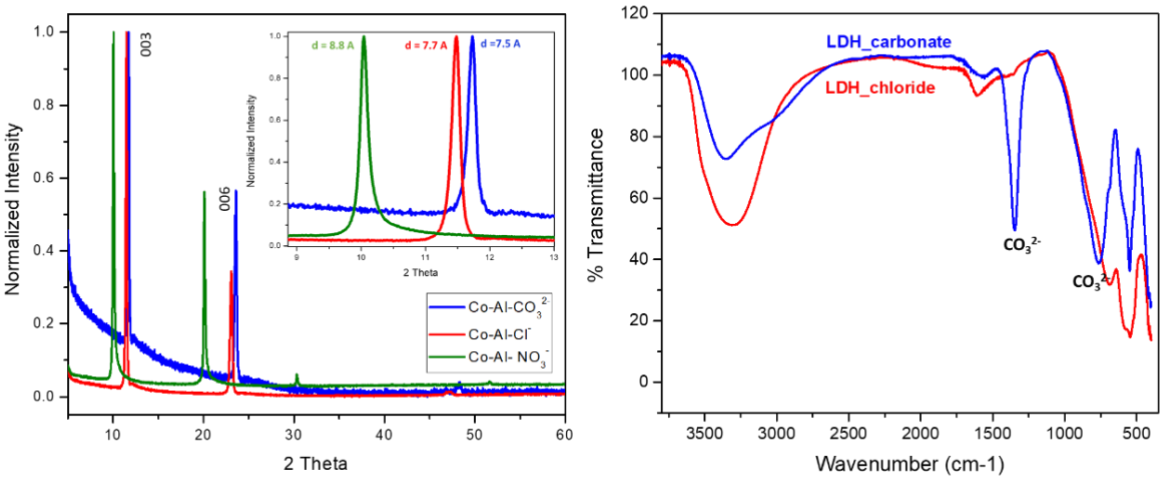

Figure 4.8. Co-Al LDH with different interlayer anions – (a) XRD (b) IR

A more detailed investigation is required to understand the behavior of polymer adsorption on sheets in formamide using advanced techniques such as small-angle neutron scattering, used in earlier studies[23,25–28]. Other wet chemical methods used earlier, such as Baleux[29], are incompatible with this system due to formamide's reactivity. Therefore, SANS would be best suited for NaTSM-LDH-F127 in formamide. A more thorough optimization is also required post-understanding of the adsorption to create a brush-like effect on the nanosheet surface. Other di-block or tri-block co-polymer systems can also be explored to create a similar effect for tunability once the fundamental behavior of PEO-PPO-PEO adsorption on NaTSM and LDH nanosheets is established.

Considering the advanced nature of these studies required for moving forward in this project during the time of COVID-19 pandemic, we decided to pivot the study into another

exciting direction (discussed in chapter 5) which can be investigated in our lab with the available equipment.

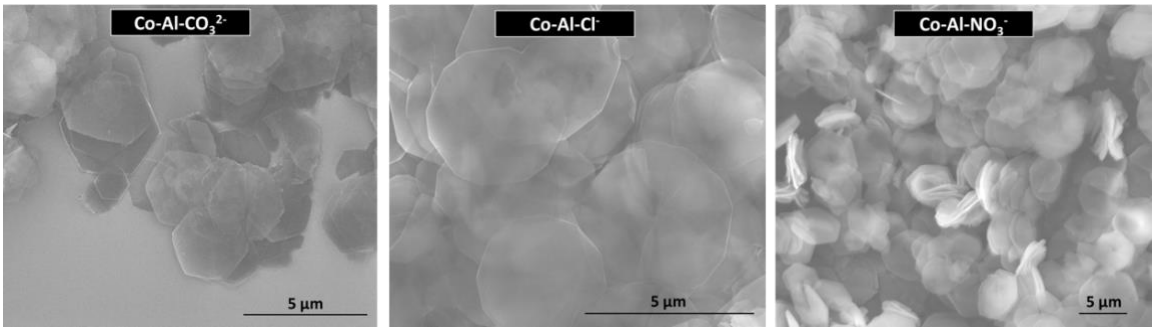

Figure 4.9. SEM images of Co-Al LDHs with different anions

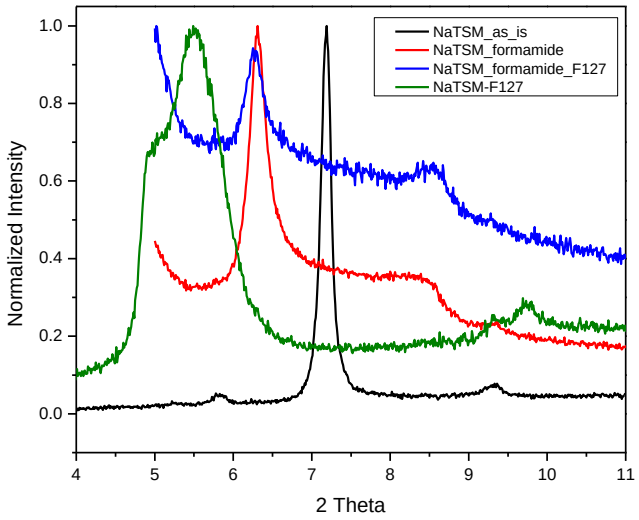

Figure 4.10. XRD of NaTSM exfoliated in formamide and NaTSM-F127 in formamide.

4.4 Conclusions

In this study, we have explored methods for the controlled assembly of oppositely charged nanosheets using tri-block co-polymer F127 to tune interactions between the nanosheets. NaTSM and Co-Al LDH were used as sources for negatively charged and positively charged nanosheets, respectively. Co-Al LDH was synthesized with three different anions

– carbonate, chloride and nitrate. The increased interlayer spacing in Co-Al nitrate allows it to be exfoliated in formamide.

We used two solvent systems – water and formamide for exfoliation and treatment with F127. TEM, XRD, and IR studies reveal exfoliation and adsorption of F127 on NaTSM in water. The interlayer spacing of F127 treated NaTSM is unaffected by the concentration of the F127 added in the solution for adsorption. The orientation and surface density of F127 on NaTSM in water needs to be investigated further. Since the Co-Al LDH system can be exfoliated only in formamide, the NaTSM-F127 system was translated to formamide. However, the XRD of NaTSM-F127 in formamide doesn't indicate adsorption of F127 on the NaTSM surface. Further investigation is needed to understand polymer and NaTSM surface behavior in formamide.

4.5 References

(1) Novoselov, K. S.; Mishchenko, A.; Carvalho, A.; Castro Neto, A. H. 2D Materials and van Der Waals Heterostructures. *Science (80-.).* **2016**, *353* (6298). https://doi.org/10.1126/SCIENCE.AAC9439/ASSET/4B54077E-F0A2-4BB2-BFA1-BC557DC78A9D/ASSETS/GRAPHIC/353_AAC9439_F6.JPEG.

(2) Ma, R.; Sasaki, T. Organization of Artificial Superlattices Utilizing Nanosheets as a Building Block and Exploration of Their Advanced Functions. *https://doi.org/10.1146/annurev-matsci-070214-021202* **2015**, *45*, 111–127. https://doi.org/10.1146/ANNUREV-MATSCI-070214-021202.

(3) Ma, R.; Sasaki, T. Nanosheets of Oxides and Hydroxides: Ultimate 2D Charge-Bearing Functional Crystallites. *Adv. Mater.* **2010**, *22* (45), 5082–5104. https://doi.org/10.1002/ADMA.201001722.

(4) Osada, M.; Ebina, Y.; Takada, K.; Sasaki, T. Gigantic Magneto–Optical Effects in Multilayer Assemblies of Two-Dimensional Titania Nanosheets. *Adv. Mater.* **2006**, *18* (3), 295–299.

https://doi.org/10.1002/ADMA.200501810.

(5) Osada, M.; Itose, M.; Ebina, Y.; Ono, K.; Ueda, S.; Kobayashi, K.; Sasaki, T. Gigantic Magneto-Optical Effects Induced by (Fe/Co)-Cosubstitution in Titania Nanosheets. *Appl. Phys. Lett.* **2008**, *92* (25), 253110. https://doi.org/10.1063/1.2937094.

(6) Xiong, P.; Sun, B.; Sakai, N.; Ma, R.; Sasaki, T.; Wang, S.; Zhang, J.; Wang, G. 2D Superlattices for Efficient Energy Storage and Conversion. *Adv. Mater.* **2020**, *32* (18), 1902654. https://doi.org/10.1002/ADMA.201902654.

(7) Xiong, P.; Wu, Y.; Liu, Y.; Ma, R.; Sasaki, T.; Wang, X.; Zhu, J. Two-Dimensional Organic–Inorganic Superlattice-like Heterostructures for Energy Storage Applications. *Energy Environ. Sci.* **2020**, *13* (12), 4834–4853. https://doi.org/10.1039/D0EE03206A.

(8) Wang, L.; Takada, K.; Kajiyama, A.; Onoda, M.; Michiue, Y.; Zhang, L.; Watanabe, M.; Sasaki, T. Synthesis of a Li−Mn-Oxide with Disordered Layer Stacking through Flocculation of Exfoliated MnO2 Nanosheets, and Its Electrochemical Properties. *Chem. Mater.* **2003**, *15* (23), 4508–4514. https://doi.org/10.1021/CM0217809.

(9) Ebina, Y.; Sasaki, T.; Harada, M.; Watanabe, M. Restacked Perovskite Nanosheets and Their Pt-Loaded Materials as Photocatalysts. *Chem. Mater.* **2002**, *14* (10), 4390–4395. https://doi.org/10.1021/CM020622E/SUPPL_FILE/CM020622E_S.PDF.

(10) Hatakeyama, K.; Tateishi, H.; Taniguchi, T.; Koinuma, M.; Kida, T.; Hayami, S.; Yokoi, H.; Matsumoto, Y. Tunable Graphene Oxide Proton/Electron Mixed Conductor That Functions at Room Temperature. *Chem. Mater.* **2014**, *26* (19), 5598–5604. https://doi.org/10.1021/cm502098e.

(11) Geim, A. K.; Grigorieva, I. V. Van Der Waals Heterostructures. *Nat. 2013 4997459* **2013**, *499* (7459), 419–425. https://doi.org/10.1038/nature12385.

(12) Cai, X.; Ozawa, T. C.; Funatsu, A.; Ma, R.; Ebina, Y.; Sasaki, T. Tuning the Surface Charge of 2d Oxide Nanosheets and the Bulk-Scale Production of Superlatticelike Composites. *J. Am. Chem. Soc.* **2015**, *137* (8), 2844–2847. https://doi.org/10.1021/jacs.5b00317.

(13) Ma, R.; Liu, X.; Liang, J.; Bando, Y.; Sasaki, T. Molecular-Scale Heteroassembly of

Redoxable Hydroxide Nanosheets and Conductive Graphene into Superlattice Composites for High-Performance Supercapacitors. *Adv. Mater.* **2014**, *26* (24), 4173–4178. https://doi.org/10.1002/adma.201400054.

(14) Li, B. W.; Osada, M.; Ebina, Y.; Ueda, S.; Sasaki, T. Coexistence of Magnetic Order and Ferroelectricity at 2D Nanosheet Interfaces. *J. Am. Chem. Soc.* **2016**, *138* (24), 7621–7625. https://doi.org/10.1021/JACS.6B02722/SUPPL_FILE/JA6B02722_SI_001.PDF.

(15) Wang, L.; Sasaki, T.; Ebina, Y.; Kurashima, K.; Watanabe, M. Fabrication of Controllable Ultrathin Hollow Shells by Layer-by-Layer Assembly of Exfoliated Titania Nanosheets on Polymer Templates. *Chem. Mater.* **2002**, *14* (11), 4827–4832. https://doi.org/10.1021/CM020685X.

(16) Osada, M.; Sasaki, T.; Ono, K.; Kotani, Y.; Ueda, S.; Kobayashi, K. Orbital Reconstruction and Interface Ferromagnetism in Self-Assembled Nanosheet Superlattices. *ACS Nano* **2011**, *5* (9), 6871–6879. https://doi.org/10.1021/NN200835V/SUPPL_FILE/NN200835V_SI_001.PDF.

(17) Talapin, D. V.; Lee, J. S.; Kovalenko, M. V.; Shevchenko, E. V. Prospects of Colloidal Nanocrystals for Electronic and Optoelectronic Applications. *Chem. Rev.* **2010**, *110* (1), 389–458. https://doi.org/10.1021/cr900137k.

(18) Si, K. J.; Chen, Y.; Shi, Q.; Cheng, W. Nanoparticle Superlattices: The Roles of Soft Ligands. *Adv. Sci.* **2018**, *5* (1), 1700179. https://doi.org/10.1002/ADVS.201700179.

(19) Hueckel, T.; Hocky, G. M.; Palacci, J.; Sacanna, S. Ionic Solids from Common Colloids. *Nature* **2020**, *580* (7804), 487–490. https://doi.org/10.1038/s41586-020-2205-0.

(20) Hata, H.; Mallouk, T. E.; Kuroda, K. Color Tuning of an Acidic Blue Dye by Intercalation into the Basic Interlayer Galleries of a Poly(Allylamine)/Synthetic Fluoromica Nanocomposite. https://doi.org/10.1021/cm802664j.

(21) Liu, Z.; Ma, R.; Osada, M.; Iyi, N.; Ebina, Y.; Takada, K.; Sasaki, T. Synthesis, Anion Exchange, and Delamination of Co-Al Layered Double Hydroxide: Assembly of the Exfoliated Nanosheet/Polyanion Composite Films and Magneto-Optical Studies. *J. Am.*

Chem. Soc. **2006**, *128* (14), 4872–4880. https://doi.org/10.1021/ja0584471.

(22) Barnes, T. J.; Prestidge, C. A. PEO-PPO-PEO Block Copolymers at the Emulsion Droplet-Water Interface. **2000**. https://doi.org/10.1021/la991217d.

(23) Nelson, A.; Cosgrove, T. Small-Angle Neutron Scattering Study of Adsorbed Pluronic Tri-Block Copolymers on Laponite. *Langmuir* **2005**, *21* (20), 9176–9182. https://doi.org/10.1021/la050680p.

(24) Li, L.; Ma, R.; Ebina, Y.; Iyi, N.; Sasaki, T. Positively Charged Nanosheets Derived via Total Delamination of Layered Double Hydroxides. *Chem. Mater.* **2005**, *17* (17), 4386–4391. https://doi.org/10.1021/cm0510460.

(25) Yurekli, K.; Mitchell, C. A.; Krishnamoorti, R. Small-Angle Neutron Scattering from Surfactant-Assisted Aqueous Dispersions of Carbon Nanotubes. *J. Am. Chem. Soc.* **2004**, *126* (32), 9902–9903. https://doi.org/10.1021/ja047451u.

(26) Granite, M.; Radulescu, A.; Pyckhout-Hintzen, W.; Cohen, Y. Interactions between Block Copolymers and Single-Walled Carbon Nanotubes in Aqueous Solutions: A Small-Angle Neutron Scattering Study. *Langmuir* **2011**, *27* (2), 751–759. https://doi.org/10.1021/la103096n.

(27) Goodwin, D. J.; Sepassi, S.; King, S. M.; Holland, S. J.; Martini, L. G.; Lawrence, M. J. Characterization of Polymer Adsorption onto Drug Nanoparticles Using Depletion Measurements and Small-Angle Neutron Scattering. *Mol. Pharm.* **2013**, *10* (11), 4146–4158. https://doi.org/10.1021/mp400138e.

(28) Patil, R.; Marathe, D.; Roy, S. P.; Ray, D.; Aswal, V. K.; Jha, P. K.; Bahadur, P.; Tiwari, S. Colloidal Stability of Graphene Oxide Nanosheets in Association with Triblock Copolymers: A Neutron Scattering Analysis. *Mater. Sci. Eng. C* **2020**, *109*, 110559. https://doi.org/10.1016/j.msec.2019.110559.

(29) Bohner, M.; Ring, T. A.; Caldwell, K. D. Studies on the Effect of Particle Size and Copolymer Polydispersity on the Adsorption of a PEO/PPO/PEO Copolymer on PS Latex Particles. *Macromolecules* **2002**, *35* (17), 6724–6731. https://doi.org/10.1021/ma0103324.

CHAPTER 5 – Synthesis, thermal characterization and ionic conductivity measurements on Zn-Al and Mg-Al Layered double hydroxides.

5.1 Introduction

In recent years, 2D layered materials and their nanosheets are being explored for ion conductivity and ion transport for applications in electronics, catalysis, selective ion transport, and energy storage devices. Several layered materials such as graphene oxide and vermiculite have shown high proton conductivity[1–6]. For anion conduction, layered double hydroxides (LDH) have garnered a lot of attention[7–17]. The positively charged 2D host layers in LDHs, which have a network of covalently bonded hydroxyl groups, make them a promising material for OH^- conductivity.

Research on the anion conductivity of LDH is motivated by the idea of using inorganic solid electrolyte/anion conductors for electrochemical systems such as alkaline fuel cells and electrolyzers. A shift to the alkaline environment in electrochemical cells is increasing to reduce cost using non-precious catalysts. However, the OH^- ion conductivity is ~ 10^{-3} to 10^{-2} S/cm which is lower than proton conductivity ~ 10^{-1} S/cm in commercially available membrane-based systems. This low OH^- conductivity is due to limitations of the existing anion conducting membranes and also low mobility of hydroxide compared to proton in water. In addition to the low conductivity values, current commercial anion exchange membranes, made of quaternary ammonium polymers, also have toxic synthesis procedures, and poor chemical and thermal stability. Therefore, LDH, as an inorganic material that is stable in alkaline conditions and at high temperatures, is being explored for anion conduction and ion selectivity.

Ion conductivity of different forms of LDH - bulk, lamellar, and nanosheets across different temperature ranges and humidity is being studied[9–12,15,18–23]. Bulk LDH has shown conductivity approaching ~ 10^{-2} S/cm at 200 °C and 100 % relative humidity[19]. This value

decreases, as expected, at lower temperatures and humidity. Different combinations of interlayer anions (chloride, carbonate, hydroxide, nitrate, bromide) and M^{2+}- M^{3+} ions (Mg-Al, Co-Al, Zn-Al, Co-Ni) in the host layer have been explored[18,21]. LDH nanosheets obtained by exfoliation of the bulk LDHs show high-in plane hydroxide ion conductivity approaching~ 10^{-1} S/cm at 60 °C and 80% RH[21]. The in-plane conductivity in nanosheets is one to three orders magnitude higher than their bulk precursors at this temperature and relative humidity. However, the cross-plane conductivity in stacked nanosheets is four to five orders lower than the in-plane conductivity. The anisotropic structure of LDHs is responsible for this large in-plane and cross-plane conductivity difference.

Experimental and theoretical simulations point towards a Grotthuss type mechanism of hydroxide ion conductivity along the plane of LDH 2D host layer/nanosheet[18,24]. The highly ordered and densely packed surface hydroxyl groups form a hydrogen-bonding network with the surrounding water molecules. In the presence of water, hydrolysis of the 2D sheet provides a free hydroxide ion which then hops through the hydroxyl network by rapid hydrogen bond formation and breaking. The hydroxyl ion network doesn't extend in the cross-plane direction, thereby drastically reducing the anion conductivity. Restacking the nanosheets decreases the ionic conductivity because it disrupts the hydrogen bonding network of the surrounding water and increases the electrostatic repulsion of the hydroxyl anion with the interlayer anions under spatial confinement. Therefore, for bulk/restacked LDHs, larger interlayer spacing, lower/monovalent charge of interlayer anions, and higher interlayer water content are associated with better anionic conduction. Interlayer water content is also related to the composition of the 2D host layer and the ratio of M^{2+}/M^{3+} ions as shown for the Mg-Al carbonate system[23]. However, in both nanosheets and bulk LDHs, higher relative humidity is favorable for ionic conductivity due to an increase in the number of surrounding water molecules.

One of the promising applications for LDH is the alkaline fuel cell, given its stability at high temperatures and alkaline environments. Increasing the operating cell temperature between 100-250 °C for fuel cells can increase the efficiency and reduce the cost by using non-precious metallic catalysts. However, most of the work on ionic conductivity of LDH and their application in electrochemical systems has been studied below 100 °C with the exception of a few studies[9,19]. In this study, we have synthesized and characterized Zn-Al and Mg-Al LDH systems with three interlayer anions to understand their hydroxide ion conductivity as a function of temperature in the 100-250°C range for applications in electrochemical systems. We have selected Zn-Al and Mg-Al LDH to separate the effects of electronic conductivity and ionic conductivity.

5.2 Experimental methods

5.2.1 Synthesis of Zn-Al carbonate

Zn-Al carbonate was synthesized as described by Liu et al. [25] Briefly, an aqueous mixture of anhydrous $ZnCl_2$, $AlCl_3.6H_2O$, and urea in molar ratio 2:1:5 was refluxed at 97 °C with magnetic stirring at 360 rpm for 24 hours. A white precipitate forms as the reaction progresses. The white precipitate is extracted by filtration and washed with nanopure water and anhydrous ethanol. The precipitate is dried in air/vacuum at room temperature.

5.2.2 Anion exchange of Zn-Al carbonate

0.2 g of Zn-Al carbonate was added to 200 ml 3mM HCl and 1 M NaCl mixture in a conical flask. The flask was purged with nitrogen and sealed to avoid contamination from atmospheric carbon dioxide. The mixture was shaken at 200 rpm for 12 hours. The obtained product was filtered and washed with degassed water and anhydrous ethanol

under an inert atmosphere. The product was left to dry in inert atmosphere and was retreated according to the same procedure to complete the exchange.

5.2.3 Synthesis of Mg-Al carbonate

Mg-Al carbonate was synthesized hydrothermally as described by Li *et al*[26]. Briefly, 80 ml aqueous mixture of $MgNO_3.6H_2O$ (0.02 mol), $Al(NO_3)_3.9H_2O$ (0.01 mol) and hexamethylenetetramine (0.026 mol) was prepared and heated at 140 °C for 24 hours in a hydrothermal vessel. The white product was washed with water and ethanol and dried in air/vacuum at room temperature.

5.2.4 Anion exchange of Mg-Al carbonate

Anion exchange of Mg-Al carbonate was carried out in the same way as described for Zn-Al LDH with acid (HCl) and salt (NaCl) concentrations being 5 mM and 4.8 M respectively.

5.2.5 Chloride to nitrate ion exchange

0.1 g of chloride LDH was added to 0.1 M 100 ml KNO_3 solution and was shaken at 200 rpm for 12 hours. The exchanged product was filtered and dried as described for the chloride exchange.

5.2.6 X-ray diffraction

Powder X-ray diffraction (XRD) was performed on a Rigaku SmartLab SE with a Cu-Kα radiation source (λ = 0.154 nm) with a tube voltage of 45 mV and a tube current of 40 mA. Diffraction patterns were obtained with a step size of 0.01° (2θ) between 5-70° at a scanning rate of 4° min^{-1}. The collected diffraction patterns were indexed using Appleman 2 software.

5.2.7 Infrared spectroscopy

FT-IR spectroscopy was measured on a Nicolet iS5 spectrometer over a range of 4000 cm^{-1} to 400 cm^{-1} at a resolution of 4 cm^{-1}.

5.2.8 Thermal characterization (DSC-TGA)

Differential Scanning Calorimetry and Thermogravimetric Analysis measurements were performed on NETZSCH'S STA 449 F3 Jupiter. LDH powder was loaded in Pt pans, and the scan was conducted from 25 – 600 °C at 1°C/min in air. The data were analyzed in Origin. The enthalpy associated with loss of water was calculated by integrating the area under the curve (DSC output in mW/mg x time in s). Background subtraction was performed for the water loss peak by defining a local baseline near the peak, as shown in Figure 5.9a and 4.10a inset.

5.2.9 Scanning electron microscopy

SEM was performed on FEI Quanta 600 FEG Mark II. 10-30 kV voltage was applied, and multiple regions were imaged for each sample.

5.2.10 Ion conductivity measurements

A 850 fuel cell testing station by Scribner was used to measure ionic conductivity at different temperatures and relative humidity. Mg-Al carbonate powder (~0.1 g) was pressed into a ~0.5 mm pellet with carbon paper on one side as a contact. Two such pellets (total thickness ~ 1 mm) were then pressed in the fuel cell between the graphite electrodes. Teflon sheets were used to prevent short-circuiting between the graphite electrodes outside the pellet area. A torque of 3N/m was used to tighten the cell before the measurements. 0.35 V of AC voltage was applied with a frequency range of 1 - 0.1 MHz, and impedance was collected as a function of frequency. Zview software was used for fitting the data.

5.3 Results and discussion

Figure 5.1 and 5.2 shows XRD patterns for Zn-Al-CO_3^{2-} and Mg-Al-CO_3^{2-} synthesized by the reflux method[25] and hydrothermal method[26], respectively. The Zn-Al LDH and Mg-Al LDH are crystalline and have a hexagonal crystal structure with interlayer spacings 0.76 nm and 0.75 nm, respectively. The corresponding SEM images show polydisperse platelets with lateral sizes of a few microns.

Carbonate anions have a strong affinity to the host layers, and due to this, LDHs are also used for carbon dioxide capture. However, this strong affinity of carbonate makes it challenging to replace with other anions. Decarbonation of LDHs has been attempted by treatment with inorganic acid solution/vapor[27,28]. The proton from the acid facilitates carbonate

removal by forming bicarbonate, and the corresponding anion acts as an interlayer anion. Though acid treatment allowed for carbonate exchange, it also led to degradation of LDH and weight loss during the process. Another approach for decarbonation was heat

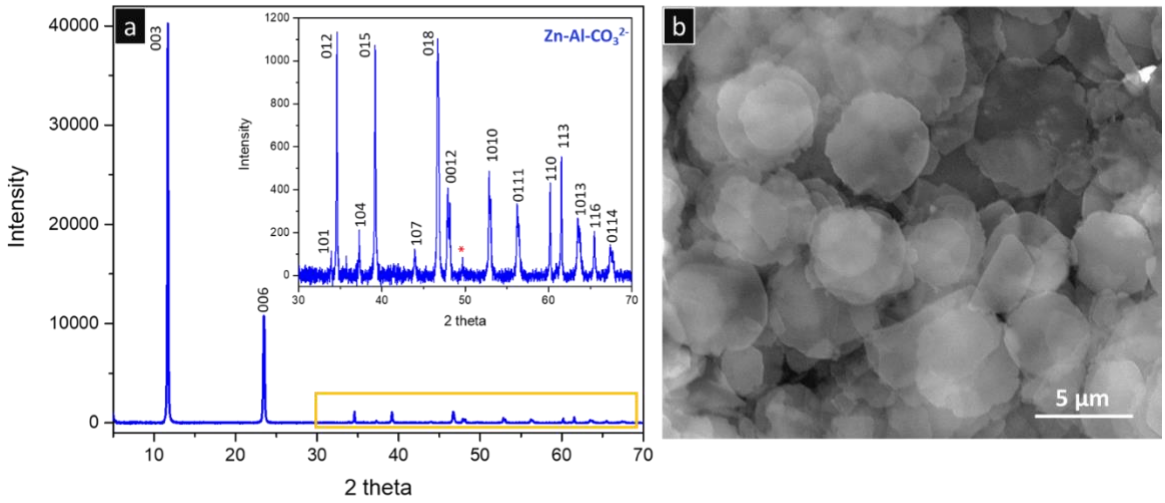

Figure 5.1. (a) Indexed XRD of Zn-Al-CO_3^{2-} (a = b = 3.076 nm, c = 22.809 nm) (b) SEM of Zn-Al-CO_3^{2-}

treatment to expel carbonate as carbon dioxide and then reconstruction of LDH structure using aqueous solution treatment with the desired anion[29,30]. The heat treatment method requires structural reconstruction, which was affected by the number of heat cycles and thus caused degradation. In 2004, Iyi *et al*.[31] developed a salt-acid treatment for decarbonation of LDH, which maintained the crystallinity and structure while achieving complete exchange. The salt-acid method is based on the acid treatment method; however, adding salt drastically improves anion exchange without degrading the LDH structure.

The concentration of acid and salt required to obtain complete decarbonation without weight loss is a function of the amount of carbonate in the formula unit of LDH, type, and the ratio of M^{2+}/M^{3+} ions in the 2D host layers[31,32]. We have optimized this ratio and reaction conditions for the LDHs synthesized in this study.

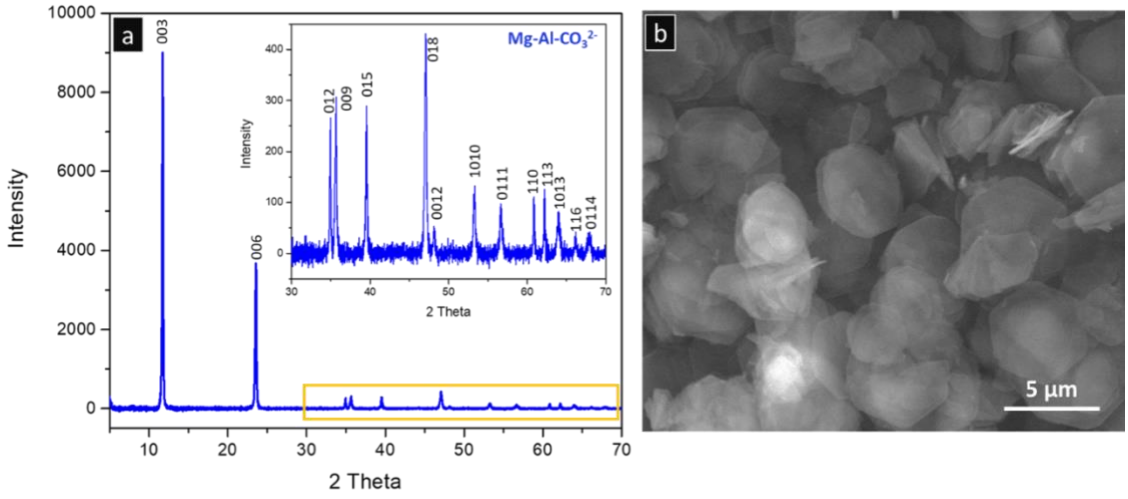

Figure 5.2. (a) Indexed XRD of Mg-Al-CO_3^{2-} (a = b = 3.046 nm, c = 22.772 nm) (b) SEM of Mg-Al-CO_3^{2-}

Due to the high affinity of carbonate to LDH, it is also essential to prevent any carbonate contamination during the exchange process. It has been observed for the Mg-Al carbonate system that the intercalated carbonate dynamically exchanges with the carbon dioxide in the atmosphere within 30 minutes[33]. Therefore, degassed water is used for the exchange process, and filtration is performed in an inert atmosphere.

Zn-Al carbonate was anion exchanged with chloride by salt-acid treatment in this study.

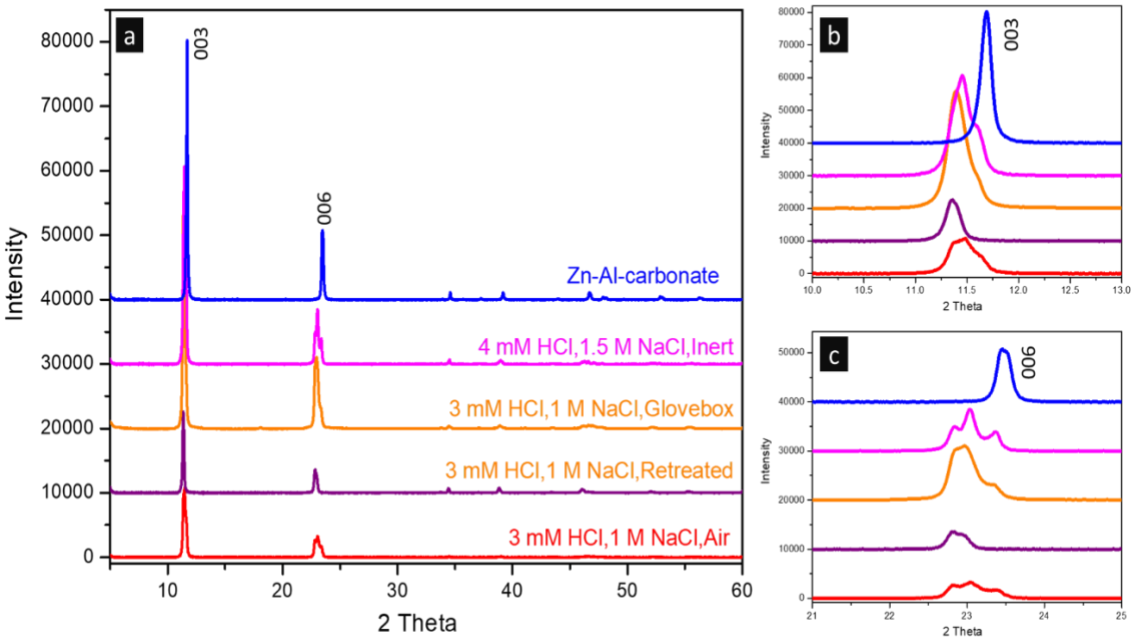

Figure 5.3. (a) XRD of Zn-Al-CO_3^{2-} and Zn-Al-Cl^- obtained by different salt-acid treatment; (b) 003 reflection magnified from (a); (c) 006 reflection magnified from (a).

Figures 5.3 and 5.4 show the XRD and IR of different acid-salt concentrations and filtration conditions. We observed that the inert atmosphere/glove box filtration decreased the carbonate content in the exchanged LDH as seen in the decreased intensity of carbonate-associated XRD peak (2θ = 11.67°) and IR mode (1356 cm^{-1} and 753 cm^{-1}). However, complete exchange was observed by retreatment of the exchanged product. A weight loss

ranging from 20-44% was observed in each treatment. Relatively higher weight loss was observed in the retreatment reaction. This weight loss involves the acid-based breakdown of the LDH structure and loss during filtration/handling of the exchanged product. The SEM images of the exchanged product do not show any morphological changes suggesting that the acid degradation leads to complete dissolution of a fraction of LDH particles and the remaining LDH is intact.

In the case of Mg-Al LDH, a higher concentration of salt-acid, as reported in the literature[34],

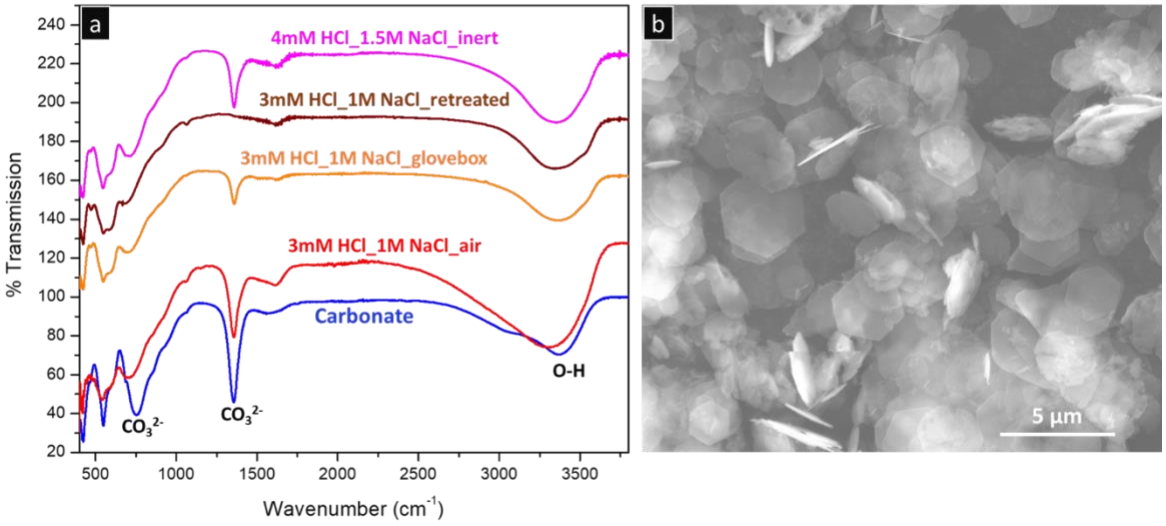

Figure 5.4. FTIR spectrum of Zn-Al-CO_3^{2-} and Zn-Al-Cl^- for different salt-acid treatments

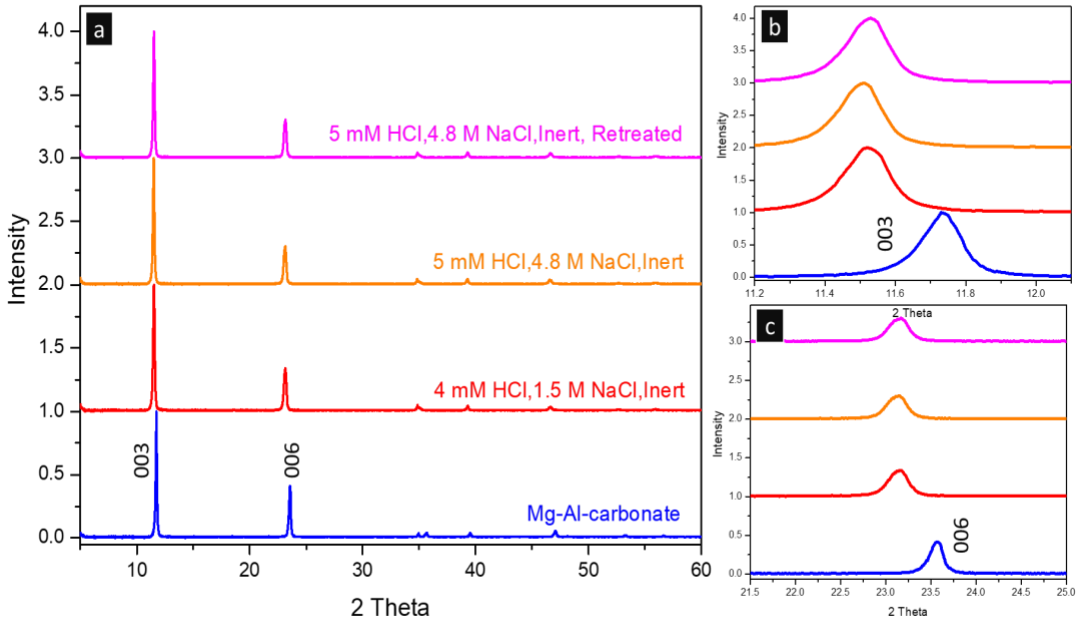

Figure 5.5. (a) XRD of Mg-Al-CO_3^{2-} and Mg-Al-Cl^- obtained by different salt-acid treatment; (b) 003 reflection magnified from (a); (c) 006 reflection magnified from (a).

was used for the exchange reaction. Figures 5.5 and 5.6 shows XRD and IR of the exchanged product with carbonate reference at different salt-acid and reaction conditions.

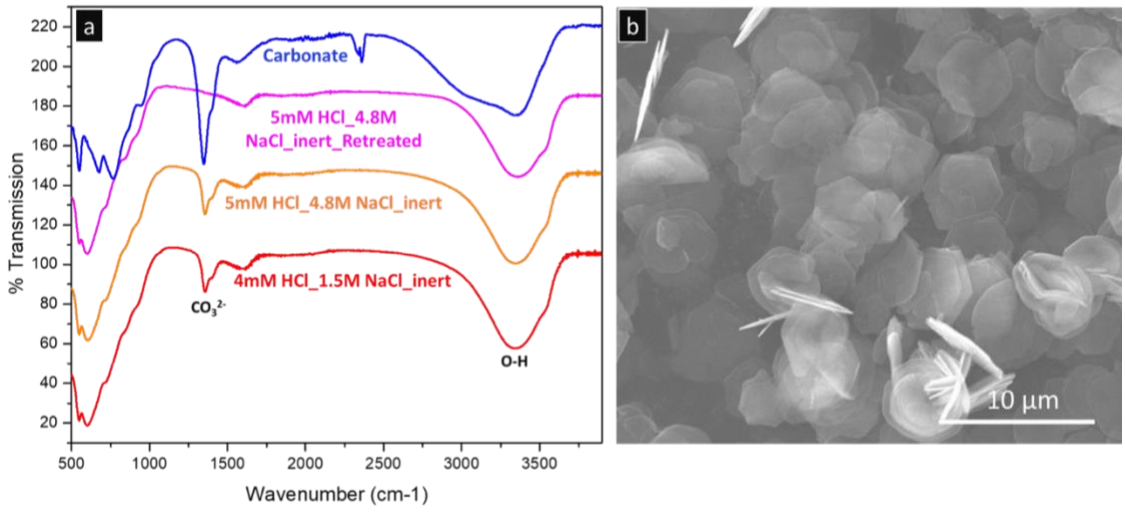

Figure 5.6. FTIR spectrum of Mg-Al-CO_3^{2-} and Mg-Al-Cl^- for different salt-acid treatments

Residual carbonate was seen in the IR vibrational mode and not in XRD reflection, unlike the Zn-Al LDH case. This could indicate a low percentage of carbonate that cannot be detected by XRD. Retreatment was needed to ensure complete exchange as in Zn-Al LDH. However, a relatively lower weight loss (5-23%) was observed in case of Mg-Al LDH.

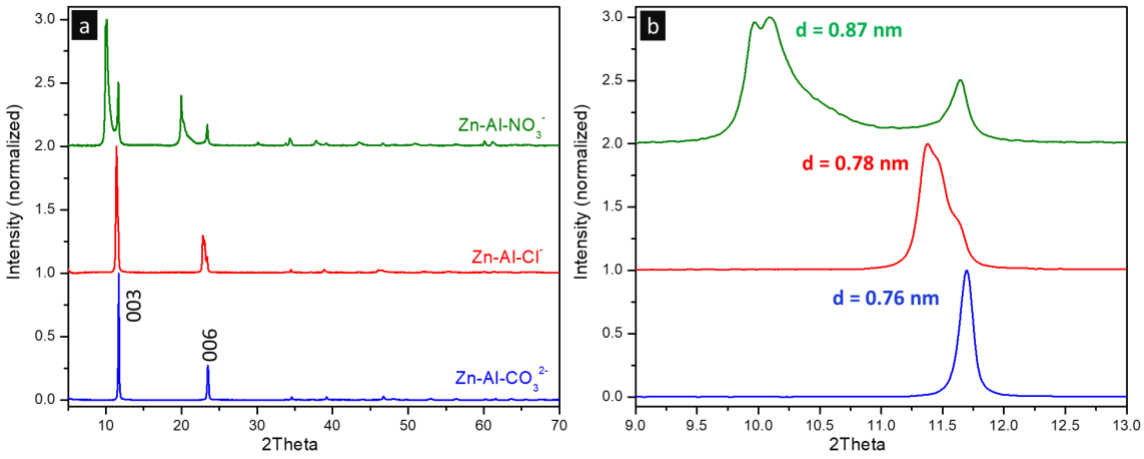

Figure 5.7. (a) XRD of Zn-Al-CO_3^{2-}, Zn-Al-Cl^- and Zn-Al-NO_3^- and (b) Magnified of (a) showing shift towards lower 2θ for 003 reflections and increase in d spacing with anion exchange.

The interlayer spacing increases to 0.78 nm and 0.77 nm in Zn-Al-Cl^- and Mg-Al-Cl^- respectively. The chloride ions are exchanged with nitrate ions by treatment with potassium nitrate solution. The excess nitrate ion in the solution drives the exchange reaction. XRD of the nitrate LDHs shows the increased interlayer spacing of 0.87 nm and 0.84 nm for Zn-Al and Mg-Al LDH, respectively. The nitrate exchange was performed on chloride-LDH with some carbonate; therefore, carbonate can be seen in nitrate-LDH XRD. Splitting in the 003 reflection for nitrate LDH at lower 2θ could be due to increased spacing from hydrated LDH.

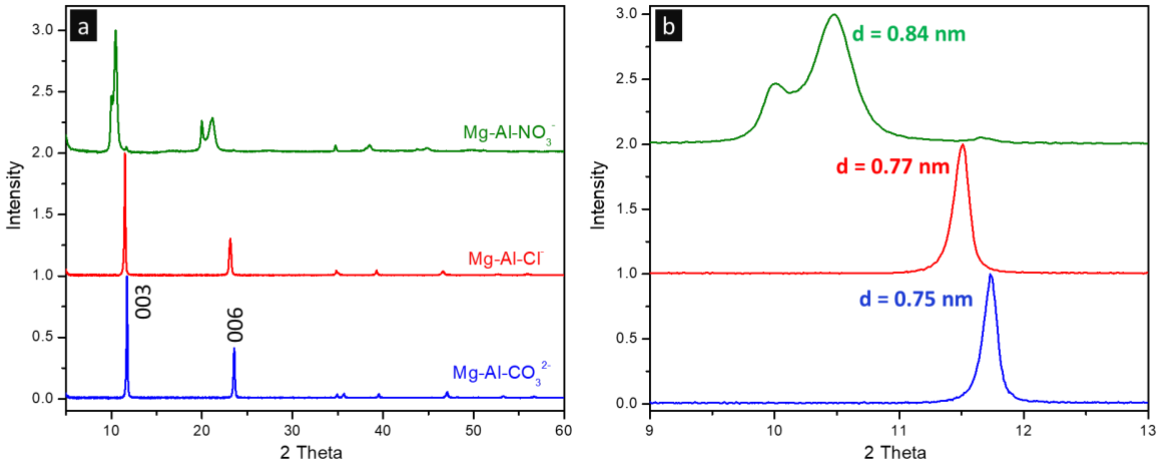

Figure 5.9. (a) XRD of Mg-Al-CO_3^{2-}, Mg-Al-Cl^- and Mg-Al-NO_3^- and (b) Magnified of (a) showing shift towards lower 2θ for 003 reflections and increase in d spacing with anion exchange.

An essential aspect of implementing LDHs as anion conductors in the temperature range of 100-250 °C is understanding the structural and chemical changes in this temperature range. As discussed earlier, the ion conductivity in LDHs is a consequence of the hydroxyl

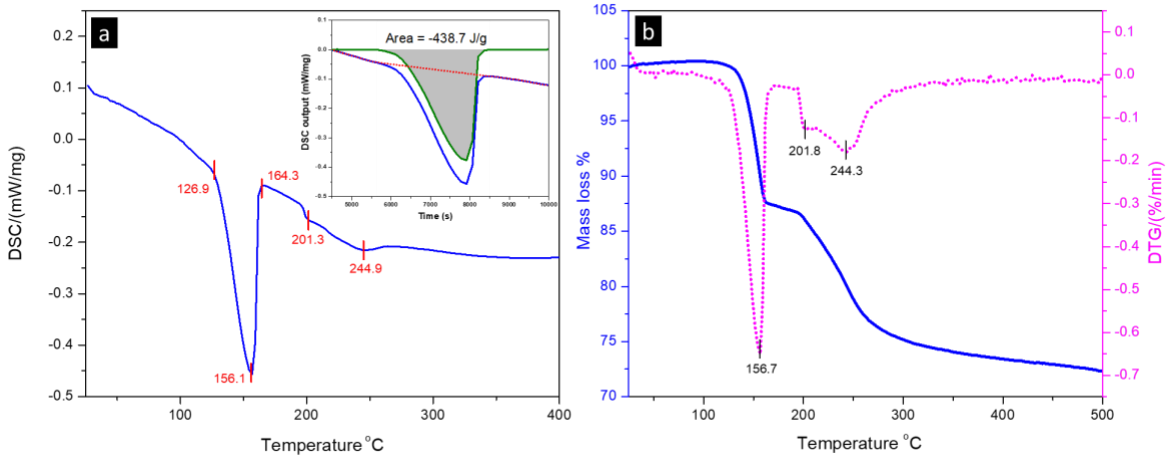

Figure 5.8. (a) Differential scanning calorimetry of Zn-Al-CO_3^{2-} (b) TGA and DTG of Zn-Al-CO_3^{2-}

ion network in the 2D host layer and its hydrogen bonding with the neighboring water molecules. Therefore, the presence of interlayer water helps in the ion conductivity of bulk LDH. The amount and the temperature at which interlayer water is lost is a function of host layer composition, the interlayer anion, and relative humidity. We have performed DSC-TGA in the air to study the loss of water and the enthalpy associated with it for different LDHs (Figures 5.9 and 5.10).

The water loss in Zn-Al Carbonate LDH happens between 126.9 °C to 164.3 °C, followed by decarbonation and dehydroxylation at 201.3 °C and 244.9 °C. In the case of Mg-Al LDH, the water loss occurs at a higher temperature range 151.9 °C to 191.6 °C, followed by decarbonation and dehydroxylation at 272.7 °C and 389.4 °C, respectively. These transitions are also observed in TGA, and mass loss associated with loss of water, carbonate and hydroxyl ions occurs with increasing temperature. The enthalpy associated with the interlayer water loss is -438.7 J/g and -388.9 J/g for Zn-Al LDH and Mg-Al LDH, respectively. We aim to compare the water loss temperature for LDHs with different

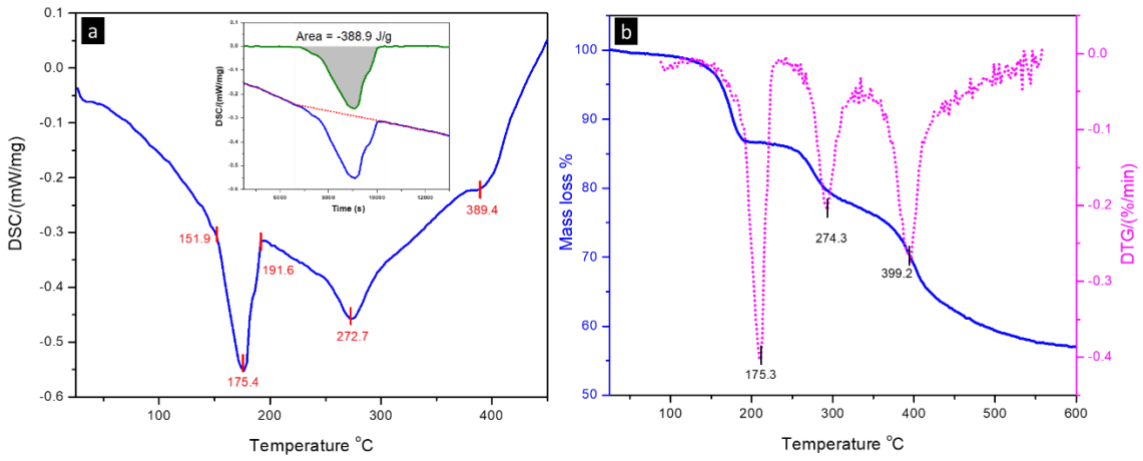

Figure 5.10. (a) Differential scanning calorimetry of Mg-Al-CO_3^{2-} (b) TGA and DTG of Mg-Al-CO_3^{2-}

interlayer anions to understand the effect of interlayer anion on water retention and conductivity. Water retention at temperatures greater than 100 °C is promising for application of these LDHs in alkaline fuel cells.

For bulk ion conductivity measurement performed on Fuel cell station 850, LDH samples were prepared in two forms – a film on hydrophilic carbon paper and a pellet pressed between carbon paper. The film was prepared as described by Xu *et al*[35] using transfer method. A LDH film was prepared on a filter paper by filtration and then transferred onto hydrophilic carbon. However, short-circuiting was observed during measurement in the fuel cell setup. Therefore, a thicker LDH system in the form of a pellet was used for measurements. Figure 5.11 shows cross-sectional SEM of the pellet with thickness variation across the length. This pellet was pressed between graphite electrodes in the

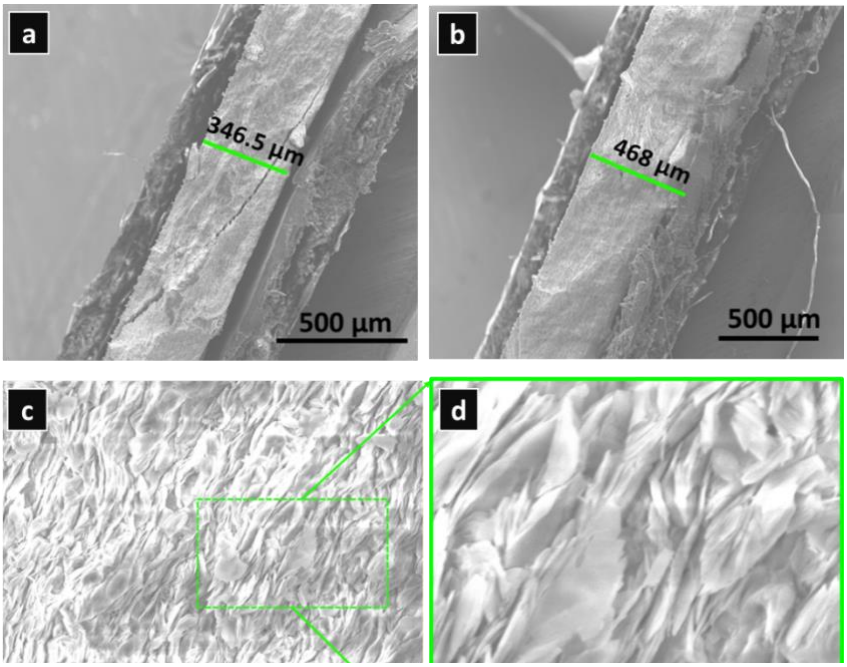

Figure 5.11. Cross-sectional SEM of LDH pellet used for ion conductivity measurement. (a) and (b) show two ends of the pellet with thickness 346.5 µm and 468 µm, respectively. (c) magnified image of pellet and (d) magnified image of (c) showing most platelets are parallel to each other.

measurement cell, as shown in Figure 5.12a. Room temperature measurement at 100 % RH on the pellet (Figure 5.12) gives a conductivity value of 0.47 x 10^{-6} S/cm. This value is comparable to the earlier values on Mg-Al-CO_3^{2-} in the literature[19].

Higher temperature measurements on the same pellet were not reproducible between different runs. Several improvements are required in the system to ensure reproducibility of the measurement – (a) thermal insulation of the setup needs to be improved to prevent significant heat loss during the measurement. We propose using a thermal insulation jacket around the fuel cell. (b) Another observation that needs to be addressed is that the pellet breaks and fills the serpentine grooves of the fuel cell. A graphite electrode without grooves but just a depression to hold the pellet may be better suited to avoid effects of pellet disintegration on the measurement. And (c), as shown in Figure 5.11, a significant fraction of the platelets is parallel to each other and the carbon electrode. This implies that the ion conduction path is cross-planar. An in-plane conduction

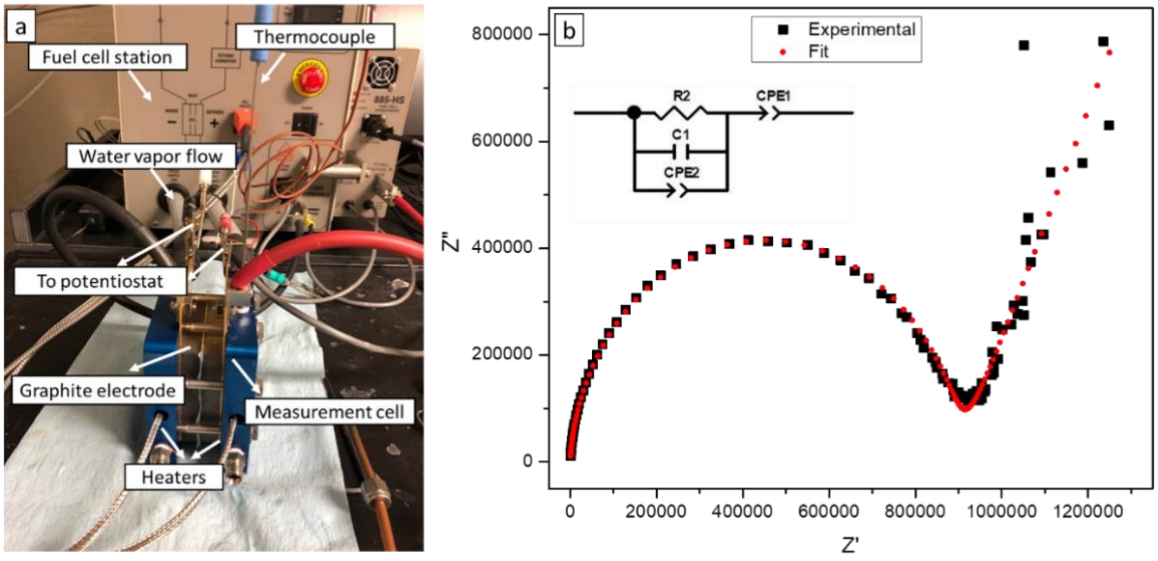

Figure 5.12. (a) Fuel cell testing station set up for ion conductivity measurements. (b) Nyquist plot at 25 °C – experimental and fit using the circuit shown in inset.

path will be more favorable for application in devices due to high in-plane ion conductivity. Therefore, synthesis approaches that provide in-plane platelet orientation perpendicular to the electrode need to be explored. Composite membranes of LDH and polymer have been proposed in the literature to grow oriented LDH for electrochemical cells[17,36]. A compatible system needs to be identified for this study and further incorporation in fuel cells.

5.4 Conclusion

This study aims to provide insight into the feasibility of LDHs as anion conductors in electrochemical systems operating in the intermediate temperature range of 100-250 °C. We have synthesized and characterized Mg-Al and Zn-Al LDH with different interlayer anions to study their structural, thermochemical properties and their impact on ionic conductivity for application in electrochemical systems.

Reflux and hydrothermal synthesis methods were used for the synthesis of Zn-Al and Mg-Al carbonate LDH, respectively. XRD and SEM indicate the formation of crystalline LDHs with a hexagonal crystal system. The carbonate LDHs were anion exchanged using salt-acid treatment to obtain chloride intercalated LDHs, showing an increase in the interlayer spacing. The interlayer spacing increases further on exchanging chloride with nitrate anion. DSC-TGA studies on the carbonate Zn-Al and Mg-Al LDH show interlayer water loss (dehydration) peak at 156.1 °C and 175.4 °C respectively, providing promising conditions for ionic conductivity the range of 100-200 °C. We have used a Fuel cell station for measuring the ion conductivity of LDHs at controlled temperature and humidity. Room temperature measurements on bulk LDH (as pellets) have shown a value of 0.47×10^{-6} S/cm, comparable to literature studies. Further improvements are required in the setup to prevent heat loss at higher temperatures. In addition, the orientation of LDH platelets in

bulk pellet or as a polymer composite needs to be optimized to utilize high in-plane conductivity.

5.5 References

(1) Karim, M. R.; Hatakeyama, K.; Matsui, T.; Takehira, H.; Taniguchi, T.; Koinuma, M.; Matsumoto, Y.; Akutagawa, T.; Nakamura, T.; Noro, S. I.; Yamada, T.; Kitagawa, H.; Hayami, S. Graphene Oxide Nanosheet with High Proton Conductivity. *J. Am. Chem. Soc.* **2013**, *135* (22), 8097–8100. https://doi.org/10.1021/JA401060Q/SUPPL_FILE/JA401060Q_SI_001.PDF.

(2) Hatakeyama, K.; Karim, M. R.; Ogata, C.; Tateishi, H.; Funatsu, A.; Taniguchi, T.; Koinuma, M.; Hayami, S.; Matsumoto, Y. Proton Conductivities of Graphene Oxide Nanosheets: Single, Multilayer, and Modified Nanosheets. *Angew. Chemie* **2014**, *126* (27), 7117–7120. https://doi.org/10.1002/ANGE.201309931.

(3) Raidongia, K.; Huang, J. Nanofluidic Ion Transport through Reconstructed Layered Materials. *J. Am. Chem. Soc.* **2012**, *134* (40), 16528–16531. https://doi.org/10.1021/JA308167F/SUPPL_FILE/JA308167F_SI_001.PDF.

(4) Shao, J. J.; Raidongia, K.; Koltonow, A. R.; Huang, J. Self-Assembled Two-Dimensional Nanofluidic Proton Channels with High Thermal Stability. *Nat. Commun. 2015 61* **2015**, *6* (1), 1–7. https://doi.org/10.1038/ncomms8602.

(5) Madauß, L.; Foller, T.; Plaß, J.; Kumar, P. V.; Musso, T.; Dunkhorst, K.; Joshi, R.; Schleberger, M. Selective Proton Transport for Hydrogen Production Using Graphene Oxide Membranes. *J. Phys. Chem. Lett.* **2020**, *11*, 9415–9420. https://doi.org/10.1021/ACS.JPCLETT.0C02481/SUPPL_FILE/JZ0C02481_SI_001.PDF.

(6) Fukuda, M.; Islam, M. S.; Shudo, Y.; Yagyu, J.; Lindoy, L. F.; Hayami, S. Ion Conduction Switching between H + and OH − Induced by PH in Graphene Oxide. *Chem. Commun.* **2020**, *56* (31), 4364–4367. https://doi.org/10.1039/D0CC00769B.

(7) Tadanaga, K.; Furukawa, Y.; Hayashi, A.; Tatsumisago, M. Direct Ethanol Fuel Cell Using

Hydrotalcite Clay as a Hydroxide Ion Conductive Electrolyte. *Adv. Mater.* **2010**, *22* (39), 4401–4404. https://doi.org/10.1002/ADMA.201001766.

(8) Kubo, D.; Tadanaga, K.; Hayashi, A.; Tatsumisago, M. Improvement of Electrochemical Performance in Alkaline Fuel Cell by Hydroxide Ion Conducting Ni–Al Layered Double Hydroxide. *J. Power Sources* **2013**, *222*, 493–497. https://doi.org/10.1016/J.JPOWSOUR.2012.08.093.

(9) Lohmann-Richters, F. P.; Müller, M.; Carmo, M. Communication—Layered Double Hydroxide as Intermediate-Temperature Electrolyte for Efficient Water Splitting. *J. Electrochem. Soc.* **2020**, *167* (8), 084512. https://doi.org/10.1149/1945-7111/AB8E80.

(10) Miyazaki, K.; Asada, Y.; Fukutsuka, T.; Abe, T.; Bendersky, L. A. Structural Insights into Ion Conduction of Layered Double Hydroxides with Various Proportions of Trivalent Cations. *J. Mater. Chem. A* **2013**, *1* (46), 14569–14576. https://doi.org/10.1039/C3TA13632A.

(11) Furukawa, Y.; Tadanaga, K.; Hayashi, A.; Tatsumisago, M. Evaluation of Ionic Conductivity for Mg–Al Layered Double Hydroxide Intercalated with Inorganic Anions. *Solid State Ionics* **2011**, *192* (1), 185–187. https://doi.org/10.1016/J.SSI.2010.05.032.

(12) Tamaki, T.; Nakanishi, N.; Ohashi, H.; Yamaguchi, T. The Effect of Particle Size and Surface Area on the Ion Conductivity of Layered Double Hydroxide. *Electrochem. commun.* **2012**, *25* (1), 50–53. https://doi.org/10.1016/j.elecom.2012.09.003.

(13) Zeng, L.; Zhao, T. S. Integrated Inorganic Membrane Electrode Assembly with Layered Double Hydroxides as Ionic Conductors for Anion Exchange Membrane Water Electrolysis. *Nano Energy* **2015**, *11*, 110–118. https://doi.org/10.1016/j.nanoen.2014.10.019.

(14) Chen, N.; Long, C.; Li, Y.; Wang, D.; Zhu, H. High-Performance Layered Double Hydroxide/Poly(2,6-Dimethyl-1,4-Phenylene Oxide) Membrane with Porous Sandwich Structure for Anion Exchange Membrane Fuel Cell Applications. *J. Memb. Sci.* **2018**, *552*, 51–60. https://doi.org/10.1016/J.MEMSCI.2018.01.045.

(15) He, X.; Cao, L.; He, G.; Zhao, A.; Mao, X.; Huang, T.; Li, Y.; Wu, H.; Sun, J.; Jiang, Z. A Highly Conductive and Robust Anion Conductor Obtained: Via Synergistic Manipulation in

Intra- and Inter-Laminate of Layered Double Hydroxide Nanosheets. *J. Mater. Chem. A* **2018**, *6* (22), 10277–10285. https://doi.org/10.1039/c8ta02193g.

(16) Perez-Page, M.; Sahoo, M.; Holmes, S. M. Single Layer 2D Crystals for Electrochemical Applications of Ion Exchange Membranes and Hydrogen Evolution Catalysts. *Adv. Mater. Interfaces* **2019**, *6* (7), 1801838. https://doi.org/10.1002/ADMI.201801838.

(17) Wan, L.; Xu, Z.; Wang, B. Green Preparation of Highly Alkali-Resistant PTFE Composite Membranes for Advanced Alkaline Water Electrolysis. *Chem. Eng. J.* **2021**, *426*, 131340. https://doi.org/10.1016/J.CEJ.2021.131340.

(18) Sun, P.; Chen, F.; Zhou, W.; Liu, X.; Ma, R.; Sasaki, T. Superionic Conduction along Ordered Hydroxyl Networks in Molecular-Thin Nanosheets. *Mater. Horizons* **2019**, *6* (10), 2087–2093. https://doi.org/10.1039/c9mh00549h.

(19) Kim, H. S.; Yamazaki, Y.; Kim, J. D.; Kudo, T.; Honma, I. High Ionic Conductivity of Mg-Al Layered Double Hydroxides at Intermediate Temperature (100-200°C) under Saturated Humidity Condition (100% RH). *Solid State Ionics* **2010**, *181* (19–20), 883–888. https://doi.org/10.1016/j.ssi.2010.04.037.

(20) Deng, X.; Huang, J.; Wan, H.; Chen, F.; Lin, Y.; Xu, X.; Ma, R.; Sasaki, T. Recent Progress in Functionalized Layered Double Hydroxides and Their Application in Efficient Electrocatalytic Water Oxidation. *Journal of Energy Chemistry*. Elsevier B.V. May 1, 2019, pp 93–104. https://doi.org/10.1016/j.jechem.2018.07.007.

(21) Sun, P.; Ma, R.; Bai, X.; Wang, K.; Zhu, H.; Sasaki, T. Single-Layer Nanosheets with Exceptionally High and Anisotropic Hydroxyl Ion Conductivity. *Sci. Adv.* **2017**, *3* (4), e1602629. https://doi.org/10.1126/sciadv.1602629.

(22) Xiong, P.; Sun, B.; Sakai, N.; Ma, R.; Sasaki, T.; Wang, S.; Zhang, J.; Wang, G. 2D Superlattices for Efficient Energy Storage and Conversion. *Adv. Mater.* **2020**, *32* (18), 1902654. https://doi.org/10.1002/ADMA.201902654.

(23) Tadanaga, K.; Furukawa, Y.; Hayashi, A.; Tatsumisago, M. Effect of Mg/Al Ratio on Hydroxide Ion Conductivity for Mg–Al Layered Double Hydroxide and Application to Direct

Ethanol Fuel Cells. *J. Electrochem. Soc.* **2012**, *159* (4), B368–B370. https://doi.org/10.1149/2.007204JES/XML.

(24) Shi, L.; Ying, Z.; Xu, A.; Cheng, Y. Unraveling the Hydroxide Ion Transportation Mechanism along the Surface of Two-Dimensional Layered Double Hydroxide Nanosheets. *J. Phys. Chem. C* **2021**, *125* (2), 1240–1248. https://doi.org/10.1021/acs.jpcc.0c09517.

(25) Zhaoping Liu; Renzhi Ma; Yasuo Ebina; Nobuo Iyi; Kazunori Takada, and; Sasaki*, T. General Synthesis and Delamination of Highly Crystalline Transition-Metal-Bearing Layered Double Hydroxides. *Langmuir* **2006**, *23* (2), 861–867. https://doi.org/10.1021/LA062345M.

(26) Li, L.; Ma, R.; Ebina, Y.; Iyi, N.; Sasaki, T. Positively Charged Nanosheets Derived via Total Delamination of Layered Double Hydroxides. *Chem. Mater.* **2005**, *17* (17), 4386–4391. https://doi.org/10.1021/cm0510460.

(27) Bish, D. L. Anion-Exchange in Takovite : Applications to Other Hydroxide Minerals. *Bull. Minéralogie* **1980**, *103* (2), 170–175. https://doi.org/10.3406/BULMI.1980.7392.

(28) Costantino, U.; Marmottini, F.; Nocchetti, M.; Vivani, R. New Synthetic Routes to Hydrotalcite-like Compounds - Characterisation and Properties of the Obtained Materials. *Eur. J. Inorg. Chem.* **1998**, No. 10, 1439–1446. https://doi.org/10.1002/(sici)1099-0682(199810)1998:10<1439::aid-ejic1439>3.0.co;2-1.

(29) Miyata, S. THE SYNTHESES OF HYDROTALCITE-LIKE COMPOUNDS AND THEIR STRUCTURES AND PHYSICO-CHEMICAL PROPERTIES I: THE SYSTEMS MgZ+-A13+-NO3, MgZ+-A13+-C1-, Mg 2 +-A13 +-ClOg, Ni 2 +-A13 +-C1-AND Zn 2 +-A13 +-C1. *Clays Clay Miner.* **1975**, *23*, 369–375.

(30) Hibino, T.; Yamashita, Y.; Kosuge, K.; Tsunashima, A. Decarbonation Behavior of Mg-Al-CO3 Hydrotalcite-like Compounds during Heat Treatment. *Clays Clay Miner. 1995 434* **1995**, *43* (4), 427–432. https://doi.org/10.1346/CCMN.1995.0430405.

(31) Iyi, N.; Sasaki, T. Deintercalation of Carbonate Ions and Anion Exchange of an Al-Rich MgAl-LDH (Layered Double Hydroxide). *Appl. Clay Sci.* **2008**, *42* (1–2), 246–251. https://doi.org/10.1016/J.CLAY.2008.01.016.

(32) Liu, Z.; Ma, R.; Osada, M.; Iyi, N.; Ebina, Y.; Takada, K.; Sasaki, T. Synthesis, Anion Exchange, and Delamination of Co-Al Layered Double Hydroxide: Assembly of the Exfoliated Nanosheet/Polyanion Composite Films and Magneto-Optical Studies. *J. Am. Chem. Soc.* **2006**, *128* (14), 4872–4880. https://doi.org/10.1021/ja0584471.

(33) Sahoo, P.; Ishihara, S.; Yamada, K.; Deguchi, K.; Ohki, S.; Tansho, M.; Shimizu, T.; Eisaku, N.; Sasai, R.; Labuta, J.; Ishikawa, D.; Hill, J. P.; Ariga, K.; Bastakoti, B. P.; Yamauchi, Y.; Iyi, N. Rapid Exchange between Atmospheric CO2 and Carbonate Anion Intercalated within Magnesium Rich Layered Double Hydroxide. *ACS Appl. Mater. Interfaces* **2014**, *6* (20), 18352–18359. https://doi.org/10.1021/AM5060405.

(34) Iyi, N.; Matsumoto, T.; Kaneko, Y.; Kitamura, K. Deintercalation of Carbonate Ions from a Hydrotalcite-like Compound: Enhanced Decarbonation Using Acid-Salt Mixed Solution. *Chem. Mater.* **2004**, *16* (15), 2926–2932. https://doi.org/10.1021/cm049579g.

(35) Zhu, H.; Huang, S.; Yang, Z.; Liu, T. Oriented Printable Layered Double Hydroxide Thin Films via Facile Filtration. *J. Mater. Chem.* **2011**, *21* (9), 2950–2956. https://doi.org/10.1039/C0JM03317K.

(36) Sun, P.; Ma, R.; Sasaki, T. Recent Progress on Exploring Exceptionally High and Anisotropic H+/OH- Ion Conduction in Two-Dimensional Materials. *Chemical Science*. Royal Society of Chemistry December 20, 2017, pp 33–43. https://doi.org/10.1039/c7sc04019a.

CHAPTER 6 – Conclusions and Perspective

6.1 3D Nanostructured material design in the sub-100 nm regime using silica colloidal crystal and high-pressure chemical vapor deposition

HPCVD infiltration of silica colloidal crystals provides a versatile strategy to synthesize 3D interconnected nanostructures of semiconductors and metals, defined as metalattices in this dissertation[1–6]. The structural repeat distance in metalattices is comparable to the characteristic length scale of the intrinsic physical phenomenon in the material, leading to the interaction between structural periodicity and the corresponding physical phenomenon.

In chapter 2, a core-shell-based chemical passivation strategy for Ge metalattice and its structural and electronic properties are discussed. The core-shell approach prevents oxidation of Ge core, and the oxide-free Ge core shows evidence of quantum confinement[1]. Based on these findings, we suggested two parameters for tuning the electronic structure of Ge metalattices – void size in the template and interdiffusion between core and shell. The core-shell metalattice is also being explored for semiconductor-based EUV plasmonics.[5]

Although the semiconductor metalattice exhibits a quantum confinement effect and is interconnected, a parallel study of Si metalattices showed that the semiconducting and metallic transport properties expected in doped and confined nanocrystals are not observed in metalattices[7]. This low conductivity may be attributed to the presence of grain boundaries and defects in infiltrated Si, surface traps at the Si-SiO_2 interface, a non-uniform dopant distribution, and disorder in the superlattice structure. One possible approach to improving the transport properties is to synthesize single-crystalline metalattices. This can be achieved by controlled laser annealing through a single crystal substrate to propagate single crystal growth into the polycrystalline metalattice. Laser

annealing has led to the formation of single-crystalline semiconductors in silica fibers in earlier studies[8,9]. Another way to achieve single-crystalline metalattices is through epitaxial growth during HPCVD. Surface modification of the metalattice can also help in reducing the surface traps, as seen in other semiconductor nanocrystals/thin films.[10–12]

The thermal and magnetic behavior of metalattices in the current structure have shown promising results. Ferromagnetic Ni metalattices show the presence of topological magnetic monopoles originating from magnetic frustration in the 3D curved surfaces of the metalattice.[13] The size-dependent variation in metalattice structure/curvature can in principle be used to tune the interactions between these magnetic monopoles and to design them for potential applications in magnetic storage devices. Thermal studies on Si metalattices made from different size templates (14 nm to 120 nm) have shown a very low thermal conductivity with a value of 1 W/m/K[14]. Computational studies indicate that this can be lowered further to 0.16 W/m/K by reducing silica template size to 5 nm. Another finding derived from that study is that a graded structure of Si metalattice comprised of different size silica particles arranged in parallel layers along z-direction can enable thermal rectification in this structure[15]. Thus, by varying the porosity of Si metalattices and their lattice spacing, heat transport in semiconductor materials can potentially be tuned in unique ways.

These studies have shown that the structure of metalattices, i.e., their void size, local and long-range order, has an impact on their physical properties. Since metalattices inherit the template structure, we investigated the detailed structure of silica nanoparticle templates using SAXS and SEM (Chapter 3). We found that particles less than 32 nm in diameter assemble in a body-centered cubic structure, and larger particles assemble in a random close packed structure along with a 2D hexatic phase. This structure and order are maintained in the inverse structures obtained by infiltrating these templates by using

HPCVD. This size-based structural variation can be attributed to shear force during assembly and to size dispersity in the silica nanoparticles. More investigation is needed to understand the contributions and interplay of different factors such as particle non-covalent interactions, size dispersity, and capillary and gravitational forces during the assembly process on the resulting template structure. A detailed understanding of the underlying factors driving particle assembly can also help in tuning the 3D arrangement of the particles. Different 3D arrangements of particles will introduce variations in symmetry, porosity, and structure of the metalattices, thereby potentially enabling tuning of their properties.

Grain boundaries and disorder in the templates propagate to the metalattices and affect their properties, as observed in the case of electronic transport. Reducing particle dispersity synthetically or by fractionalization of particles post-synthesis can help in improving the quality of colloidal crystals. Optimization of the deposition process and surface modification of the substrate has been shown to decrease the density of cracks and grain boundaries in the deposited film,[16,17] and this strategy could be implemented for silica nanoparticle system.

6.2 Synthesis and characterization of layered double hydroxides

Layered double hydroxides in all three of their forms - bulk, intercalated, and nanosheets - have garnered a lot of attention for applications in catalysis and energy storage devices. One of their characteristic properties is hydroxide ion conductivity, which is comparable to proton conductivity in ionomer-based systems[18]. This makes inorganic LDHs, which are stable at high temperatures and in an alkaline environment, promising candidates for anionic conduction in electrochemical systems at intermediate temperatures (100-250 °C)

In this dissertation, we synthesized and characterized the structural, thermochemical, and ionic conduction properties of LDHs in order to understand their fundamental behavior for applications as anionic conductors in electrochemical systems operating between 100-250 °C (chapter 5). We synthesized nine different types of crystalline layered double hydroxides by varying the M^{2+} ion (Co-Al, Mg-Al, Zn-Al) and the interlayer anions (carbonate, chloride, and nitrate). The ion exchange method was used to convert as-synthesized LDH containing carbonate anions to LDH with chloride and nitrate interlayer anions. Variations in the M^{2+} ion and the interlayer anion change the interlayer spacing, the content of interlayer water, and the enthalpy/free energy associated with desorption of interlayer water, thus affecting the ion conductivity of LDHs. We used DSC-TGA to study their thermochemical behavior and determine the enthalpy of water desorption. Future work will include comparing the thermal behavior and free energy of water desorption of different LDHs in order to establish a correlation between the composition and retention of water at intermediate temperatures. This may enable us to identify LDH compositions that function well under electrochemical device conditions. Ionic conductivity measurements using the Scribner fuel cell station need to be optimized further to reduce thermal loss, improve measurement reproducibility and measure conductivity across different LDH orientations.

In addition to identifying the composition of LDHs for anion conduction, their orientation in the device is also essential to maximize the in-plane conduction. This can be achieved by synergistic work on synthesizing oriented LDH samples[19,20] and by measuring their corresponding anisotropic ionic conductivity. The optimized composition and orientation of LDH will be implemented in bipolar membranes and/or ion-selective conductors in redox flow batteries, electrolysers, and fuel cells that operate in alkaline environments.

6.3 References

(1) Mahale, P.; Moradifar, P.; Cheng, H. Y.; Nova, N. N.; Grede, A. J.; Lee, B.; De Jesús, L. R.; Wetherington, M.; Giebink, N. C.; Badding, J. V.; Alem, N.; Mallouk, T. E. Oxide-Free Three-Dimensional Germanium/Silicon Core–Shell Metalattice Made by High-Pressure Confined Chemical Vapor Deposition. *ACS Nano* **2020**.

(2) Chen, W.; Talreja, D.; Eichfeld, D.; Mahale, P.; Nova, N. N.; Cheng, H. Y.; Russell, J. L.; Yu, S.-Y.; Poilvert, N.; Mahan, G.; Mohney, S. E.; Crespi, V. H.; Mallouk, T. E.; Badding, J. V.; Foley, B.; Gopalan, V.; Dabo, I. Achieving Minimal Heat Conductivity by Ballistic Confinement in Phononic Metalattices. *ACS Nano* **2020**.

(3) Chen, Y.; Liu, Y.; Moradifar, P.; Glaid, A. J.; Russell, J. L.; Mahale, P.; Yu, S.-Y.; Culp, T. E.; Kumar, M.; Gomez, E. D.; Mohney, S. E.; Mallouk, T. E.; Alem, N.; Badding, J. V.; Liu, Y. Quantum Transport in Three-Dimensional Metalattices of Platinum Featuring an Unprecedentedly Large Surface Area to Volume Ratio. *Phys. Rev. Mater.* **2020**, *4* (3), 035201.

(4) Liu, Y.; Kempinger, S.; He, R.; Day, T. D.; Moradifar, P.; Yu, S. Y.; Russell, J. L.; Torres, V. M.; Xu, P.; Mallouk, T. E.; Mohney, S. E.; Alem, N.; Samarth, N.; Badding, J. V. Confined Chemical Fluid Deposition of Ferromagnetic Metalattices. *Nano Lett.* **2018**, *18* (1), 546–552.

(5) Moradifar, P.; Kang, L.; Mahale, P.; Liu, Y.; Nova, N. N.; Glaid, A.; Mallouk, T. E.; Badding, J.; Werner, D.; Alem, N. Plasmonic Metalattices: A Correlated Monochromated Electron Energy Loss Study and Theoretical Calculations. *Microsc. Microanal.* **2019**, *25* (S2), 678–679.

(6) Abad Mayor, B.; Knobloch, J. L.; Frazer, T. D.; Hernandez-Charpak, J. N.; Cheng, H. Y.; Grede, A. J.; Giebink, N. C.; Mallouk, T. E.; Mahale, P.; Nova, N. N.; Tomaschke, A. A.; Ferguson, V. L.; Crespi, V. H.; Gopalan, V.; Kapteyn, H. C.; Badding, J. V.; Murnane, M. M. Nondestructive Measurements of the Mechanical and Structural Properties of Nanostructured Metalattices. *Nano Lett.* **2020**.

(7) Yixuan Chen, Electronic localization in 3D silicon and platinum metalattices and

magnetoelectrical transport properties of Dirac nodal line semimetal ZrSiS, The Pennsylvania State University, University park, 2020

(8) Healy, N.; Mailis, S.; Bulgakova, N. M.; Sazio, P. J. A.; Day, T. D.; Sparks, J. R.; Cheng, H. Y.; Badding, J. V.; Peacock, A. C. Extreme Electronic Bandgap Modification in Laser-Crystallized Silicon Optical Fibres. *Nat. Mater. 2014 1312* **2014**, *13* (12), 1122–1127.

(9) Ji, X.; Page, R. L.; Chaudhuri, S.; Liu, W.; Yu, S. Y.; Mohney, S. E.; Badding, J. V.; Gopalan, V. Single-Crystal Germanium Core Optoelectronic Fibers. *Adv. Opt. Mater.* **2017**, *5* (1), 1600592.

(10) Vilan, A.; Cahen, D. Chemical Modification of Semiconductor Surfaces for Molecular Electronics. *Chem. Rev.* **2017**, *117* (5), 4624–4666.

(11) Zhang, H.; Hu, B.; Sun, L.; Hovden, R.; Wise, F. W.; Muller, D. A.; Robinson, R. D. Surfactant Ligand Removal and Rational Fabrication of Inorganically Connected Quantum Dots. *Nano Lett.* **2011**, *11* (12), 5356–5361.

(12) Talapin, D. V.; Lee, J. S.; Kovalenko, M. V.; Shevchenko, E. V. Prospects of Colloidal Nanocrystals for Electronic and Optoelectronic Applications. *Chem. Rev.* **2010**, *110* (1),

(13) Rana, A.; Liao, C.; Iacocca, E.; Zou, J.; Pham, M.; Lu, X. Creation and Observation of Topological Magnetic Monopoles and Their Interactions in a Ferromagnetic Meta-Lattice. Submitted, 2021.

(14) Chen, W.; Talreja, D.; Eichfeld, D.; Mahale, P.; Nova, N. N.; Cheng, H. Y.; Russell, J. L.; Yu, S.-Y.; Poilvert, N.; Mahan, G.; Mohney, S. E.; Crespi, V. H.; Mallouk, T. E.; Badding, J. V.; Foley, B.; Gopalan, V.; Dabo, I. Achieving Minimal Heat Conductivity by Ballistic Confinement in Phononic Metalattices. *ACS Nano* **2020**, acsnano.9b09487.

(15) Disha Talreja, Time-Domain Thermoreflectance Probing of Tunable Thermal Transport in Silicon Metalattices, PhD dissertation, The Pennsylvania State University, University Park, 2020

(16) Jiang, Z.; Hsain, Z.; Pikul, J. H. Thick Free-Standing Metallic Inverse Opals Enabled by New Insights into the Fracture of Drying Particle Films. *Langmuir* **2020**, *36* (26), 7315–7324.

(17) Jiang, Z.; Pikul, J. H. Centimetre-Scale Crack-Free Self-Assembly for Ultra-High Tensile Strength Metallic Nanolattices. *Nat. Mater. 2021 2011* **2021**, *20* (11), 1512–1518.

(18) Sun, P.; Ma, R.; Bai, X.; Wang, K.; Zhu, H.; Sasaki, T. Single-Layer Nanosheets with Exceptionally High and Anisotropic Hydroxyl Ion Conductivity. *Sci. Adv.* **2017**, *3* (4), e1602629.

(19) Sun, P.; Ma, R.; Sasaki, T. Recent Progress on Exploring Exceptionally High and Anisotropic H+/OH- Ion Conduction in Two-Dimensional Materials. *Chemical Science*. Royal Society of Chemistry December 20, 2017, pp 33–43.

(20) Wan, L.; Xu, Z.; Wang, B. Green Preparation of Highly Alkali-Resistant PTFE Composite Membranes for Advanced Alkaline Water Electrolysis. *Chem. Eng. J.* **2021**, *426*, 131340.

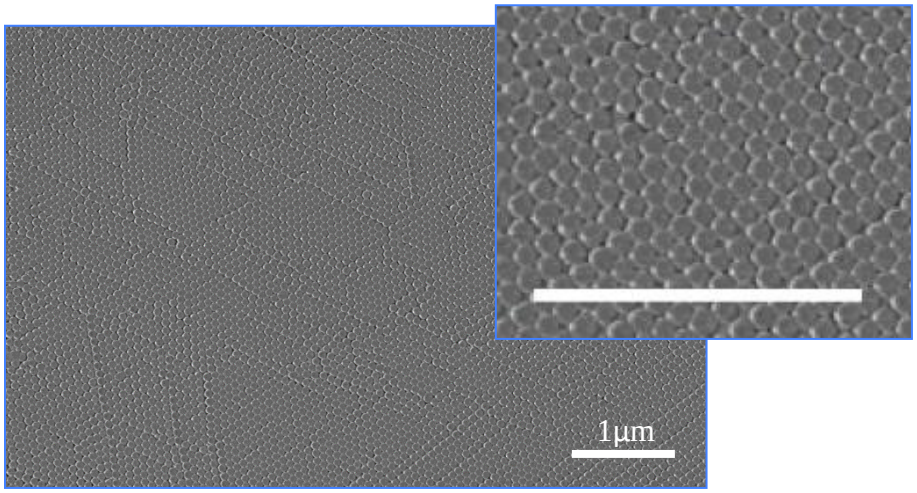

Figure A.1. Top view SEM image of the silica template used for the synthesis of core-shell metalattice. Scale bar in the magnified inset image is 1 µm.

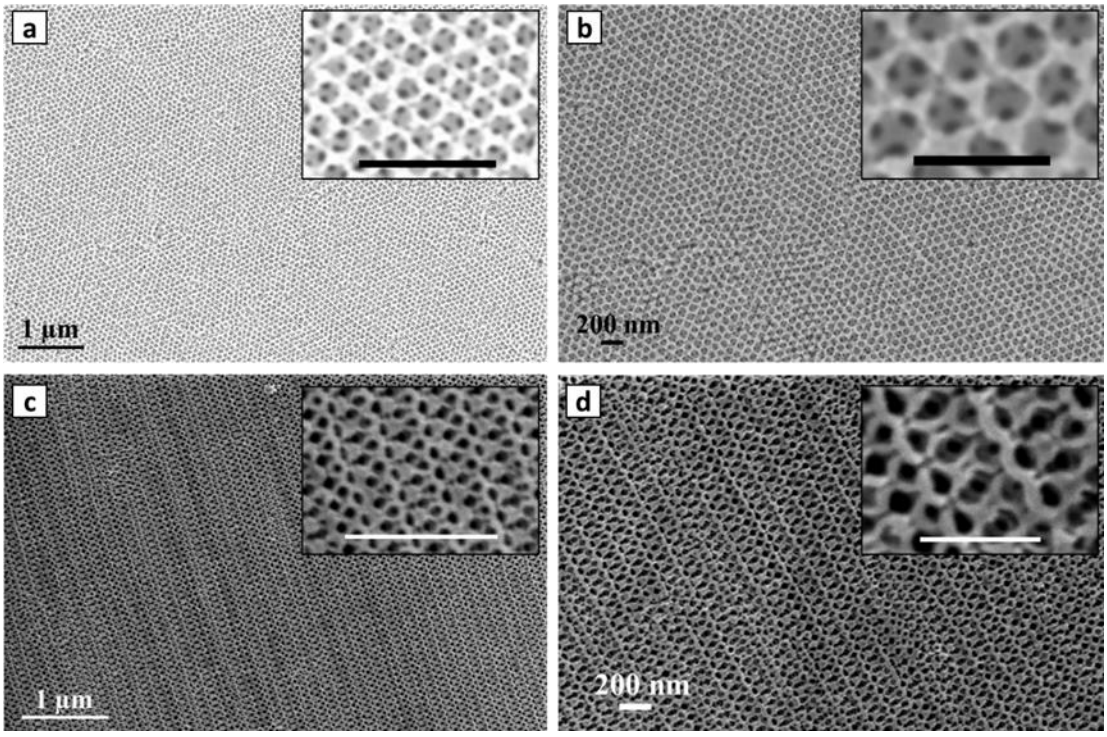

Figure A.2. Ge metalattice from a 60 nm silica sphere template at different magnifications (a) and (b). Ge-Si core-shell metalattice at different magnifications (c) and (d). Inset scale bar is 250, 200, 500 and 200 nm for a,b,c and d respectively.

A3(a)

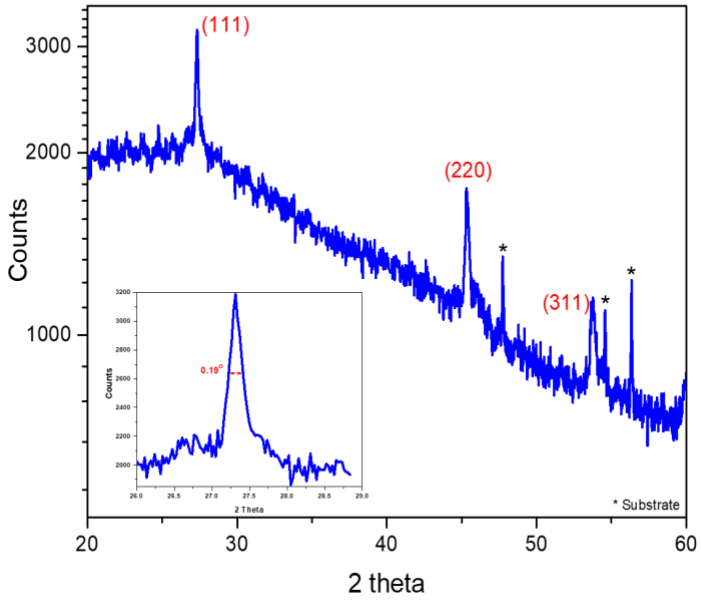

A3(b)

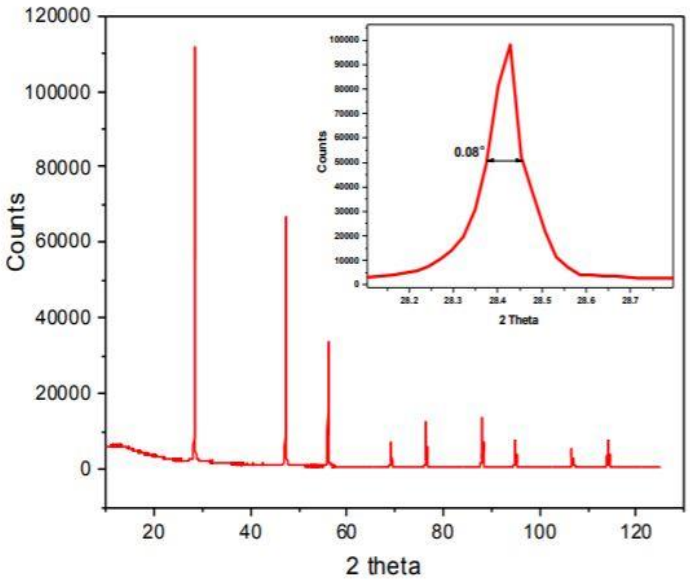

Figure A.3. (a) X-ray diffraction (CuKα, λ = 1.5418 Å) of the core-shell metalattice film. The inset shows width of the Ge (111) peak after stripping the Kα2 component of the reflection. (b) X-ray diffraction of a crystalline Si standard with inset showing the width of the Kα2 stripped (111) peak to determine the instrumental line broadening.

Calculation of the Ge crystalline domain size using the Scherrer formula[1] –

Ge (111) FWHM = 0.19°

Si (111) FWHM = 0.08° (instrumental line width)

λ = 1.5418 Å = 0.15418 nm

Deconvoluted Ge (111) FWHM = $(0.19^2 - 0.08^2)^{½}$ = 0.17° = 3.01 x 10^{-3} radians

Crystal domain size: $t = \frac{0.9\lambda}{FWHM \cdot \cos\theta} \approx 47$ nm

1. Patterson, A. "The Scherrer Formula for X-Ray Particle Size Determination". *Phys.*

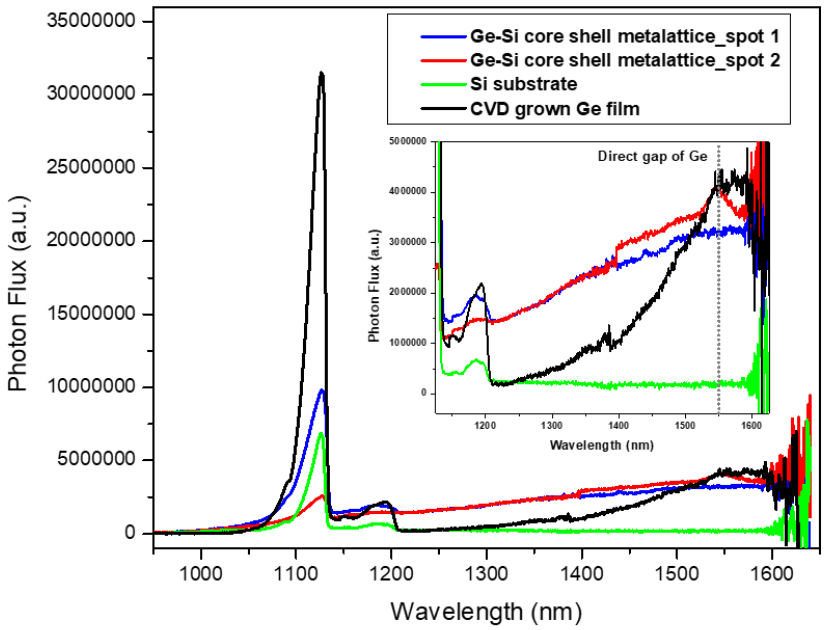

Figure A.4. Photoluminescence spectra of a core-shell metalattice at two different spots on the sample, a CVD-grown Ge film, and the Si substrate. The inset shows a magnified view of the region to the blue of the Ge bulk band gap energy.

Rev. **1939**, *56*, 978–982.

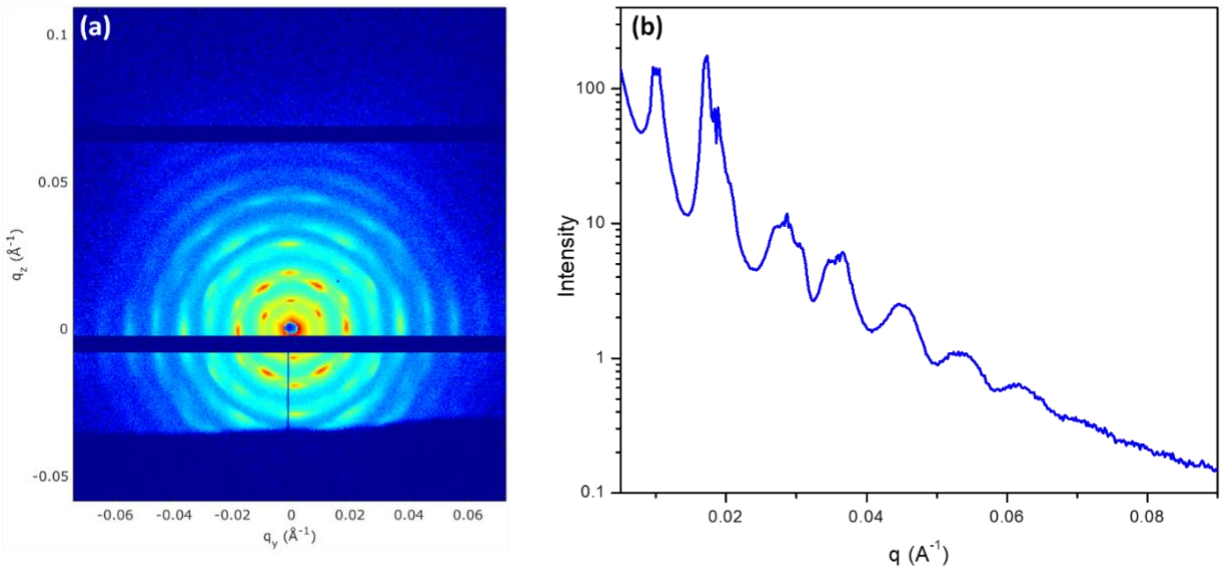

Figure A.5. (a) Synchrotron 2D SAXS pattern for a-Ge metalattice after template removal and before shell infiltration (b) 1D Azimuthal average of (a).

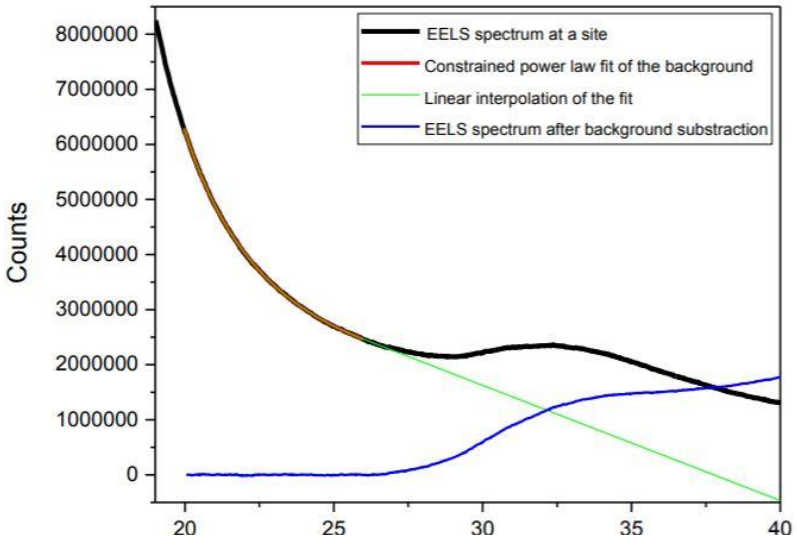

Figure A.6. Background correction of EELS spectrum to obtain the edge onset of the Ge 3d edge.

Sample	Peak position (cm^{-1})	FWHM
Si reference (Si-Si)	520.3	2.83
CVD grown Ge film (Ge-Ge)	299.6	4.02
Ge metalattice spheres in. (Ge-Ge)	299.5	5.96
Ge metalattice sphere out. (Ge-Ge)	298.2	6.18
Ge-Si core shell metalattice. (Ge-Ge)	297.9	7.22

Table A-1. Peak position in Raman spectrum and their corresponding FWHM for different Ge samples.

Site	Average edge onset (eV)	Std. dev
Octahedral (3 data points)	30.10	0.06
Tetrahedral (3 data points)	30.16	0.07
Meta-bond (3 data points)	30.36	0.13

Table A-2. Average and standard deviation for the edge onset of the different sites- Oh, Td and MB.

Site	**Average edge onset (eV)**	**Std. dev**
Core (1) (5 data points)	30.02	0.12
Interface (2) (5 data points)	30.05	0.08
On shell (3) (4 data points)	30.43	0.14
On Shell (4) (5 data points)	30.24	0.13

Table A-3. Average and standard deviation for the edge onset of different points from core to shell.

Particle size from SEM (nm)	% Dispersity	Arg (mmol)	TEOS (mol)	Water(mol)	Ethanol (mol)	Cyclohexane (mol)	Seeds (ml)	Reaction temperature (°C)	Reaction time (Hours)
20.3 ± 1.3	6.4	0.49	0.025	4.8	N/A	N/A	N/A	70	24
22.7 ± 1.2	5.3	0.52	0.025	3.8	N/A	0.042	N/A	60	20
31.1 ± 2.1	6.8		0.032	4	N/A	0.09	20 (23 nm seeds)	60	30
48.8 ± 2.5	5.1		0.032	4	N/A	0.09	20 (23 nm seeds)	60	48
69.7 ± 2.8	4.0	0.5	0.012	1.4	1.4	N/A	0.64(20 nm seeds)	70	24
122.7 ± 5.5	4.5	0.5	0.025	1.2	1.5	N/A	0.27(20 nm)	70	24

Table B-1. Precursor concentrations and reaction conditions for synthesis of silica nanoparticles.

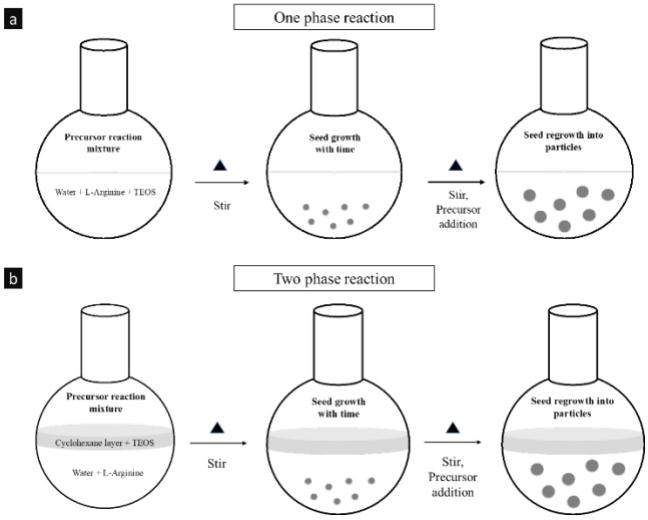

Figure B.1. Schematic representation of for synthesis of silica particles as seeds and their regrowth to get larger particles by (a) one phase reaction (b) two phase reaction

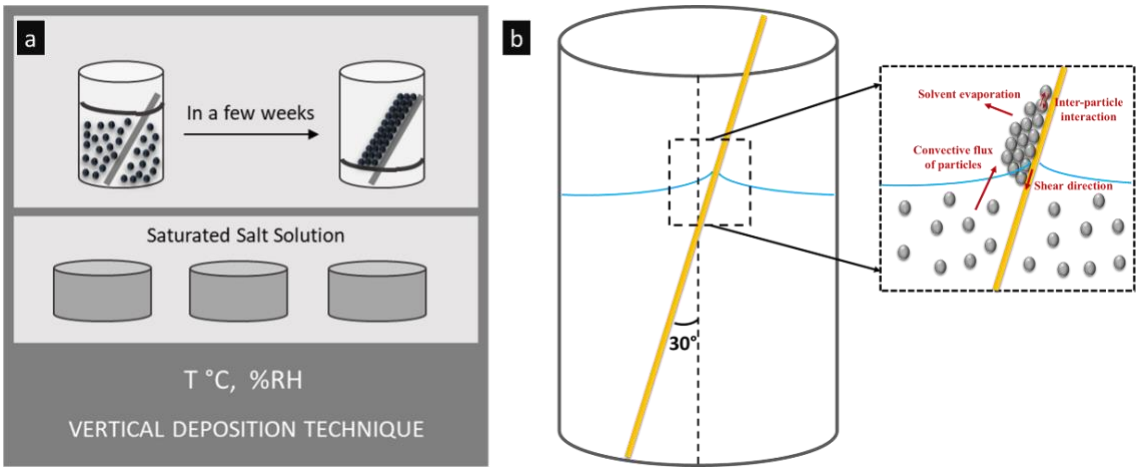

Figure B.2. Schematic representation of (a) the set-up for silica colloidal crystal deposition on Si wafer using vertical deposition technique (b) particles assembling at the interface

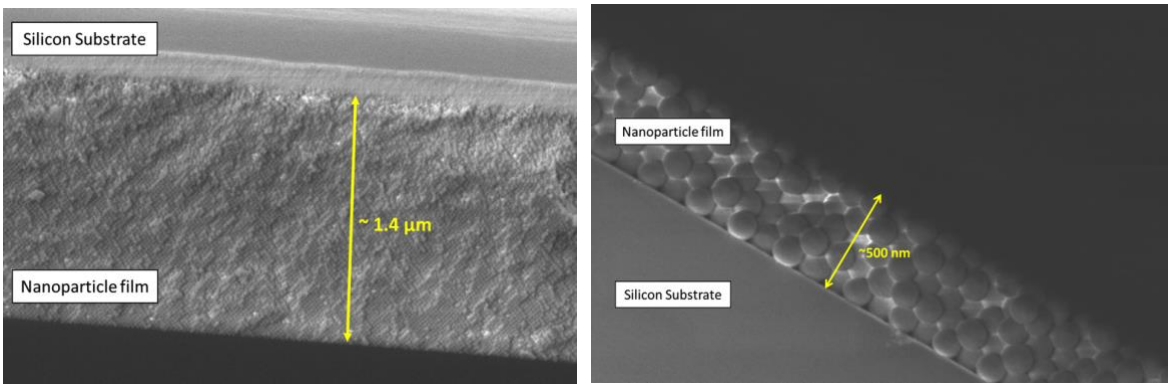

Figure B.3. Cross sectional view of colloidal crystalline films grown from 20.3 and 122.7 nm diameter L-arginine-stabilized silica nanoparticles by vertical evaporative deposition on silicon substrates

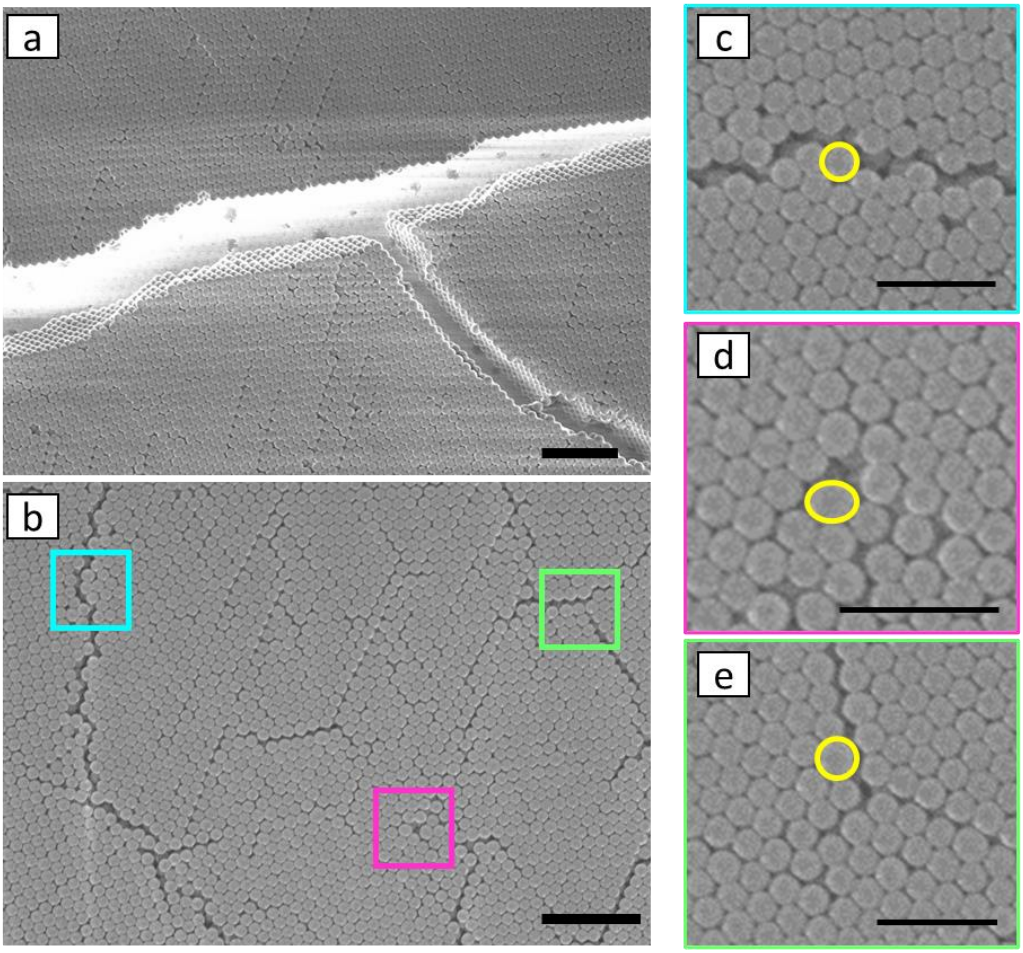

Figure B.4. SEM images of different regions of films grown from 122.7 nm diameter silica nanoparticles. (a) Region showing cracking in the film due to drying; (b) region showing several defects – grain boundaries and vacancies; (c) (d) (e) Magnified regions from (b) showing that the presence of an anomalous particle leads to defects in the colloidal crystal. Scale bars are 1 micron in (a), (b) and 500 nm in (c), (d) and (e).

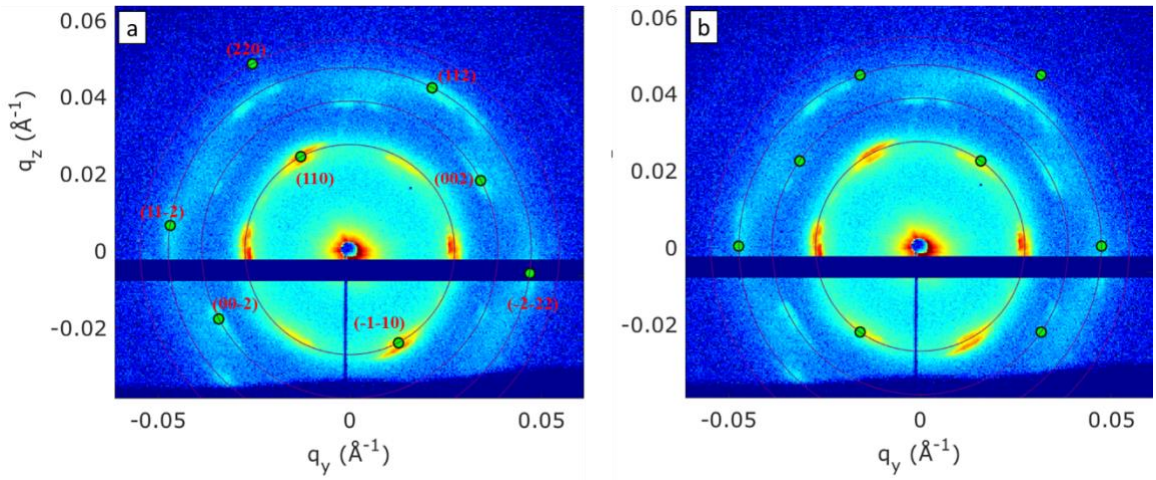

Figure B.5. 22.7 nm 2D pattern indexed with bcc structure with crystallites at different angles in the 2D plane. Crystallites present at different angles (0, 63 and 125 (Figure 3) azimuthal angle) as shown in (a) and (b) in 2D plane explain all the reflections.

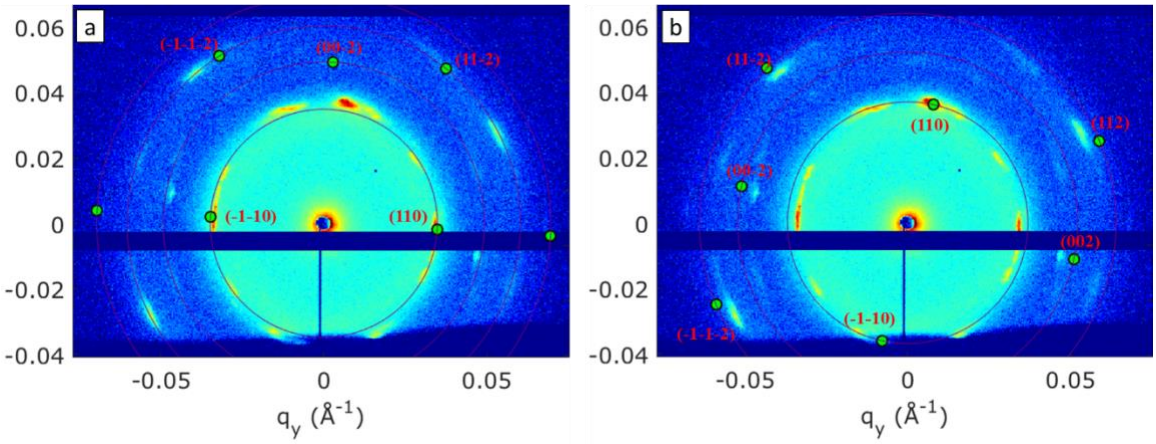

Figure B.6. Another representative 20.3 nm 2D pattern showing bcc structure with two different lattice parameters (a) Indexed with a = 25.5 nm, and (b) Indexed with a= 24.1 nm

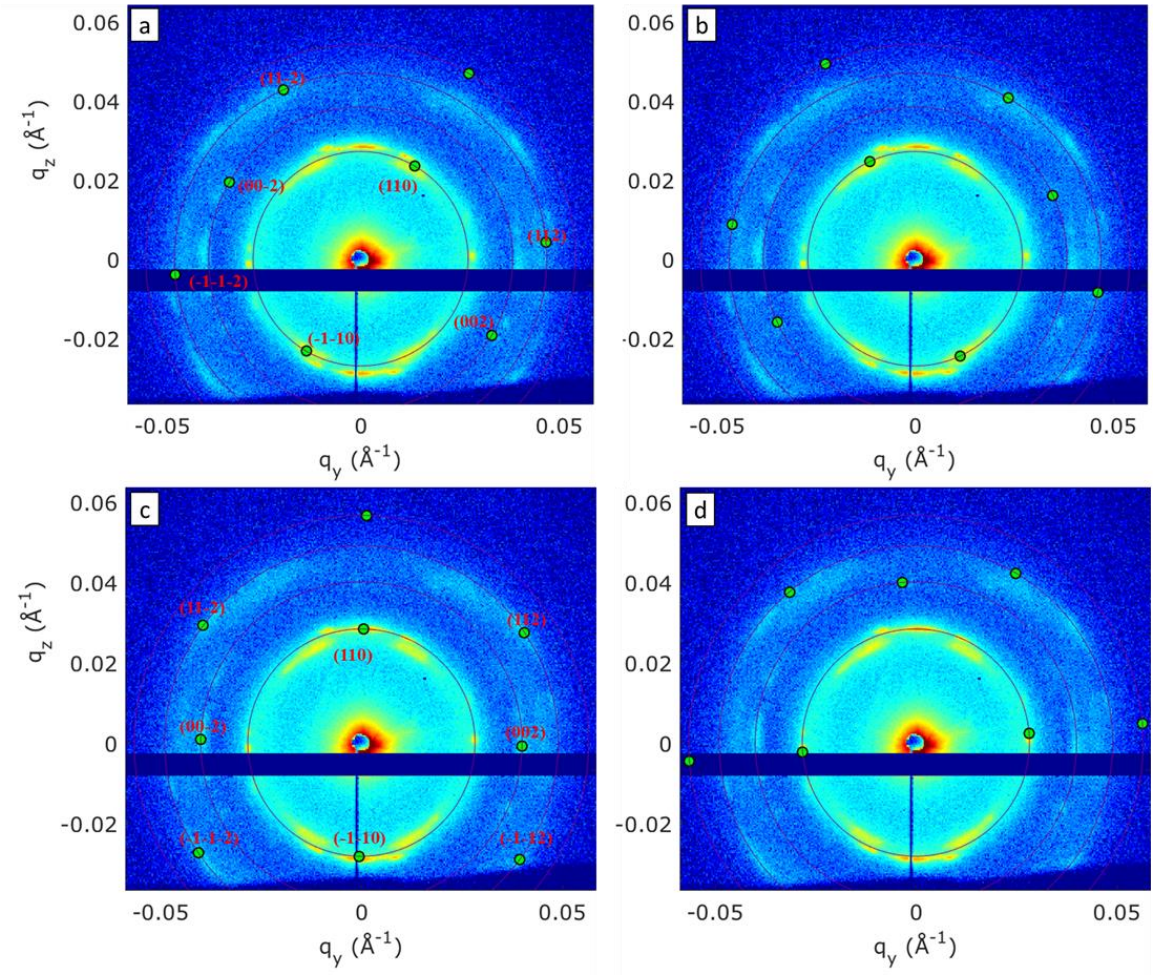

Figure B.7. Another representative 22.7 nm 2D pattern showing bcc structure (a) and (b) a= 32.8 and crystallites at angle 5 and 60, (c) and (d) a =31.4 nm and crystallites at 34 and 130 angle in the 2D plane.

Simulation of scattering from different close pack structures –

(a) Face centered cubic (FCC) – Figure S9 shows real space FCC structure with ABCABC stacking and its corresponding reciprocal lattice. The lattice parameter is 10 and the particle diameter is $10 \cdot \sqrt{2}/2$. X ray beam is along the Z axes (as in the measurement)

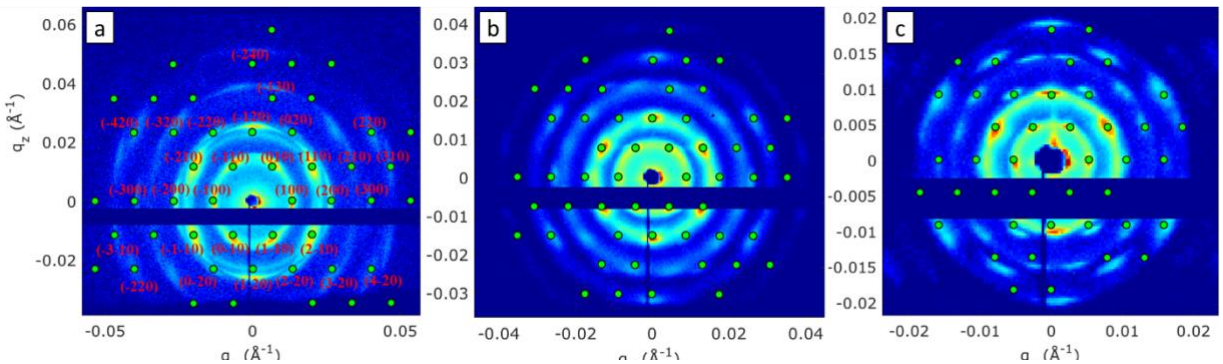

Figure B.8. Second crystallite orientation explaining the remaining reflections in templates indexed in figure 4 (a) 48.8 nm a = 54.4 nm (b) 69.7 nm a = 82.5 nm, and (c) 122.7 nm a = 137.6 nm. The indexing of reflections is same for (a), (b) and (c).

and perpendicular to the close pack plane 111. The reflections on the Bragg condition, or the peaks on qz=0 plane, are denoted with closed symbols. The symbols with thicker lines are the peaks that might cross the qz=0 plane if the peaks are elongated along the qz direction. Such elongated peaks along one direction are called the Bragg rods. For example, if there are stacking faults along the Z axis in Figure S9a, these peaks become the Bragg rods, elongated along the qz axis.

The reciprocal space of FCC structure of which the Z direction orientation is the same with one in Figure S8a is drawn in Figure S8b and S8c with selected major FCC reflections. FCC's first order reflections {111} would not make to the Ewald sphere, which is parallel to qz=0 plane in this case, and will not be observed.

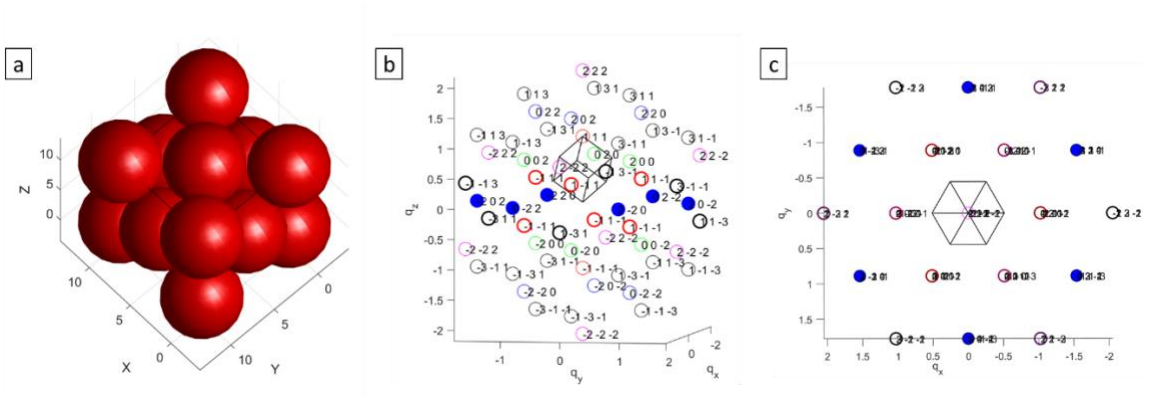

Figure B.9. (a) FCC structure with lattice parameter a=10. (b) and (c) Reciprocal lattice of single crystal FCC with 111 plane parallel to xy plane or 111 reciprocal lattice vector is along the q_z axis.

(b) Hexagonal close packed (HCP) – When spherical particles pack in ABAB packing, the crystal structure is the hexagonally close packed (HCP) structure, which is shown in Figure S9a. The reciprocal lattice of the HCP structure, for which the z-axis direction orientation

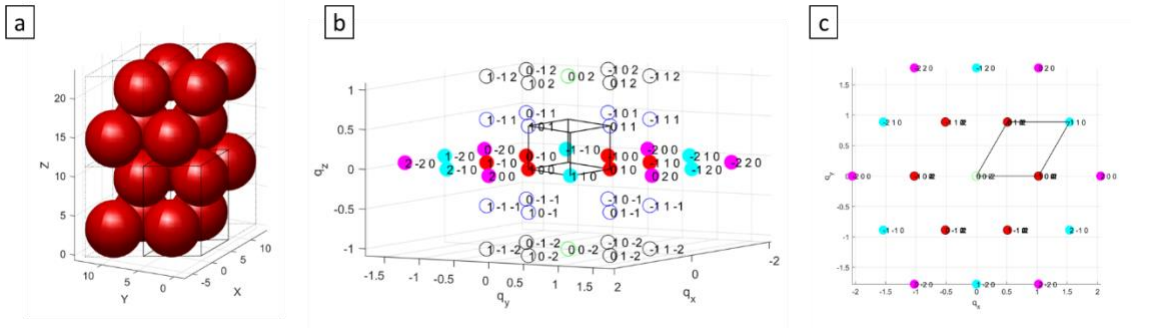

Figure B.10. (a) HCP structure Here, the particle diameter is $10 \cdot \sqrt{2}/2$ and the lattice parameters are $a = 10 \cdot \sqrt{2}/2$ and $c = \sqrt{\frac{8}{3}}a$. (b) and (c) The reciprocal lattice of a single crystal HCP of which 001 plane is parallel to xy plane, or 001 reciprocal lattice vector is along the q_z axis. The reflections in the Bragg condition, or the peaks in the q_z=0 plane, are denoted with closed symbols.

is the same as in Figure S9a, is drawn in Figure S9b and S9c for selected major HCP reflections. Note that if a FCC structure would have a significant stacking fault, the positions of the observed peaks would be similar to those of HCP.

(c) rHCP1 and rHCP2 - When the stacking order of three layers A, B, and C is random, the packing structure is called the rHCP. Each A, B, and C layer is 2D hexagonally packed (HEX). We calculate two rHCPs, where rHCP1 considers that the peak shape is still round and rHCP2 assumes the peak shape elongation along the q_z axis.

For this calculation, we set the x and y fractional coordinates of three layers A, B, and C, as below:

A = [0, 0];

B = [1/3, 2/3];

C = [2/3, 1/3];

The particle jth's real space coordinate $\boldsymbol{r}_j$ can be calculated with a proper choice of hexagonal lattice vectors. The z position of the jth particle is $j \cdot t_L$, where t_L is the layer distance and is identical to the half of the c axis length of the HCP unit cell. The scattering factor for a given hkl is calculated as below

$$A(q_{hkl}) = F(q_{hkl}; D) \sum_{j=1}^{N_L} e^{-jq_{hkl}r_j}$$

And the intensity calculated for all possible hkl's. The shape of each peak is described by a Lorenzian function f.

$$I(q) = \sum_{h,k,l} \left| f\left(q; q_{hkl}, A(q_{hkl}), \sigma_{q_{xy}}, \sigma_{q_z}\right) \right|^2$$

For simplicity, in this calculation, we kept the peak widths $\sigma_{q_{xy}}$ and σ_{q_z} the same for all structures. To include the Bragg rod effect for rHCP2, we decreased the lattice constant

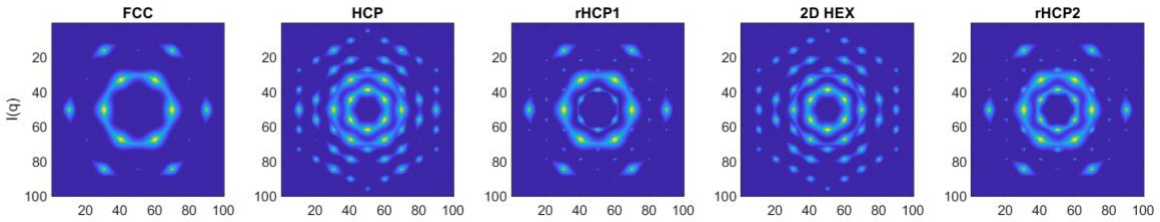

Figure B.11. Comparison of simulated 2D SAXS patterns for different close packed structures.

along the x-ray beam direction that is the z-axis here.

1D pattern structure	**Peak ratio**	**Template size**	**Peak ratio**
2D Hex	12.01	31.1 nm	1.94
HCP	2.98	48.8 nm	2.88
rHCP1	0.46	69.7 nm	1.32
rHCP2	2.66	122.7 nm	1.09

Table B-2. Peak 1: Peak 2 ratio for simulated azimuthally averaged 1D patterns and templates.

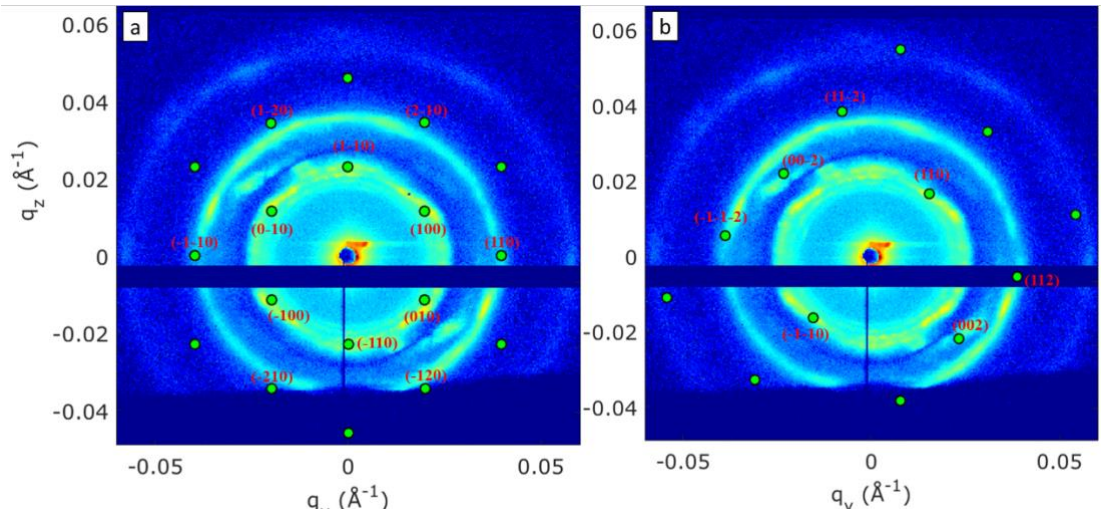

Figure B.12. 31.1 nm template has multiple structures. Indexing of 31.1 nm template with (a) 2D hexagonal, p6mm, a = 31.6 nm. (b) bcc Im3m a= 39.3 nm (r = 33 nm). Multiple structures may be present in the transition size 31.6 nm

Particle size (from SEM, nm)	**Structure**	**Average lattice parameter (From SAXS, nm)**	**Particle size from lattice parameter (nm)** (bcc $2r = \sqrt{3}a/2$, rhcp 2r= a)	**Grain size (nm)**
20.3 ± 1.3	bcc	25 ± 0.8	21.7	555.8 ± 234.3
22.7 ± 1.2	bcc	32.9 ± 1.4	28.5	570.3 ± 237.6
31.1 ± 2.1	rhcp (multiple structures possible)	31.6 ± 0.9	31.6	372.0 ± 64.4

48.8 ± 2.5	rhcp	54.5 ± 0	54.5	881.7 ± 26.4
69.7 ± 2.8	rhcp	82.5 ± 0	82.5	671 ± 15.6
122.7 ± 5.5	rhcp	138.8 ± 1.9	138.8	1704.1

Table B-3. Structures, lattice parameters and average grain sizes of colloidal crystal films grown from different size silica nanoparticles.

Grain size calculation

Linecuts were performed to measure first order diffraction peaks corresponding to a given crystal structure in a sample. The peak so obtained were fit to a Gaussian function by using Origin. The extracted FWHM was corrected for instrumental resolution-based broadening using the equation below,

$$\Delta q_{corr} = \sqrt{(\Delta q_{obs}^2 - \Delta q_{inst}^2)}$$

where Δq_{corr} is the corrected FWHM, Δq_{obs} is the observed FWHM extracted from the first order diffraction peak and Δq_{inst} is the instrumental broadening which is 0.0005 Å^{-1} for our measurement. The resolution-corrected broadening was used to determine the crystallite size using the Debye Scherrer equation. For NPs having multiple crystal structures/mixed phases, the first order diffraction peak from non-overlapping diffraction spots were used to determine crystallite size.

Nanoparticle size (nm)	**Structure**	**Δq_{corr} (Å^{-1})**	**Grain size (nm)**	**Average grain size (nm)**
20.3	bcc	0.00098	576.8	555.8 ± 234.3
		0.00091	619.8	

		0.00059	965.2	
		0.00178	317.3	
		0.00162	347.8	
		0.00111	507.9	
22.7	bcc	0.00064	886.9	570.3 ± 237.6
		0.00177	319.2	
		0.00141	399.7	
		0.0012	471	
		0.00061	924.1	
		0.00115	493.3	
		0.00113	498.1	
31.1	rhcp (multiple structures possible)	0.00116	488.7	372 ± 64.4
		0.00194	291.9	
		0.00141	399.7	
		0.00152	371.9	
		0.00183	308.4	
		0.00152	371.9	
		0.00152	371.9	
48.8	rhcp	0.00066	853.1	715.0 ± 159.5
		0.00066	853.1	
		0.00098	576.9	
		0.00098	576.9	
69.7	rhcp	0.00087	652.6	625.8 ± 73.0
		0.00083	679.9	

		0.00109	518.1	
		0.00087	652.6	
122.7	rhcp	0.00033	1704.1	1366.7 ± 402.6
		0.00033	1704.1	
		0.00062	905.4	
		0.00049	1153.7	

Table B-4 shows the Δq_{obs} and Δq_{corr} for different nanoparticle templates. Three or more first order diffraction peaks were averaged to obtain grain size for a crystal structure.

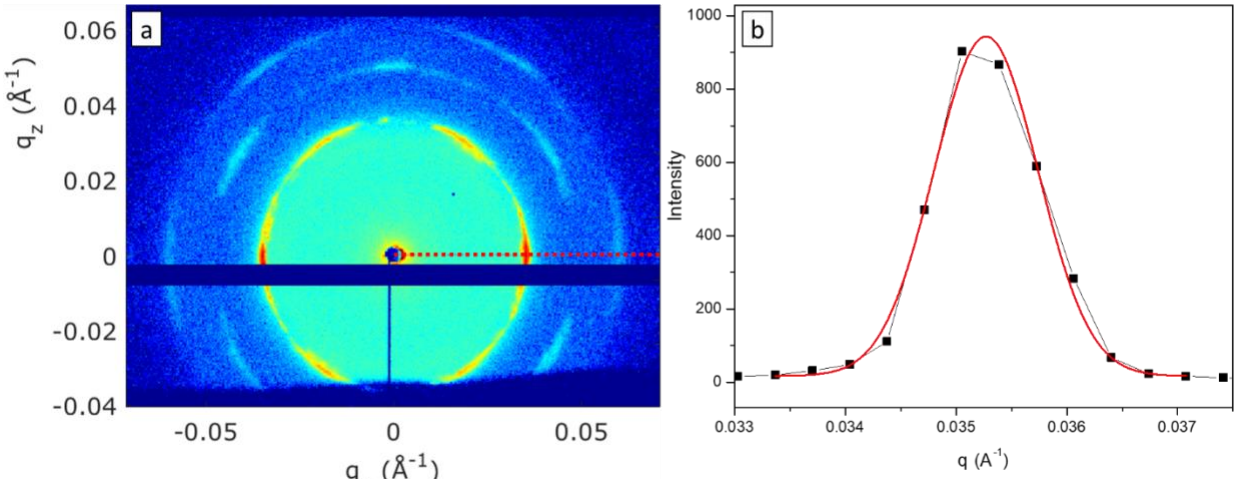

Figure B.13. (a) Linecut along the dotted line for 20.3 nm template with bcc structure (b) Guassian fit for the peak in the linecut to obtain FWHM.

Inverse Ge sample size	**Peak ratio**
31.1 nm	2.0
49.7 nm	2.21
68.8 nm	0.79
122.7 nm	3.0

Table B-5. Inverse Ge structure peak 1: peak 2 ratio.

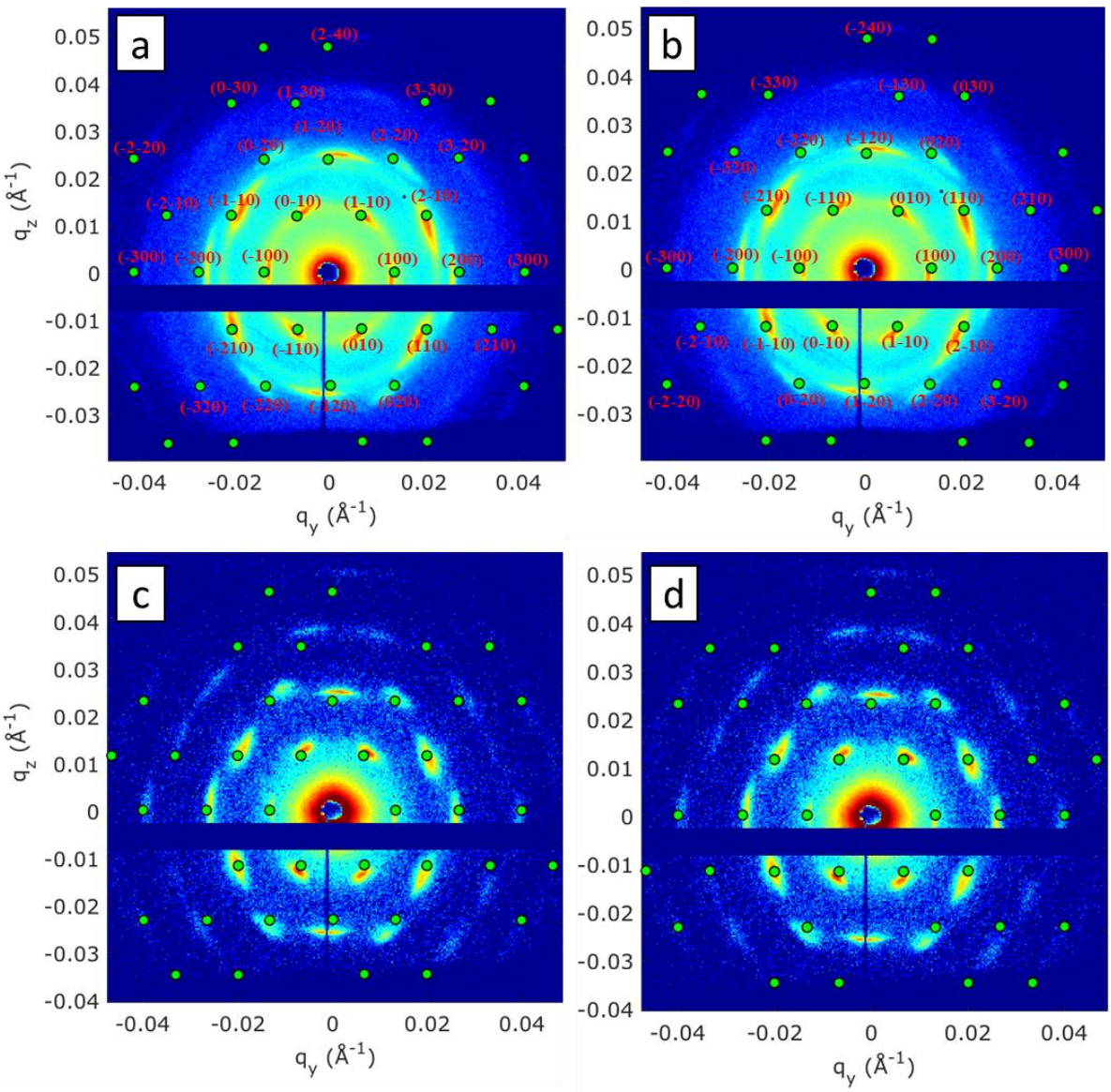

Figure B.14. 2D scattering pattern of (a) and (b) Ge infiltrated 48.8 nm template indexed with p6mm structure and a= 52.7 nm. Two different orientations of crystallites in the 2D plane index all the reflections. (c) and (d) inverse Ge structure from 49 nm template indexed with p6mm and a= 54.5 nm. Two different orientations of crystallites in the 2D plane index all the reflections. Indexing is same for (a) and (c);(b) and (d).

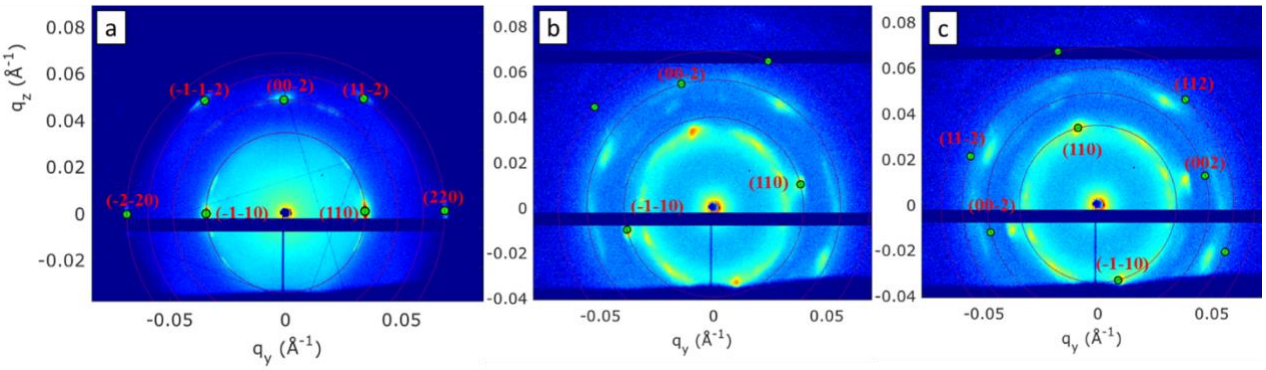

Figure B.15. Inverse structure of (a) 20.3 nm, bcc with a= 25.9 (b) 22.7 nm, bcc structure a= 23.3 nm and (c) 22.7 nm, bcc a= 25.8 nm

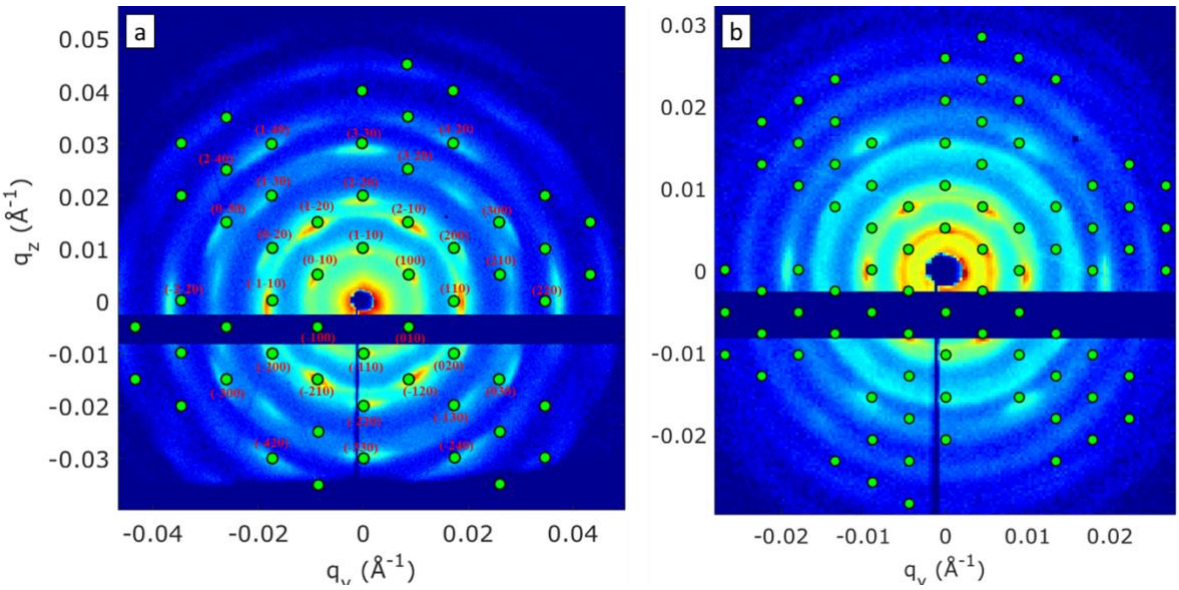

Figure B.16. Inverse structures indexed using 2D hexagonal p6mm (a) 69.7 nm, a = 69.5 nm and (b) 122.7 nm, a = 140.2 nm Indexing is same for (a) and (b).

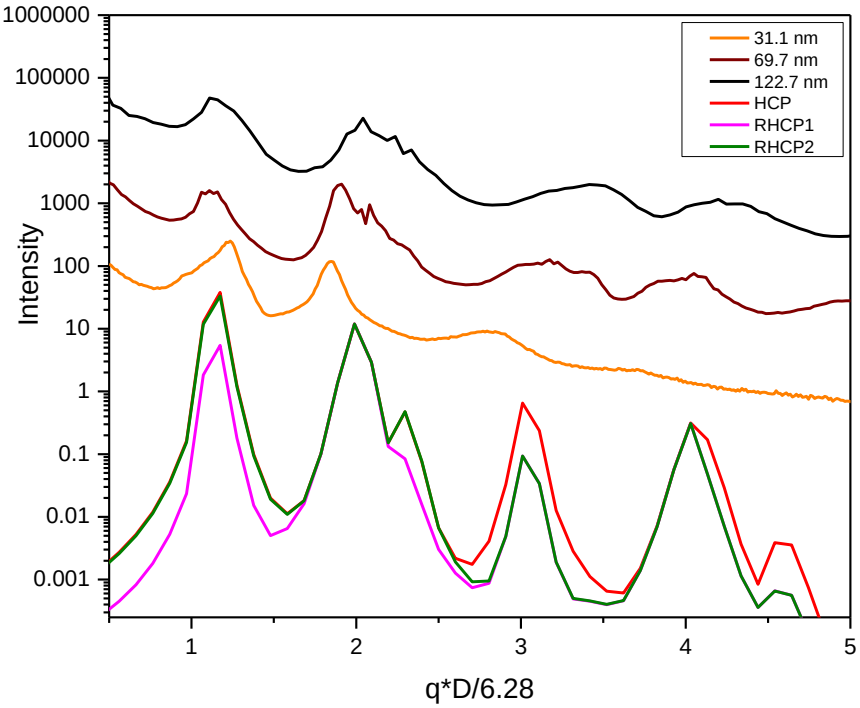

Figure B.17. Comparison of 31.1 nm, 69.7 nm and 122.7 nm inverse structures with simulated 1D patterns. Their peak 1: peak 2 ratio are mentioned in Table S5. With the ratios, there structure is rhcp.

Representative template particle size (from SEM, nm)	**Structure**	**Average lattice parameter (From SAXS, nm)**	**Grain size (nm)**
20.3 ± 1.3	bcc	25.8 ± 0.6	735.8 ± 195.3
22.7 ± 1.2	bcc	26.1± 1.7	322.4 ± 70.3
31.1 ± 2.1	rhcp (multiple structures possible)	33.8 ± 0.3	440.9 ±29.4
48.8 ± 2.5	rhcp	54.4 ± 0.1	673.6 ± 192.4
69.7 ± 2.8	rhcp	70.5 ± 0.9	1045.7± 216.4
122.7 ± 5.5	rhcp	136.1 ± 4.1	885.4 ± 87.8

Table B-6. Structures, lattice parameters and average grain sizes of inverse Ge structures obtained by infiltration of silica templates

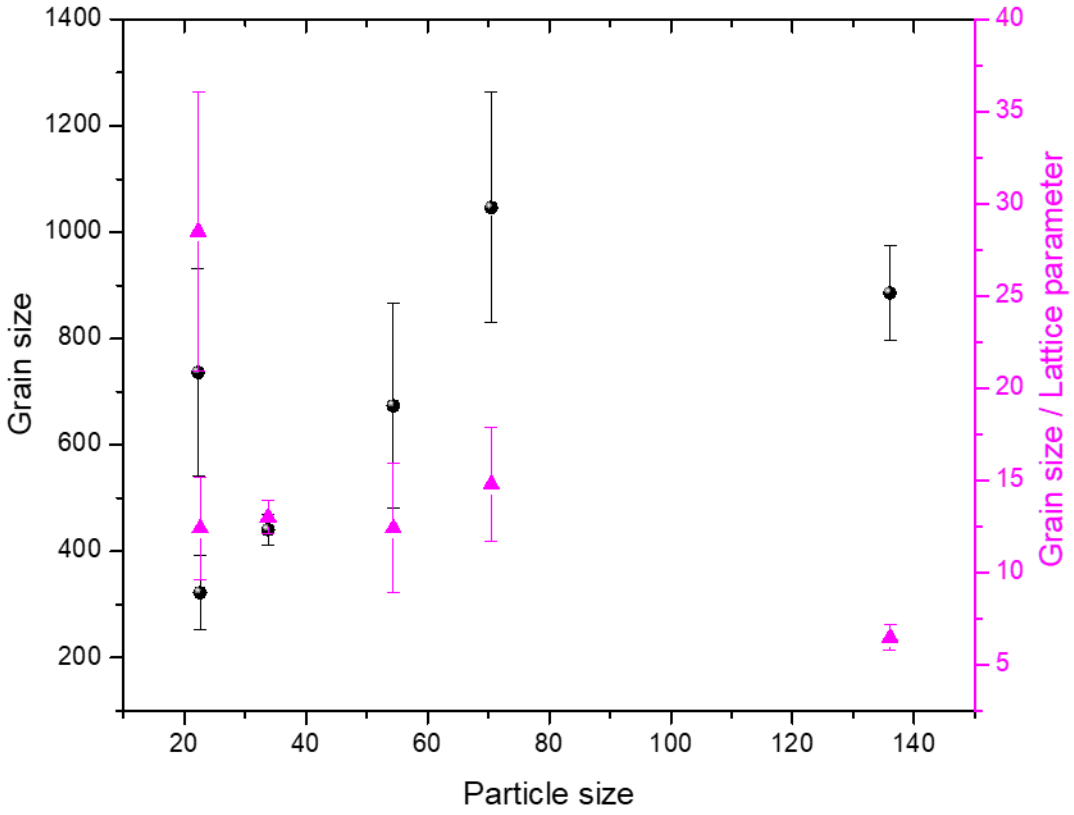

Figure B.18. Variation in grain size and number of unit cells per average grain as a function of particle size. The general trend for the number of unit cells per average grain is similar to the templates.